Nanophotonic engineering of thermal emitters

Thesis by

Komron Joseph Shayegan

In Partial Fulfillment of the Requirements for

the degree of

Doctor of Philosophy

California Institute of Technology

Pasadena, California

2025

(Defended January 31, 2025)

Dedicated to Mama and Baba

Acknowledgements

It is impossible to adequately express the gratitude and debt I owe to all those who have helped shape my path through scientific research. First and foremost, I would like to thank my advisor, Prof. Harry A. Atwater, for his boundless enthusiasm and patience. His guidance and feedback throughout my doctoral research have helped me through challenges both in and out of the lab.

I thank my committee, Professors Alireza Marandi, Andrei Faraon, and Axel Scherer, for their support and feedback. Professor Marandi is the reason I was able to come to Caltech at the outset, and I am indebted to him. He has cultivated a wonderful lab of his own that I have been able to tangentially benefit from through scientific discussions with his group members that go into the wee hours. Prof. Andrei Faraon has acted as a template and scientific resource through his group's own work on inverse-designed and mid-infrared optics. Prof. Axel Scherer's group has also served as a collaborative outlet in mid-infrared filter work and his work has served as a resource for my own research.

Throughout my doctoral research, I have had the privilege of working with great mentors both within and outside of Caltech. Within Caltech, I would like to thank Professor Rossman for his generosity in both time and resources at the outset of my infrared measurements and Professors Schwab and Nadj-Perge for orienting me through Caltech's academic system as a student and teaching assistant. Outside of the Caltech community, I have been honored to work with Professors Shanhui Fan, Aaswath Raman, and Bo Zhao. Bo Zhao really got me started on all modeling and theoretical work in my PhD. Working with and discussing nonreciprocal radiative effects with Professor Raman's student, Jae Hwang, has always been thought-provoking.

The KNI staff, namely Guy DeRose, Bert Mendoza, and Alireza Ghaffari, who have all made enabling our research progress their priority have been a tremendous help throughout the years. The work presented in this thesis was enabled by multiple members in Professor Atwater's group, both formally and informally. To name a few: Yonghwi Kim, Souvik Biswas, Yae-Chan Lim, Ruzan Sokhoyan, Jared Sisler, Magel Su, and Lior Michaeli have all contributed to the fabrication, measurement, modeling, and ideas in this work.

The administrative assistants both in and outside of the Atwater group have made Caltech a welcoming and smooth place to work. The ones who directly improved my experience in the labs are Kamaljit Flower, Thomasine Murphy, Christine Jenstad, and Jennifer Blankenship.

Finally, I would like to acknowledge the people who helped get me to this point outside beyond my time strictly at Caltech. Professor Barry Rand at Princeton was an influential figure in opening his lab's doors to me as an undergraduate researcher and has continued to provide feedback.

My friends throughout the years who have made Pasadena a wonderful place to live: Sophia, Aidan, Robby, Ryoto, Nico, Jared, Melissa, Big Dave, Parker, Souvik, Ramon, Claudio, Morgan, Meir and the little ones, and many, many more.

There have been good times and there have been bad times; and through it all there has always been family. I am extremely grateful to call myself a part of this family, Mama, Baba, Leila, and Rameen.

Abstract

Thermal emission is our most ubiquitous light source, as all objects with non-zero temperature emit this type of radiation. Consequently, our ability to shape the spectral and directional properties of thermally emitted and absorbed light by structures is both intriguing at a fundamental level and has practical implications for infrared light sources, radiative cooling, and energy harvesting systems. To impart desired properties to emitted radiation, nanophotonic designs where subwavelength features are patterned into structures have proved effective in preliminary demonstrations of engineered nanoscale control of thermal emission.

In this thesis, we leverage nanophotonic designs to demonstrate new phenomena in the context of thermal emission. We first use a guided-mode structure made of α-Si to resonantly couple to magneto-optically active InAs. The magneto-optic response is a common effect used in nonreciprocal optical elements, which we use here to directly observe a violation of the Kirchhoff thermal radiation law, a strict equality in the spectral, directional absorptivity and emissivity. This demonstration is significant in two ways: first, it opens new avenues to design thermal emitters with distinct spectral, directional emissivity and absorptivity properties, and second, it confirms theoretical predictions which have long lacked experimental confirmation.

We then extend this experimental Kirchhoff violation to a broadband, directive thermal emitter. The nanophotonic design to achieve this is a deeply subwavelength structure of gradient epsilon-near-zero InAs layers that couple to a Berreman mode. The angular selectivity is determined by the stack thickness, while the broadband spectral range of the effect is imparted by the closely spectrally separated epsilon-near-zero wavelengths.

Finally, we theoretically and experimentally lay the groundwork for a thermal lens, where emitted radiation is directed to a focus a given distance above the surface of the structure. Using a combination of coupled dipole approximation, global optimization, and experimental measurements, we realize the necessary collective and local resonance conditions for this effect.

Published Content and Contribution

* indicates equal contribution

[1] **K. J. Shayegan**, B. Zhao, Y. Kim, S. Fan, H. A. Atwater, Nonreciprocal infrared absorption via resonant magneto-optical coupling to InAs. *Sci. Adv.* **8**, eabm4308 (2022). DOI: 10.1126/sciadv.abm4308.

K. J. S. *performed measurements, supported the theoretical and modeling work, and wrote the manuscript.*

[2] **K. J. Shayegan**, S. Biswas, B. Zhao, H. A. Atwater, Direct observation of the violation of Kirchhoff's law of thermal radiation. *Nature Photonics* **17**, 891-896 (2023). https://doi.org/10.1038/s41566-023-01261-6.

K. J. S. *fabricated the samples, carried out the measurements, led the data analysis and modelling, and wrote the manuscript.*

[3] R. Sokhoyan, P. Thureja, J. Sisler, M. Grajower, **K. J. Shayegan**, E. Feigenbaum, S. Elhadj, H. A. Atwater, Electrically tunable conducting oxide metasurfaces for high power applications. *Nanophotonics* **12**, 293-253 (2023). https://doi.org/10.1515/nanoph-2022-0594.

K. J. S. *performed auxiliary temperature-dependent infrared optical characterization of the device layers.*

[4] T. Jeon, J. Myung, C. Choi, **K. J. Shayegan**, S. M. Lewis, A. Scherer, Novel deposition method of cross-linked polyethylene thin film for low-refractive-index mid-infrared optical coatings. *Sensors* **23**, 9810 (2023). https://doi.org/10.3390/s23249810.

K. J. S. *performed auxiliary infrared optical measurements.*

[5] **K. J. Shayegan***, J. S. Hwang*, B. Zhao, A. P. Raman, H. A. Atwater, Broadband nonreciprocal thermal emissivity and absorptivity. *Light Sci. & Appl.* **13**, 176-181 (2024). https://doi.org/10.1038/s41377-024-01520-3.

K. J. S. *performed measurements and simulations of the magneto-optic response of the structures and conceived of the project idea.*

In preparation

[6] Y.-C. Lim, **K. J. Shayegan**, H. A. Atwater, Leaky modes for dual polarization, directive, broadband thermal emission. *in preparation* (2025).

K. J. S. *performed project supervision and conception.*

[7] **K. J. Shayegan**, L. Michaeli, G. R. Rossman, H. A. Atwater, Focused thermal emission through collective resonances. *in preparation* (2025).

K. J. S. *performed device fabrication, theoretical modelling, optimization, design, measurement, and wrote the manuscript.*

Table of Contents

List of Figures

List of Tables

Chapter 1

Introduction

"I wish I could show you when you are lonely or in darkness the astonishing light of your own being."

- Hafez

1.1 Evolving conceptions of thermal radiation

All objects with finite temperature emit thermal radiation. Because of its universal nature, everyone has some intuitive understanding of thermally emitted radiation. People know that when a blacksmith heats a piece of iron, the glowing end that is pulled from the fire is extremely hot and malleable. We have harnessed this incandescence for millennia, from selective transmission and reflection of the Lycurgus cup to Edison's light bulb [1].

This ubiquity of thermally emitted radiation and the role it plays in our everyday existence continues to drive our interest in understanding the basic properties of how we can generate, manipulate, and harness this type of light. Recent advances in nanolithography and laser light sources have given birth to the field of metasurfaces, integrated photonics, and spurred developments in quantum optics. However, the application of these new fabrication technologies with the aim of controlling thermally emitted radiation, where the wavelength and phase front of the light are not constrained is far less explored. This thesis aims to apply nanophotonic principles to thermally emitted radiation, demonstrating phenomena such as nonreciprocity of thermal emission and extended spatial control to show complex functions such as focusing.

1.2 Classical and quantum properties of thermally emitted radiation

The spectral and spatial distributions of thermal radiation from unpatterned, gray bodies is described by Planck's law of blackbody radiation and Lambert's cosine law [2]. The angular, or spatial, distribution of the radiance of thermally emitted radiation from a surface with no micro- or nano-structuring follows Lambert's cosine law:

$$I_\theta = I_0 \cos(\theta)\, d\Omega \qquad \text{(Eq. 1.1)}$$

where θ gives the angle relative to normal, $d\Omega$ defines the subtended solid angle through which the photon flux is observed per unit area at angle θ relative to normal, and I_0 gives the radiance at normal incidence.

The accurate description of the spectral distribution, or radiance, of thermally emitted radiation, I_v, (W m^{-2} sr^{-1} Hz^{-1}) was formalized by Max Planck in 1901 by accounting for the quantization of cavity radiation [2]. Planck's formulation of the quantum aspect of emitted radiation solved a long-standing issue from the classical Rayleigh-Jeans formula, known as the "ultraviolet catastrophe". The Rayleigh-Jeans formula for the spectral radiance predicted that the spectral distribution followed a frequency-squared distribution, making the high-frequency spectral distribution of a blackbody divergent.

*Considering a rectangular cavity with sides of length A, B, C in the $x, y,$ and z dimensions, the standing waves for the fundamental wave function [3]

$$e^{i(\boldsymbol{k}\cdot\boldsymbol{r}-\omega t)} = e^{k_x x} e^{k_y y} e^{k_z z} e^{-i\omega t} \quad \text{(Eq. 1.2)}$$

will exist when

$$k_x A = \pi n_x \; ; \; k_y B = \pi n_y \; ; \; k_z C = \pi n_z \quad \text{(Eq. 1.3)}$$

with n_x, n_y, n_z all being integers. The modes as a function of frequency, v, will then take the form

$$\boldsymbol{k}^2 = \frac{\omega^2}{c^2} = \pi^2 \left(\frac{{n_x}^2}{A^2} + \frac{{n_y}^2}{B^2} + \frac{{n_z}^2}{C^2} \right) \quad \text{(Eq. 1.4)}$$

or

$$\frac{4v^2}{c^2} = \left(\frac{{n_x}^2}{A^2} + \frac{{n_y}^2}{B^2} + \frac{{n_z}^2}{C^2} \right) \quad \text{(Eq. 1.5)}$$

which gives the allowed modes for a given frequency for an ellipsoid. The speed of light is denoted by c. For a rectangular cavity (one octant of the ellipsoid), the number of occupied modes up to frequency v will be

$$\frac{1}{8}\frac{4\pi}{3}\frac{2vA}{c}\frac{2vB}{c}\frac{2vC}{c} = \frac{4\pi v^3}{3c^3}V \quad \text{(Eq. 1.6)}$$

therefore, the density of modes will be

$$g = \frac{8\pi v^3}{3c^3} \quad \text{(Eq. 1.7)}$$

* This derivation of Planck's law follows Chapter 7 of G. R. Fowles, *Introduction to Modern Optics* (Dover, 1989).

where the factor of two comes from the orthogonality of the two polarization modes. The density of modes per unit volume, per unit frequency is then

$$g_v = \frac{8\pi v^2}{c^3} \quad \text{(Eq. 1.8)}$$

At this point, if one were to calculate the spectral radiance, i.e. the power per unit area per unit frequency, the emitted radiation would be divergent at high frequencies. This is where Planck's photon statistics come into play.

If the number of photons that can occupy a given mode of a given frequency is quantized, then the spectral density of cavity radiation, u_v, is given by

$$u_v = g_v h v \langle n_v \rangle = \frac{8\pi h v^3}{c^3} \langle n_v \rangle \quad \text{(Eq. 1.9)}$$

where $\langle n_v \rangle$ is the average number of photons per mode. The frequency-dependent occupation factor is the Bose-Einstein distribution for photons (see reference 3). This gives us a spectral density of the cavity radiation

$$u_v = \frac{8\pi h v^3}{c^3} \frac{1}{e^{hv/kT} - 1} \quad \text{(Eq. 1.10)}$$

Planck's law gives the spectral radiance of the blackbody cavity, i.e. the frequency-dependent intensity distribution,

$$I_v = \frac{1}{4} c\, u_v = \frac{2\pi h v^3}{c^2} \frac{1}{e^{hv/kT} - 1} \quad \text{(Eq. 1.11)}$$

We note that Planck's law, through photon statistics, ensures that the spectral radiance for large frequencies, v, will no longer be divergent (Figure 1.1 a).

To summarize, the directional and spectral properties of thermal radiation are given by Lambert's cosine and Planck's law respectively. Both these descriptions of the emitted radiation imply a diffuse (i.e. not directionally selective) and broadband nature.

1.3 Nanophotonic engineering of thermal radiation

Recent developments in nanofabrication have allowed us to impart dielectric features that interact with light on the subwavelength scale. Periodic boundary conditions on the order of the wavelength of light have enabled photonic crystals that engineer the photonic density of states (PDoS) [4], while subwavelength scatterers designed with a spatial phase profile have enabled flat

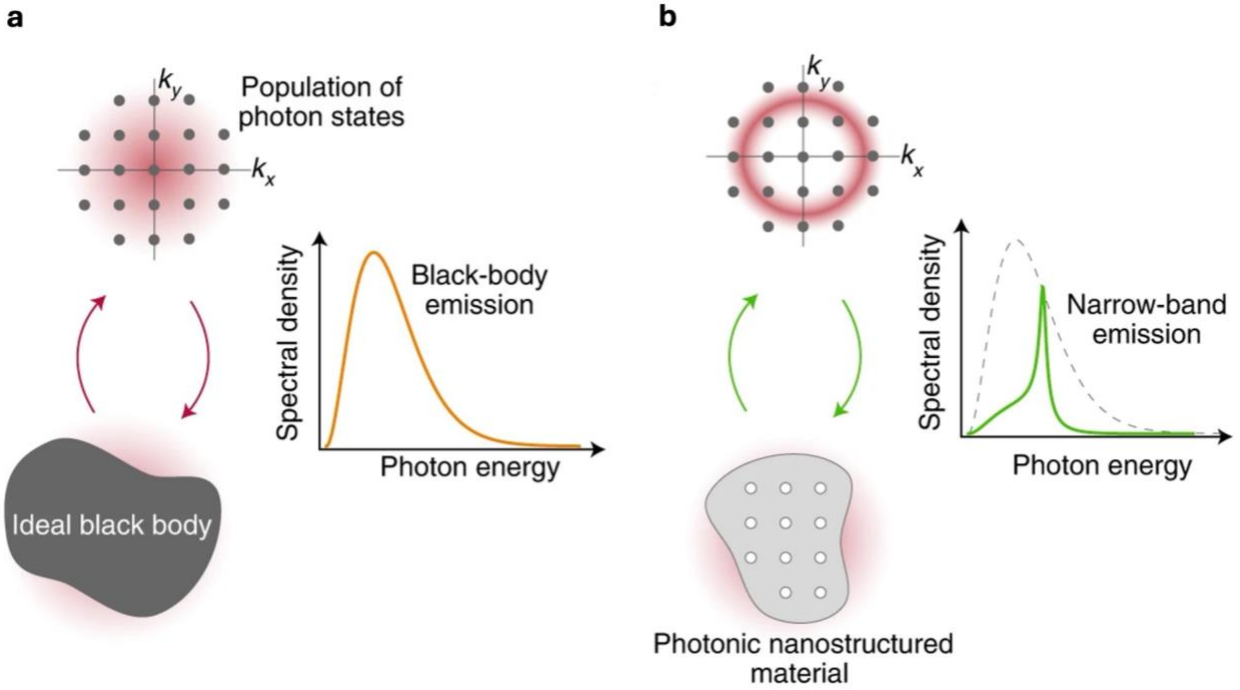

Figure 1.1 Blackbody radiation from unpatterned and patterned emitters. (**a**) A plot of the spectral density, u_v, as a function of photon energy. An ideal blackbody will have a broadband spectral distribution of the emitted radiation following Planck's law. (**b**) Engineering a photonic structure at the wavelength scale can shape the PDoS, and thus the modes that the radiation can efficiently couple to. This can be done to produce narrowband emission. This figure has been modified from reference 11.

optics such as metalenses [5]. These designs have mainly been limited to coherent illumination with laser light, where the spectral and/or spatial phase profile of the input electromagnetic field is controlled.

These advances in nanofabrication and control of scattering properties are transferrable to thermally emitted light, however the mapping is not one-to-one. Thermally emitted radiation is the product of random charge fluctuations in material, which can have long-range spatial coherence if coupled to surface waves (e.g. surface phonon polaritons, SPhPs), but most often does not.

Consequently, the spectral and spatial coherence must be imposed on the emitted light through PDoS engineering and use of extended or guided modes (see Figure 1.1 b).

The first demonstration and characterization of spectrally and spatially coherent thermal emission was done by ruling a diffraction grating onto the surface of SiC (Figure 1.2 a) [6]. The diffraction grating coupled SPhPs supported by the SiC to the far-field when the wavelength, λ, and angle, θ, satisfy the diffraction condition

$$\frac{2\pi}{\lambda}\sin(\theta) = k_{||} + n\frac{2\pi}{d} \qquad \text{(Eq. 1.12)}$$

where $k_{||}$ defines the in-plane wavevector (i.e. the wavevector of the surface wave), d defines the period of the grating, and n is an integer (i.e. the order of diffraction). The resulting emission pattern for this structure has a narrow spectral and angular distribution, as shown in Figure 1.2 b. The in-plane coherence length, l_c, for a given wavelength can be backed out through the angular spread of the emission at that wavelength:

$$l_c = \frac{\lambda}{\Delta\theta} \qquad \text{(Eq. 1.13)}$$

This method of imposing coherence to light radiated by a thermal emitter intrinsically links the spectral and spatial coherence properties of the radiation. The in-plane spatial coherence provided

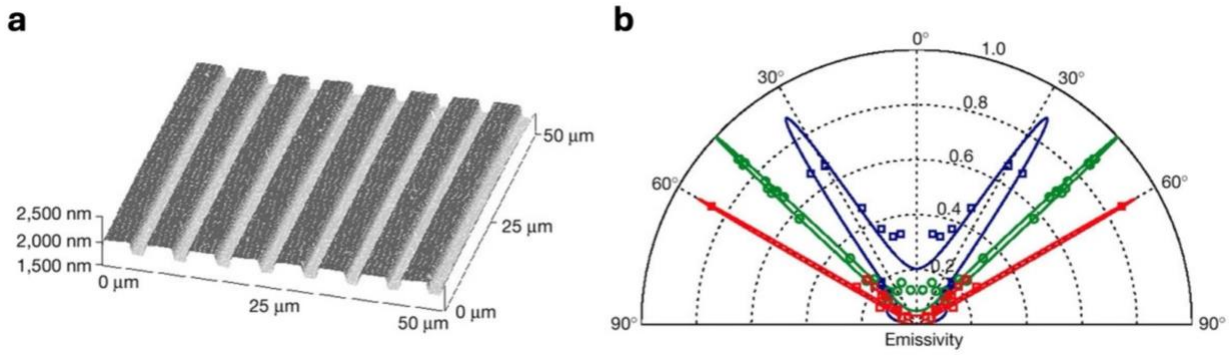

Figure 1.2 Coherence effects on emitted radiation from nano-structured materials. (**a**) Atomic force microscopy image of grating ruled onto SiC. The period of the grating is 6.25 µm. The grating outcouples surface phonon polaritons to the far field when the diffraction condition is satisfied. (**b**) Polar plots of transverse magnetic polarized emission from the structure at three different wavelengths (λ = 11.04 µm, 11.36 µm, and 11.86 µm for the blue, red, and green traces respectively). The narrow angular distribution of the radiated light correlates to high spatial coherence. This figure has been reproduced and modified from reference 6.

by the SPhP, however, can be substituted through other photonic phenomena, like guided modes (Chapters 2 and 3), Berreman modes (Chapter 4), and surface lattice resonances (Chapter 5).

1.4 Applications of engineered thermal emitters

Thermal emitters with engineered nanophotonic properties have a multitude of applications. Narrowband, omnidirectional thermal emitters have been demonstrated as efficient, tunable mid-infrared light sources [7] and used for on-chip gas sensing (Figure 1.3) [8]. A further extension of these mid-infrared light sources would be to make compact mid-infrared flat-optics by integrating these light sources with the photonic components used to manipulate the amplitude, phase, and polarization of the emitted light (Figure 1.4) [9, 10, 11].

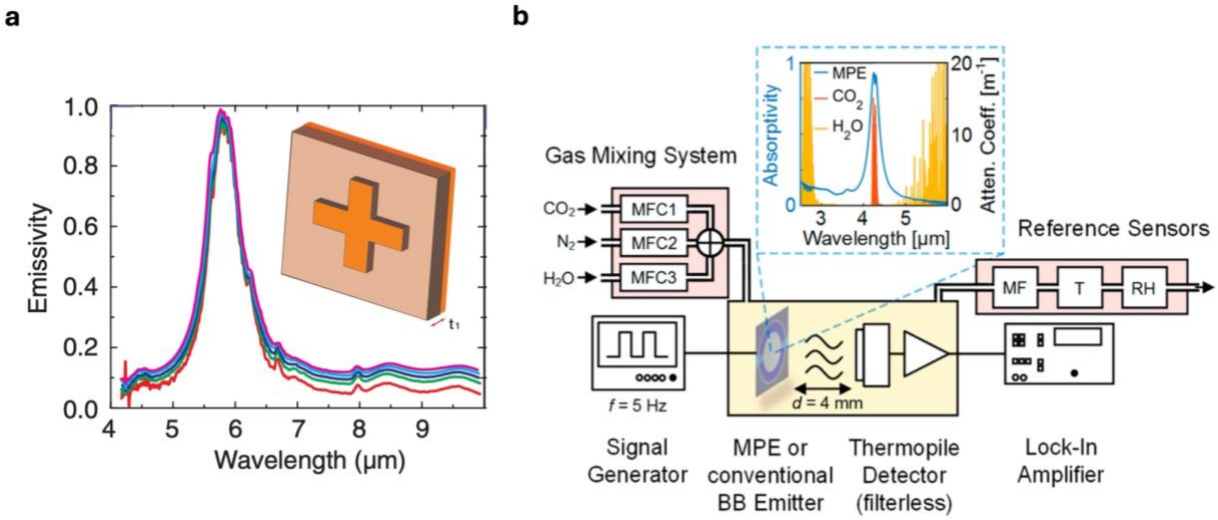

Figure 1.3 Narrowband thermal emitters for spectroscopy and sensing. (**a**) Narrowband thermal emission through a metal-insulator-metal cross shaped array impedance matched to free space. Figure has been adapted from reference 7. (**b**) On-chip narrowband thermal emitter for optical gas sensing. The emission is measured at a thermopile detector. The signal is modulated by the absorbance of a gas analyte that fills the chamber. Figure has been reproduced and modified from reference 8.

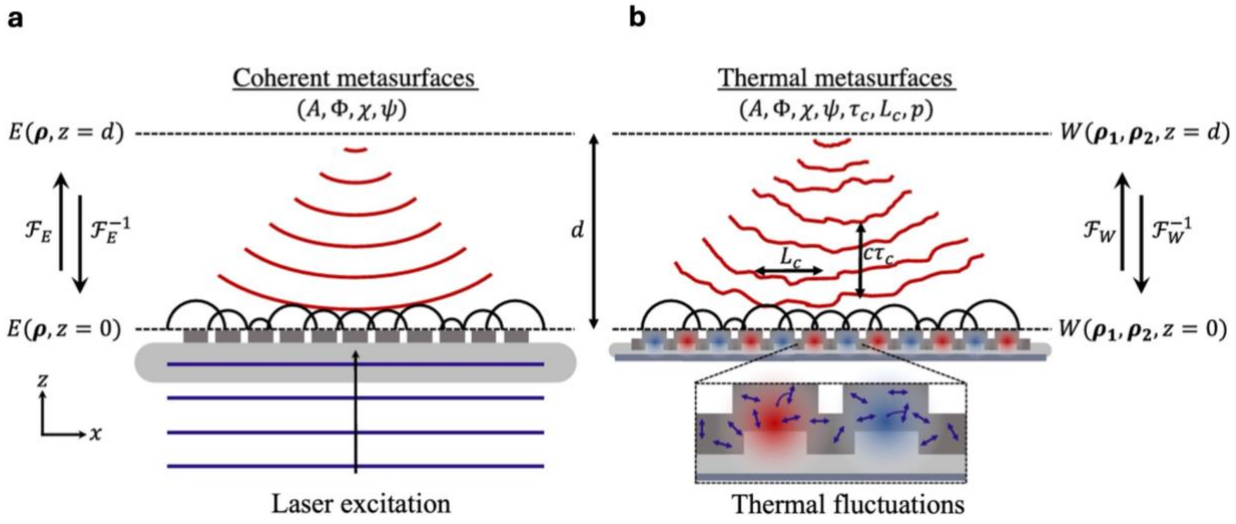

Figure 1.4 Conceptual comparison between a "coherent" metasurface and a thermal metasurface. (**a**) In the coherent case, the metasurface is illuminated with laser excitation. The designed elements impart a phase that is independent of collective (i.e. inter-resonator coupling) responses. (**b**) Thermal metasurface, where thermal fluctuations populate extended modes and are scattered to the far-field. The coherence is imparted through the inter-resonator coupling/extended modes and is correlated to the angular and spectral selectivity. Figure has been reproduced and modified from reference 11.

Nanophotonic thermal emitters have had most substantial applications in energy conversion and management, mainly through thermophotovoltaics and radiative coolers, respectively. Thermophotovoltaics rely on the conversion of radiated heat to electrical energy. Engineering a heterostructure that highly absorbs broadband solar radiation and emits radiation selectively above the energy bandgap of a photovoltaic is a way to minimize the intrinsic inefficiency of having below-bandgap photons incident on a photovoltaic. Conversely, an engineered broadband infrared thermal emitter that highly reflects visible light has been used as a passive radiative cooler [12], demonstrating sub-ambient non-evaporative cooling (Figure 1.5).

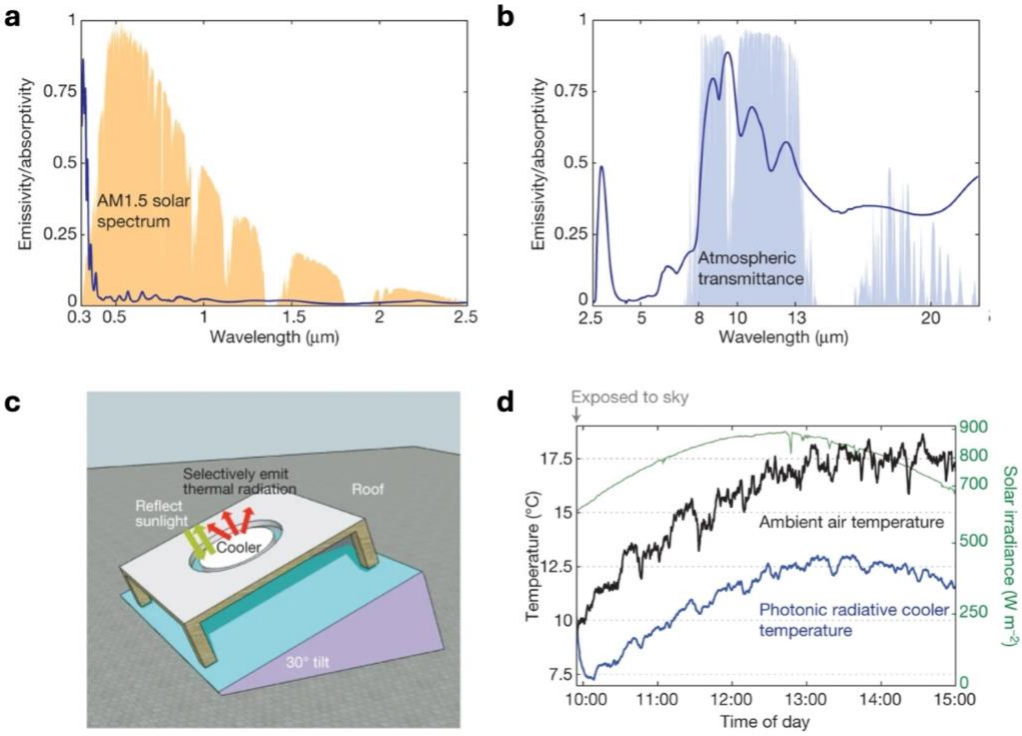

Figure 1.5 Passive radiative cooling through emissivity engineering of nanophotonic structures. (**a**) Emissivity/absorptivity spectra of the designed cooler in the visible spectrum, demonstrating high reflectivity. (**b**) Emissivity/absorptivity spectra for the radiative cooler, with high emissivity coinciding with the atmospheric transparency window. (**c**) The radiative cooling experiment, where visible light from the sun is reflected and thermal radiation is emitted through the earth's transparency window. (**d**) The temperature of the radiative cooler compared to the ambient air temperature during peak sun illumination. This figure is adapted from reference 12.

One of the primary areas of interest to improve radiative heat management (e.g. cooling or energy conversion) enabled by nanophotonic thermal emitters is to design structures that go beyond Kirchhoff's law of thermal radiation. Kirchhoff's law of thermal radiation states that the spectral, angular absorptivity and spectral angular emissivity of a body must be equal. This derivation assumes the thermal emitter obeys Lorentz reciprocity, meaning a nonreciprocal thermal emitter necessarily violates Kirchhoff's law of thermal radiation [13]. We include a derivation of Lorentz reciprocal relations in Chapter 2.

One can think of such an emitter as analogous to an optical isolator, where specific energy photons are absorbed efficiently in one channel and emitted efficiently to another. This concept has been extended to the idea of time-asymmetric photovoltaics [14] where absorption of radiation and subsequent re-emission from the thermal emitter/absorber back to the source is considered an inherent loss mechanism (Figure 1.6 a). In the case of a time-asymmetric, or nonreciprocal, absorber, the absorbed radiation can be re-emitted in a channel distinct from the absorptive

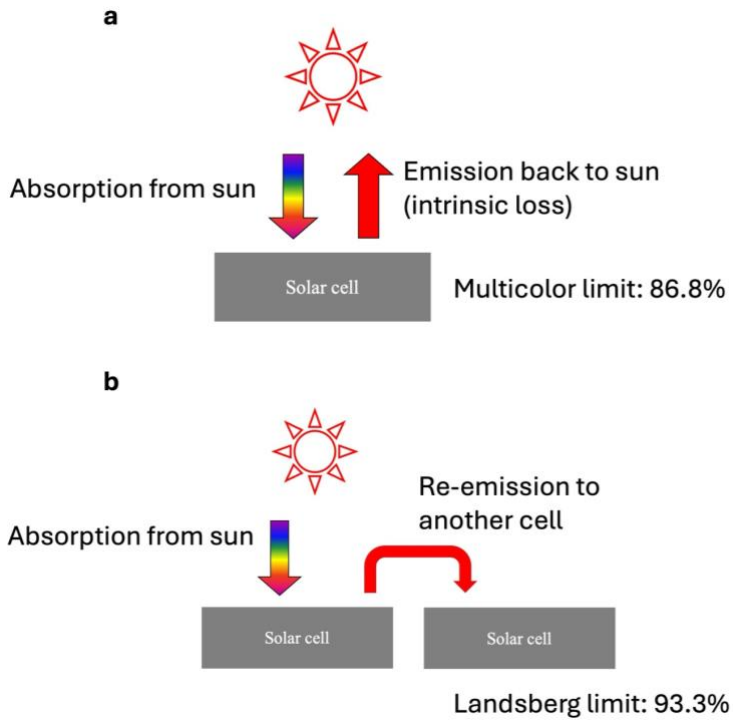

Figure 1.6 Concept of nonreciprocal photovoltaics. (**a**) In the reciprocal case, radiation is absorbed from a source and directly re-emitted from the absorber back to the source with the same efficiency. This can be considered an intrinsic loss mechanism, and limits conversion efficiency to the "multicolor" limit. (**b**) The nonreciprocal case, where the intrinsic loss mechanism of re-emission is directed to a secondary cell. In this circumstance, the theoretical efficiency limit is the Landsberg limit. This figure is adapted from presentations by S. Fan and H. A. Atwater.

channel, circumventing this loss (Figure 1.6 b). Multiple theoretical works have established improved photovoltaic efficiencies that could be attained through a series of these nonreciprocal absorbers.

While detailed balance may be broken, the second law of thermodynamics is maintained. If one were to integrate the absorptivity and emissivity of the emitter over all angles and over all wavelengths, the total hemispherical emission and absorption must be equal. At the writing of this thesis, it is still a matter of debate as to the true practical efficiency with this constraint in place [15].

1.5 Summary of scientific content and scope of thesis

This thesis takes nanophotonic and plasmonic concepts and leverages them to highlight fundamental phenomena of thermal emission, namely Kirchhoff violation and thermal lensing. To this end, we build the understanding of our structures with a variety of theoretical models for diffraction and waveguiding, simulation tools for anti-symmetric permittivity tensors, and analytical calculations to predict interparticle coupling of finite resonant thermally emitting nanoparticles. These models are included alongside the experimental data they are used to predict and explain.

Chapters 2 and 3 of this thesis demonstrate nonreciprocal structures in the far-field through resonant magneto-optical coupling to InAs. Direct thermal emission measurements with applied external magnetic fields, the first of their kind, were made to assess our ability to create thermal emitters with distinct absorptivity and emissivity channels (Chapter 3). The work in Chapter 3 builds upon the initial results in Chapter 2 and introduces the concept of an angle-resolved thermal emission spectroscopy setup for when the spectral, directional emissivity and absorptivity of a structure are unequal.

After both absorptivity and direct emissivity measurements of nonreciprocal structures were demonstrated, we extended the concept of Kirchhoff-violating structures to a tunable, broadband spectral range using Berreman modes, in collaboration with Jae-Seung Hwang and Aaswath Raman at UCLA (Chapter 4). A tunable, broadband nonreciprocal absorptivity/emissivity window is particularly important in assessing the true efficiency gains that can be realized through nonreciprocal thermal absorbers.

In Chapter 5 of this thesis, we extend the concept of spatially coherent thermal emission realized through collective resonances to create a device with an in-plane phase profile. The phase profile is designed to demonstrate self-focused thermal emission, where specific wavelengths of the thermally generated radiation are focused to a spot. This requires an extended, or collective mode, that is supported by a finite array of individually spectrally varying resonators. The extended mode allows for sufficient in-plane coherence build-up, while the spectral variation in the local resonances enables a spatially-varying phase profile.

Finally, we summarize the advancements provided in this thesis regarding the fabrication and measurement of nonreciprocal thermal emitters as well as the simulation, fabrication, and characterization of thermal emitters with a spatial phase profile. We then look forward to what can be done in future research to continue improving upon the concepts and tools presented throughout this thesis.

References

[1] S. A. Maier, *Plasmonics: Fundamentals and Applications* (Springer, 2007).

[2] M. Planck. Ueber das Gesetz der Energieverteilung im Normalspectrum, *Ann. der Physik* **4**, 553-563 (1901).

[3] G. R. Fowles, *Introduction to Modern Optics* (Dover, 1989).

[4] J. D. Joannopoulos, S. G. Johnson, J. N. Winn, R. D. Meade, *Photonic Crystals* (Princeton University Press, 2008).

[5] N. Yu, F. Capasso, Flat optics with designer metasurfaces. *Nature Materials* **13**, 139-150 (2014).

[6] J.-J. Greffet, et al. Coherent emission of light by thermal sources. *Nature* **416**, 61-64 (2002).

[7] X. Liu, et al. Taming the blackbody with infrared metamaterials as selective thermal emitters. *Phys. Rev. Lett.* **107**, 045901 (2011).

[8] A. Lochbaum, et al. On-chip narrowband thermal emitter for mid-IR optical gas sensing. *ACS Photonics* **4**, 1371-1380 (2017).

[9] H. Chalabi, A. Alu, & M. L. Brongersma. Focused thermal emission from a nanostructured SiC surface. *Phys. Rev. B* **94** 094307 (2016).

[10] A. C. Overvig, S. A. Mann, & A. Alu. Thermal metasurfaces: complete emission control by combining local and nonlocal light-matter interactions. *Phys. Rev. X* **11** 021050 (2021).

[11] D. G. Baranov, et al. Nanophotonic engineering of far-field thermal emitters. *Nature Materials* **18**, 920-930 (2019).

[12] A. P. Raman, M. A. Anoma, L. Zhu, E. Rephaeli, S. Fan. Passive radiative cooling below ambient air temperature under direct sunlight. *Nature* **515**, 540-544 (2014).

[13] L. Zhu & S. Fan. Near-complete violation of detailed balance in thermal radiation. *Phys. Rev. B* **90**, 220301 (2014).

[14] M. A. Green. Time-asymmetric photovoltaics. *Nano Letters* **12**, 5985-5988 (2012).

[15] S. Yang, M. Liu, C. Zhao, S. Fan, & C.-W. Qiu. Nonreciprocal thermal photonics. *Nature Photonics* **18**, 412-424 (2024).

Chapter 2

Nonreciprocal infrared absorption

2.1 Motivation and introduction to Lorentz nonreciprocity

Nonreciprocal elements are a vital building block of electrical and optical systems. In the infrared regime, there is a particular interest in structures that break reciprocity because their thermal absorptive (and emissive) properties should not obey the Kirchhoff thermal radiation law.

Reciprocity can be broken with linear time-invariant, nonlinear, and linear time-varying platforms [1, 2, 3, 4]. In this section, we focus on magneto-optical methods of realizing nonreciprocal photonic behavior. The use of magneto-optical materials, e.g., ferrites, in basic optical elements such as isolators and circulators has been a basic component in integrated photonics for many decades. The use of bare magneto-optical materials to observe free-space radiation from coupled plasmon-phonon modes has been demonstrated, however the wavelength regimes thus far are limited to the far-infrared and the dependence on magnetic field was not measured [5].

Prior experimental work on free-space magneto-optical elements has investigated coupling to surface plasmon resonances at a fixed incidence angle in the Otto configuration in the far-infrared regime [6], as well as polarization rotation in the Faraday geometry [7, 8]. Pairing magneto-optical semiconductors with photonic crystals and examining the magnetic field and angular dependence in the infrared has not yet been experimentally explored. Despite an abundance of theoretical designs reporting free-space isolation with magneto-optical elements in this wavelength regime [9, 10, 11], experimental realizations are lacking.

This chapter is adapted from K. J. Shayegan, B. Zhao, Y. Kim, S. Fan, H. A. Atwater, Nonreciprocal infrared absorption via resonant magneto-optical coupling to InAs. *Sci. Adv.* **8**, eabm4308 (2022).

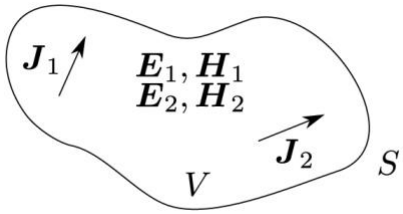

Figure 2.1 Conceptual diagram where two current sources, $\boldsymbol{J}_1$ and $\boldsymbol{J}_2$, induce electric and magnetic fields $\boldsymbol{E}_1$, $\boldsymbol{H}_1$ and $\boldsymbol{E}_2$, $\boldsymbol{H}_2$, respectively. The sources are both enclosed by surface, *S*. This figure is reproduced from reference [12].

To understand how Lorentz reciprocity is broken, we first derive the Lorentz reciprocity theorem (adapted from [12]). Consider a volume containing to sets of current sources, $\boldsymbol{J}_1$ and $\boldsymbol{J}_2$. These two sources induce electric and magnetic fields $\boldsymbol{E}_1$, $\boldsymbol{H}_1$ and $\boldsymbol{E}_2$, $\boldsymbol{H}_2$, respectively (see Figure 2.1).

Taking the divergence of the quantity $(\boldsymbol{E}_1 \times \boldsymbol{H}_2 - \boldsymbol{E}_2 \times \boldsymbol{H}_1)$ (Eq. 2.1) and expanding, we get

$$(\nabla \times \boldsymbol{E}_1) \cdot \boldsymbol{H}_2 - (\nabla \times \boldsymbol{H}_2) \cdot \boldsymbol{E}_1 - (\nabla \times \boldsymbol{E}_2) \cdot \boldsymbol{H}_1 + (\nabla \times \boldsymbol{H}_1) \cdot \boldsymbol{E}_2 \qquad \text{(Eq. 2.2)}$$

From Maxwell's curl equations,

$$\nabla \times \boldsymbol{E}_1 = -j\omega\mu\boldsymbol{H}_1 \qquad \text{(Eq 2.3)}$$

$$\nabla \times \boldsymbol{H}_1 = j\omega\varepsilon\boldsymbol{E}_1 + \boldsymbol{J}_1 \qquad \text{(Eq 2.4)}$$

$$\nabla \times \boldsymbol{E}_2 = -j\omega\mu\boldsymbol{H}_2 \qquad \text{(Eq 2.5)}$$

$$\nabla \times \boldsymbol{H}_2 = j\omega\varepsilon\boldsymbol{E}_2 + \boldsymbol{J}_2 \qquad \text{(Eq 2.6)}$$

Through substitution, the quantity in Eq. 2.1 simplifies to

$$\nabla \cdot (\boldsymbol{E}_1 \times \boldsymbol{H}_2 - \boldsymbol{E}_2 \times \boldsymbol{H}_1) = \boldsymbol{J}_1 \cdot \boldsymbol{E}_2 - \boldsymbol{J}_2 \cdot \boldsymbol{E}_1 \qquad \text{(Eq. 2.7)}$$

If one assumes that the permeability, μ, and permittivity, ε, tensors are symmetric. This must be the case, or the cancellation of the $\boldsymbol{H}$ and $\boldsymbol{E}$ terms does not occur in Eq. 2.7. When the tensors are anti-symmetric, as is the case for magneto-optic materials, the equality in Eq. 2.11 will not occur. If we integrate over the volume containing both sources, Eq. 2.7 becomes

$$\iiint_V \nabla \cdot (\boldsymbol{E}_1 \times \boldsymbol{H}_2 - \boldsymbol{E}_2 \times \boldsymbol{H}_1) dv' = \iiint_V \boldsymbol{J}_1 \cdot \boldsymbol{E}_2 - \boldsymbol{J}_2 \cdot \boldsymbol{E}_1 dv' \qquad \text{(Eq. 2.8)}$$

Applying the divergence theorem to the left-hand side of Eq. 2.8

$$\oiint_S (\boldsymbol{E}_1 \times \boldsymbol{H}_2 - \boldsymbol{E}_2 \times \boldsymbol{H}_1) ds' = \iiint_V \boldsymbol{J}_1 \cdot \boldsymbol{E}_2 - \boldsymbol{J}_2 \cdot \boldsymbol{E}_1 dv' \quad \text{(Eq. 2.9)}$$

In the limit of $S \rightarrow \infty$, $\boldsymbol{E}_1$ and $\boldsymbol{H}_2$become spherical waves, which are approximated as plane waves sharing the same β (propagation) vector. Through this plane-wave approximation, the left-hand side of Eq. 2.9 simplifies to zero:

$$\boldsymbol{E}_1 \times (\beta \times \boldsymbol{E}_2) - \boldsymbol{E}_2 \times (\beta \times \boldsymbol{E}_1) = \boldsymbol{E}_1 (\beta \cdot \boldsymbol{E}_2) - \beta(\boldsymbol{E}_1 \cdot \boldsymbol{E}_2) - \boldsymbol{E}_2 (\beta \cdot \boldsymbol{E}_1) + \beta(\boldsymbol{E}_2 \cdot \boldsymbol{E}_1) \quad \text{(Eq. 2.10)}$$

Finally, we arrive at the conventional form of the Lorentz reciprocity theorem:

$$\iiint_V \boldsymbol{J}_1 \cdot \boldsymbol{E}_2 \, dv' = \iiint_V \boldsymbol{J}_2 \cdot \boldsymbol{E}_1 \, dv' \quad \text{(Eq. 2.11)}$$

In words, the fields generated by a source at position 1 as measured by source 2 is equal to the fields generated by the source 2 as measured by source 1 [13].

The Kirchhoff thermal radiation law can consequently be expressed as an equality of the absorptivity and emissivity at a given wavelength (λ), polarization, and angle of incidence (θ_i) [14, 15, 16]:

$$\alpha(\theta_i, \lambda) = e(\theta_i, \lambda) \quad \text{(Eq. 2.12)}$$

This equality between the angular and spectral distributions of the emissivity and absorptivity is a direct consequence of Lorentz reciprocity, which in a scattering context takes the form:

$$r(\theta_i, \lambda) = r(-\theta_i, \lambda) \quad \text{(Eq. 2.13)}$$

where $r(\theta_i, \lambda)$ is the incident radiation from θ_i that is not absorbed by the absorber/emitter and reflected through the $-\theta_i$ channel and vice-versa for $r(-\theta_i, \lambda)$. The above relationships, however, assume that the emitter/absorber obeys Lorentz reciprocity and does not transmit any of the incident radiation [17]. In a nonreciprocal system, the equality in Equation 2.13 is broken; and the Kirchhoff law is violated [18]. The nonreciprocal behavior of the reflection directly relates to the nonreciprocal thermal radiation. This relation is visualized in Figures 2.2 a, b.

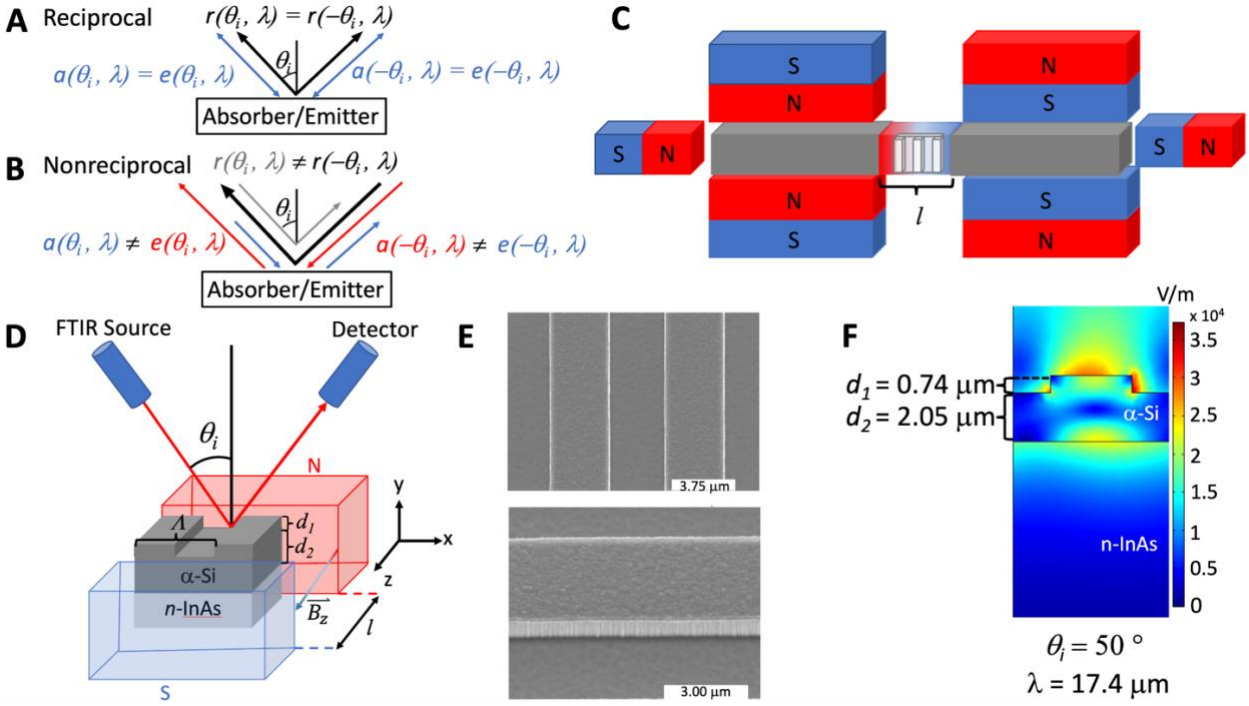

Figure 2.2 Overview of nonreciprocal absorber/emitter theory, design, and implementation. **(a** & **b)** Reciprocal and nonreciprocal relations for an absorber/emitter. **(c)** Schematic of the Halbach array used in the measurement. The poles of the magnets on each side of the system are rotated by 90° relative to one another to increase the magnitude of the magnetic field through the pole pieces (gray). The pole pieces provide a focused and uniform magnetic field across the sample, which is shown in the gap. We tune the magnetic field strength by changing the gap length, *l*, between the pole pieces. **(d)** Schematic of the measurement scheme. A silicon carbide Globar is used as the thermal source inside of a Fourier transform infrared (FTIR) spectrometer. The sample is mounted on a rotating stage which controls the angle of incidence, θ_i, from the source onto the sample. The detector is mounted on a rotating arm to collect the specular reflected light. Polarizers at the source output and detector input allow polarization-dependent measurements. (**e**) Scanning electron microscope (SEM) images of the α-Si photonic crystal slab with no tilt (top), and 45° tilt (bottom). (**f**) Simulation showing the electric field intensity for 50° incident radiation at 17.3 mm with the measured α-Si parameters from the SEM images.

We experimentally demonstrate strong nonreciprocal behavior, breaking the reflectivity relationship in Equation 2.13 over a wide range of incident angles in an infrared thermal photonic absorber that incorporates magneto-optic InAs with a static external magnetic field [19]. To apply the external magnetic field, we use a Halbach array consisting of three permanent magnets with their fields oriented towards a pole-piece (Figure 2.2 c) [20]. The pole-piece is made of a soft ferromagnetic alloy which focuses the magnetic field so that it is uniform over the sample. We control the strength of the field through the sample by tuning the length of the gap, *l*, between the

two pole-pieces (Figures 2.2 c, d). The maximum field used in this paper is limited by the sample size, 5 mm.

Our device consists of a low-loss, amorphous silicon (α-Si) GMR waveguide structure fabricated on the surface of a 500-μm-thick, degenerately *n*-type doped InAs wafer (Figures 2.2 d, e) serving as our magneto-optical material resonantly excited in the Voigt geometry. The patterned α-Si structure on the InAs gives a clear angle-dependent guided mode dispersion relation with distinct resonances for both the zero and non-zero magnetic field cases. While most of the modal field of a guided mode is confined within a low-loss α-Si resonator, some of the modal field penetrates the magneto-optic InAs layer below, which produces the nonreciprocal effect in the presence of a magnetic field (Figure 2.2 f).

2.2 Drude model of InAs permittivity

The doping concentration of the InAs is chosen such that the GMR wavelength coincides with the ENZ wavelength (17.3 μm) in the infrared. The degenerately-doped InAs exhibits a Drude-like optical response with non-zero off-diagonal permittivity values in an applied magnetic field:

$$\varepsilon(\omega) = \begin{bmatrix} \varepsilon_{xx} & \varepsilon_{xy} & 0 \\ \varepsilon_{yx} & \varepsilon_{yy} & 0 \\ 0 & 0 & \varepsilon_{zz} \end{bmatrix} \quad \text{(Eq. 2.14)}$$

$$\varepsilon_{xx} = \varepsilon_{yy} = \varepsilon_{\infty} - \frac{\omega_p^2(\omega + i\Gamma)}{\omega[(\omega + i\Gamma)^2 - \omega_c^2]} \quad \text{(Eq. 2.15)}$$

$$\varepsilon_{xy} = -\varepsilon_{yx} = i\frac{\omega_p^2\omega_c}{\omega[(\omega + i\Gamma)^2 - \omega_c^2]} \quad \text{(Eq. 2.16)}$$

$$\varepsilon_{zz} = \varepsilon_{\infty} - \frac{\omega_p^2}{\omega(\omega + i\Gamma)} \quad \text{(Eq. 2.17)}$$

In Equations 2.15 - 2.17, the plasma and cyclotron frequencies are $\omega_p = \sqrt{ne^2/(m_e\varepsilon_0)}$ and $\omega_c = eB/m_e$, respectively. Four-point probe measurements of the InAs wafer in conjunction with ellipsometry fits of the values Ψ and Δ, the complex ratio amplitude and phase responses,

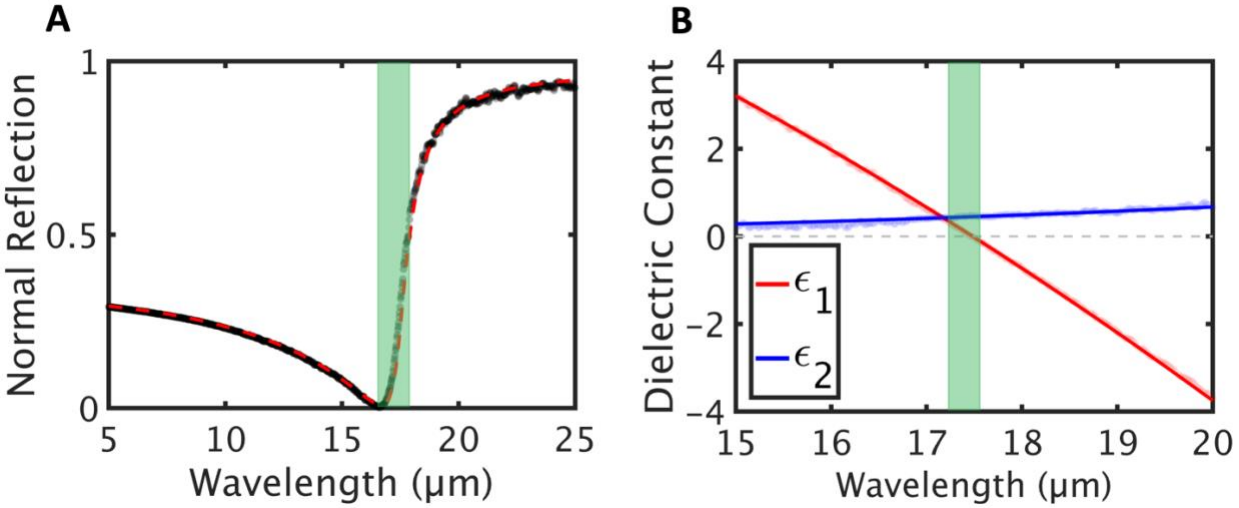

Figure 2.3 Drude reflectance and dielectric constant of degenerately-doped *n*-InAs. (**a**) Drude reflectance of the InAs wafer. The transparent black dots show the measured data and the dashed red curve gives the fit for a Drude-like optical response with $n = 1.5 \times 10^{18}$ cm^{-3}, and Γ = 4.5 THz. (**b**) Real and imaginary parts of the dielectric function for the isotropic case. The transparent dots mark the permittivity values directly calculated from the data, and the solid blue and red curves show the extracted values from fitting the ellipsometry values Ψ and Δ. The chartreuse strips mark ENZ wavelength regime where we expect to see large nonreciprocal behavior.

give a relaxation rate Γ = 4.5 THz, a high-frequency limit dielectric constant ε_∞= 12.3, a carrier concentration $n = 1.5 \times 10^{18}$ cm^{-3}, and an effective electron mass $m = 0.033\, m_e$, where $m_e = 9.109 \times 10^{-31}$ kg [21]. The Drude model fit to the experimental values is shown in Figure 2.3 a. Furthermore, our designs target the ENZ wavelength regime (17.3 μm) since the off-diagonal terms of the dielectric function ($\varepsilon_{xy}, \varepsilon_{yx}$) are largest relative to the on-diagonal terms when a magnetic field is applied to the InAs at this wavelength (Figure 2.3 b).

2.3 Design and fabrication of guided mode resonant structure

We implement targeted wavelength control with a GMR structure, which is commonly employed to enhance absorption/reflection by critical coupling in infrared applications [22, 23, 24, 25]. We design the GMR structure to critically couple to *p*-polarized free-space radiation, (i.e., electric field oscillating in the *x*-*y* plane), near the ENZ wavelength over a range of angles, with the guided resonance in the absorber. Because the resonator has been designed around the ENZ wavelength, we see a strong detuning of a resonant peak with a magnetic field. If no patterned α-Si were used, the plasma edge of the InAs would have no distinct resonance that could be detuned with a magnetic field. This effect is discussed in more detail in the following section.

The optimal dimensions for the GMR structure are found based on an analysis of the guided mode in a *uniform* α-Si slab atop *n*-InAs. In this approximation of the periodic α-Si, the uniform α-Si has a thickness $t = d_1/2 + d_2$, where d_1 is the periodic element depth and d_2 is the supporting layer thickness of the α-Si. The dispersion relation, $\omega(k_x)$, of the fundamental guided mode is then found by solving the equation [26, 27]:

$$\tan(k_{Si}t) = \frac{k_{Si}\varepsilon_{Si}[k_{air} + k_{InAs}\xi_{xx}]}{{k_{Si}}^2 - {\varepsilon_{Si}}^2 k_{air}k_{InAs}\xi_{xx}} \qquad \text{(Eq. 2.18)}$$

where $k_{Si} = \sqrt{Re(\varepsilon_{Si})(\omega/c)^2 - {k_x}^2}$, $k_{air} = \sqrt{{k_x}^2 - (\omega/c)^2}$, $k_{InAs} = \sqrt{{k_x}^2 - (\omega/c)^2 Re(\varepsilon_{InAs})}$, $\xi_{xx} = 1/Re(\varepsilon_{InAs})$, and k_x is the wavevector along the direction of propagation. In this derivation, we focus on the reciprocal case to get a sense of matching the slab waveguide to the Drude-like resonance of the InAs and neglect the off-diagonal terms of the InAs which are zero when there is no applied magnetic field. In reference 28, the derivation for the non-zero magnetic field case shows that $\omega(k_x) \neq \omega(-k_x)$ and the symmetry of the dispersion relation is broken.

We use the COMSOL *electromagnetic waves, frequency domain* package to simulate the optical response of the GMR structure. For the material properties and geometries of the structure,

we use the measured values of the α-Si periodicity and depth from SEM images and *n*-InAs optical properties from the model fits of ellipsometry data and four-point probe measurements. For each trace at a fixed angle of incidence, we swept the wavelength from 16 to 19 μm in 12-nm intervals. The absorptivity was found by subtracting the reflectivity from 1, as there was no transmission for the structure. This is verified by taking transmission measurements of the *n*-InAs wafer.

A plot of the symmetric angular dispersion for varying slab thicknesses of the α-Si waveguide is provided in Figure 2.4. In the calculations, we use the fitted dielectric constant values of the *n*-InAs from ellipsometry.

We choose a periodicity (Λ) of 7 μm such that the guided mode can be folded in the light cone and couple with the free-space radiation. We fine-tune the other dimensions and used a GMR structure depth d_1 = 0.72 μm, and supporting layer thickness d_2 = 2.1 μm. Since the periodicity of the GMR structure itself is much smaller than the wavelength of interest, we expect to see only specular reflection in the considered wavelength range [28]. We note that the linewidth of the resonance created by the GMR structure is sensitive to both the patterned area widths (Λ / 2) and the scattering rate of the *n*-InAs underneath [29].

Our fabrication of the GMR structure started by deposition of α-Si on the InAs wafer using plasma-enhanced chemical vapor deposition (PECVD). The deposition was carried out at a temperature of 200 °C and pressure of 800 mTorr with a flow rate of 250 SCCM (5% SiH_4/Ar) for 90 seconds. We then spin-coated 500 nm of ZEP 520A resist (1 minute at 2,000 rpm) and baked the sample for 5 minutes at 180 °C on a hot plate.

Electron beam lithography was then used to write the desired pattern into the resist, using a beam current of 100 nA with a 300 mm aperture and a dose of 240 mC/cm^2. After writing the pattern into the resist, the sample was dipped in ZED N-50 for 2 minutes and 30 seconds for development. Following exposure, the sample was baked at 140 °C for 3 minutes.

The α-Si pattern was subsequently etched using inductively coupled plasma-enhanced reactive ion etching (ICP RIE). The etching recipe began with an O_2 followed by a SF_6 cleaning cycle for 10 minutes each followed by 2 minutes and 30 seconds of etching with SF_6 as the etchant gas. The same cleaning cycle was then repeated in reverse. The sample was left in PG remover overnight and then checked with a confocal microscope to ensure the resist had been removed.

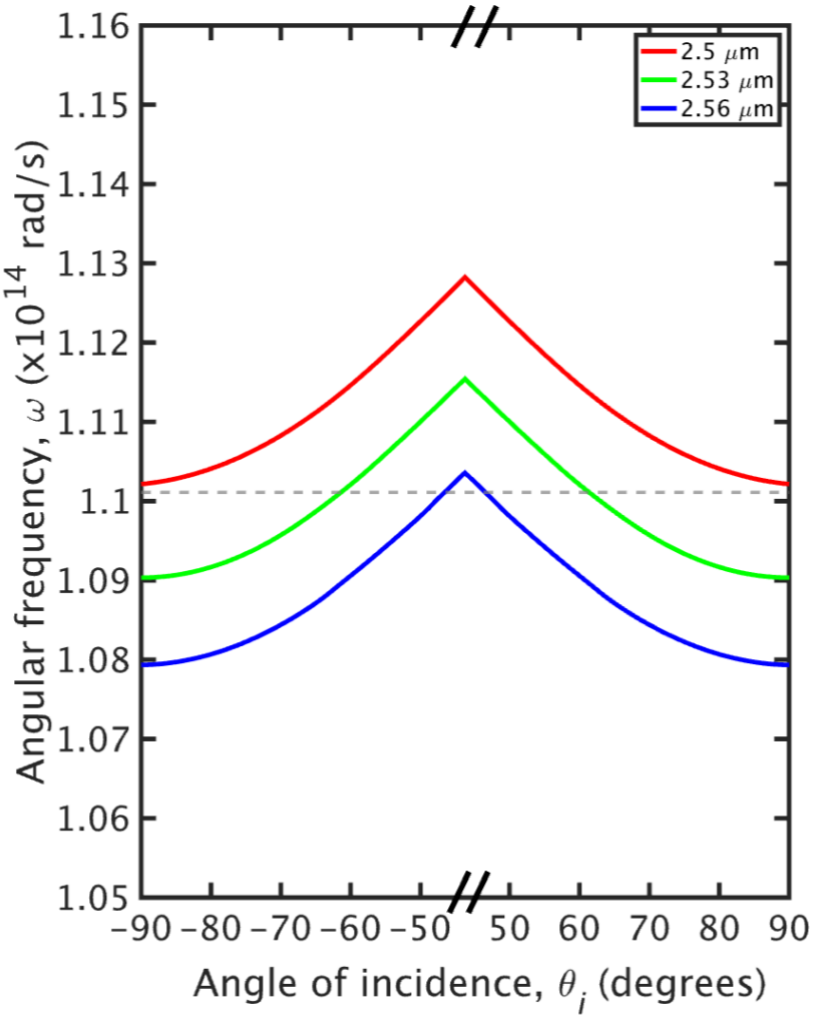

Figure 2.4 Slab waveguide angular dispersion for varying α-Si layer thicknesses, *t*, on top of *n*-InAs. The dispersion relation of the slab waveguide is found by solving Equation 2.18. The dashed gray line (1.101 x 10^{14} rad/s, or 17.2 μm) is the same as the one used in the comparison of the experimental and simulated traces in Figure 2.9 as a reference for the reader. The dispersion for t = 2.5 μm is closest to the dimensions used in our experiment (and simulations). There is a considerable shift in theory for the solution to the dispersion for a small change in α-Si thickness, with the dispersion shifting to lower frequencies (longer wavelengths) for a thicker slab layer.

2.4 Nonreciprocal infrared absorptivity measurement

To probe the sample, we use a two-theta stage with a silicon carbide Globar source and focusing optics, exciting the sample at an incident angle θ_i relative to the *x*-*z* plane and collect the specular reflected light at $-\theta_i$. For the zero and low (up to but not including 0.8 T) magnetic field measurements, the original sample holder of the system (J. A. Woollam I.R. VASE Mark II) was used. For higher magnetic field measurements, we use a separate adapter to accommodate the Halbach array. The lower magnetic field measurements are obtained using a specially-designed aluminum holder to separate the two neodymium magnets while holding the sample in between the two magnets' poles. The field strength was tuned by inserting aluminum spacers to increase the gap between the magnets. We used a Halbach array magnet configuration with tunable pole pieces to apply $0.8 < B < 1.2$ T [30]. An image of the magnet assembly can be found in Figure 2.5. We measured the magnetic field strength and uniformity across the sample surface with a transverse Hall sensor made from InAs (Lakeshore HGT 1010).

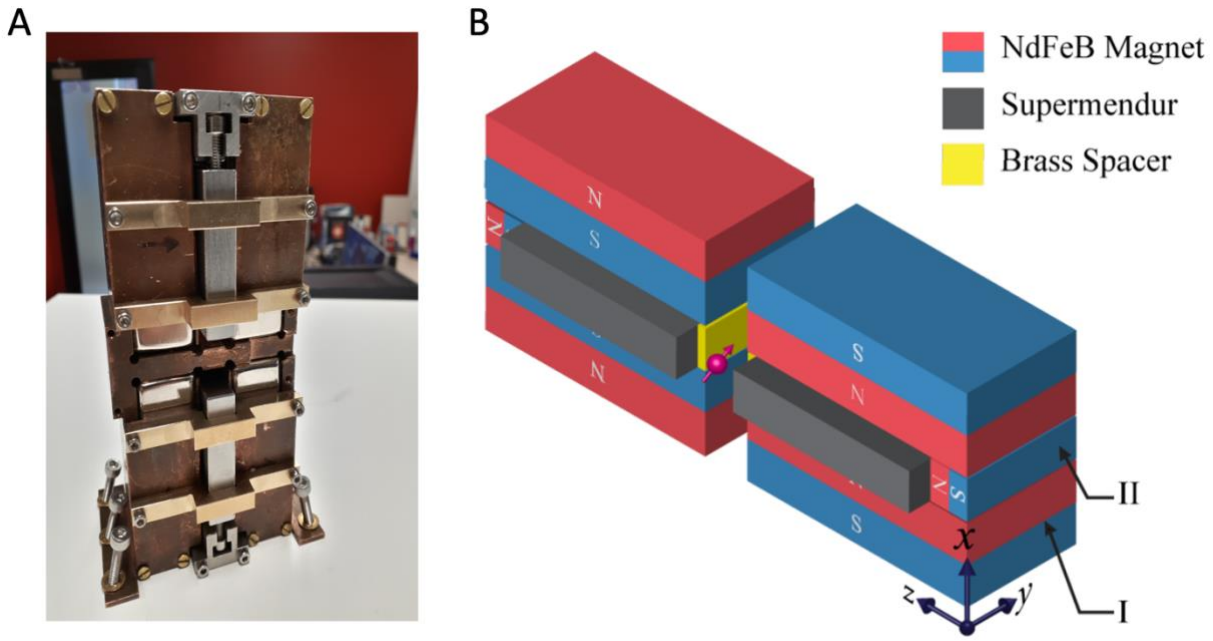

Figure 2.5 Image and schematic of the Halbach array with tunable supermendur pole pieces. Both the image and the schematic are courtesy of Chris Adambukulam and Arne Laucht. In the image, the magnets are housed in a brass and copper enclosure. The schematic shows the magnet rotated 90°. The original use of the magnet was for cryogenic qubit measurements.

The sample was in the Voigt geometry, with an in-plane magnetic field, B, breaking time-reversal symmetry. By changing the sign of the magnetic field, we produced the same effect as keeping the sign of magnetic field constant while switching the positions of the source and detector [31, 32, 33]. The use of linear polarizers at both the source output and detector input allows for a deconvolution of the physical effects (e.g. ensure that there is no cross-polarization due to sample misalignment).

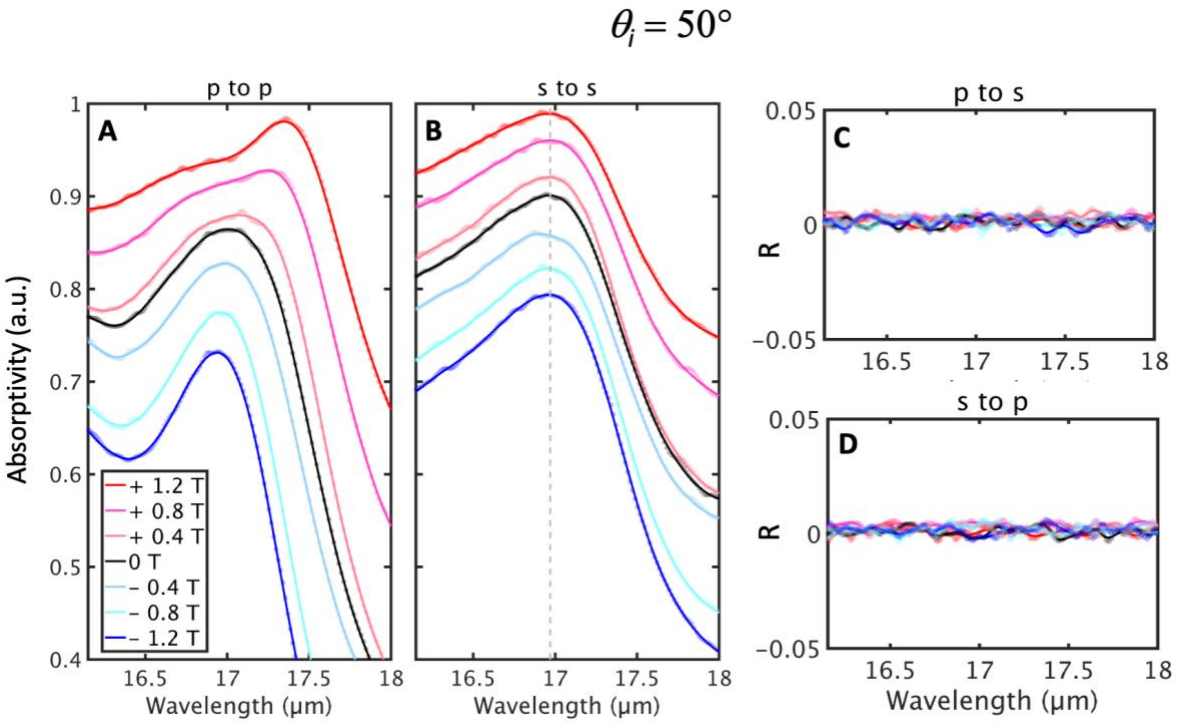

Figure 2.6 Polarization-dependent reflection measurements for varying applied magnetic field. (**a**) *p* to *p*-polarization, (**b**) *s* to *s*-polarization, (**c**) *s* to *p*-polarization, and (**d**) *p* to *s*-polarization. The dotted points are experimental data and the solid lines are fits to the data points. We only show data for the incident angle θ_i = 50° in this figure. We see a clear tuning of the peak position with magnetic field for *p* to *p*-polarization but no spectral shape change for *s* to *s*-polarization. We do not observe polarization conversion, further demonstrating that the change in the *p* to *p*-polarization is not due to misalignment of the device in the setup. The data in (a) and (b) are artificially offset to highlight the spectral peak shift (*p*-polarization) and no shift (*s*-polarization).

The Voigt geometry used in these experiments means that the nonreciprocal behavior of electromagnetic radiation inside of the InAs will be confined to *p*-polarized scattering, where the electric field oscillates perpendicular to the applied magnetic field (Figure 2.6 a). Conversely, we expect reciprocal behavior for *s*-polarized scattering, as the applied magnetic field is aligned with the oscillations in the electric field, and the cross product of the electric and magnetic fields is zero. The reciprocal behavior for *s*-polarized light is shown in Figure 2.6 b, where the absorptivity maxima for all magnetic field values are marked with a dashed gray line at approximately 17 μm. In Figures 2.6 a and b, we emphasize the spectral shift in the peak position of the absorptivity and offset the data for clarity. The overall absorptivity for *s*-polarized light does not change with varying magnetic field. Furthermore, we do not observe any detectable polarization conversion from *p* to *s* or *s* to *p*-polarization, confirming the proper alignment of our GMR structure relative to the optical beam path of the light (Figures 2.6 c, d). The InAs layer is optically thick and therefor no light is transmitted through the sample, allowing us to only measure the absorptivity and reflectivity. We observed a significant redshift of the absorptivity peak due to the GMR, especially in the positive field case (0 T to 1.2 T). The strong magnetic dependence of the absorptivity spectrum clearly demonstrates the reciprocity breaking effect. This nonreciprocal effect is observed in a wide angular and wavelength range.

To deconvolve the contributions coming from the *n*-type InAs and the entire GMR structure (*n*-type InAs with α-Si on top), we simulated angular absorption spectra as a function of magnetic field for both cases and compared the simulations to our measurements (Figure 2.7). The simulations were performed using a finite-difference, frequency-domain electromagnetic simulation tool, and incorporated the measured InAs optical properties and α-Si grating parameters. The simulated and measured plasma edge splitting for the unpatterned InAs wafer are in good qualitative agreement, with a broad resonance visible for the positive field surface magneto-plasmon and a shorter wavelength onset (16.5 μm) for the negative field surface magneto-plasmon (Figures 2.7 a, c). The addition of the periodic α-Si does not increase the wavelength shift, however clear maxima are seen from the coupled GMR structure that can be evaluated for multiple angles and compared to the data, which is further discussed in the following section.

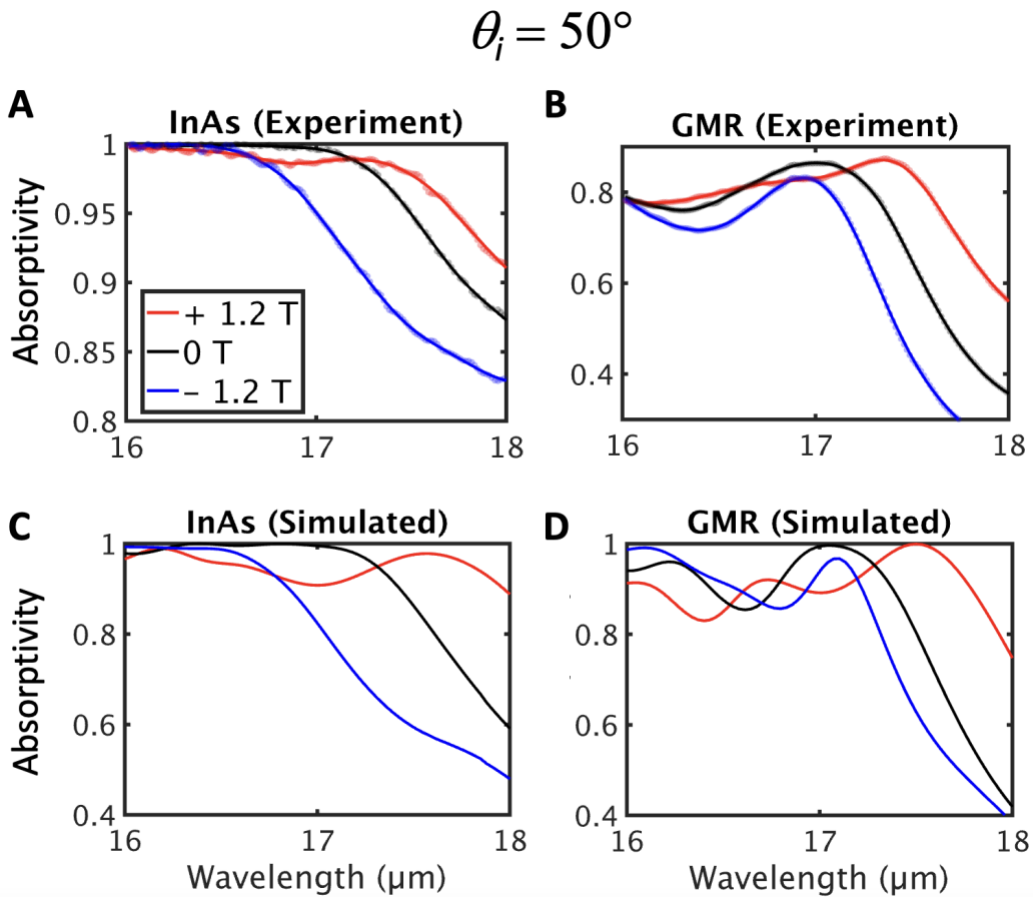

Figure 2.7 Magnetic field effect on *p*-polarized absorptivity spectra for bare InAs and the GMR structure at θ_i = 50°. (a) The measured shift in absorptivity of bare InAs as a function of magnetic field emanates from the splitting of the plasma edge in InAs into a positive (red) and negative (blue) magneto-plasmon. (**b**) Data for the GMR structure, showing the effect of adding the α-Si structure on top of the InAs wafer, which produces resonant absorptivity peaks for both positive and negative applied magnetic fields. Panels **c** and **d** show the simulated results for bare InAs and the GMR structure, respectively.

Comparing the measured positive field for the GMR structure (Figure 2.7 b, red curve) and the simulation (Figure 2.7 d, red curve) we note that both maxima occur at a resonance centered at 17.5 μm. However, a second shoulder resonance is present in the simulation at 16.7 μm which is not easily visible in the experiment. The shoulder resonance is much weaker in the experiment likely because of the larger material loss in both the α-Si and InAs. Going from zero to negative applied magnetic field at a θ_i = 50° we did not see a large shift in the resonant peak position for either the simulation or the measurement, but do see the resonance narrowing for the negative field case. The simulated and experimental traces for more angles of incidence and an intermediary 0.8 T field are included in Figure 2.8.

For narrower angles where the magnetic field effect goes from divergent to convergent, (45° to 35° incidence), we see that there is a strong magnetic field effect that causes an absorption resonance at longer wavelengths for positive field. As we go to narrower angles, the magnetic field effect is weaker and the resonance at shorter wavelengths begins to dominate. This is also why for a stronger field, the linewidths narrow at narrow incidence angle compared to the weaker field case (i.e. the longer wavelength resonance corresponding to a shift in the plasma edge from a positive field dominates, as seen in Figure 2.6 a).

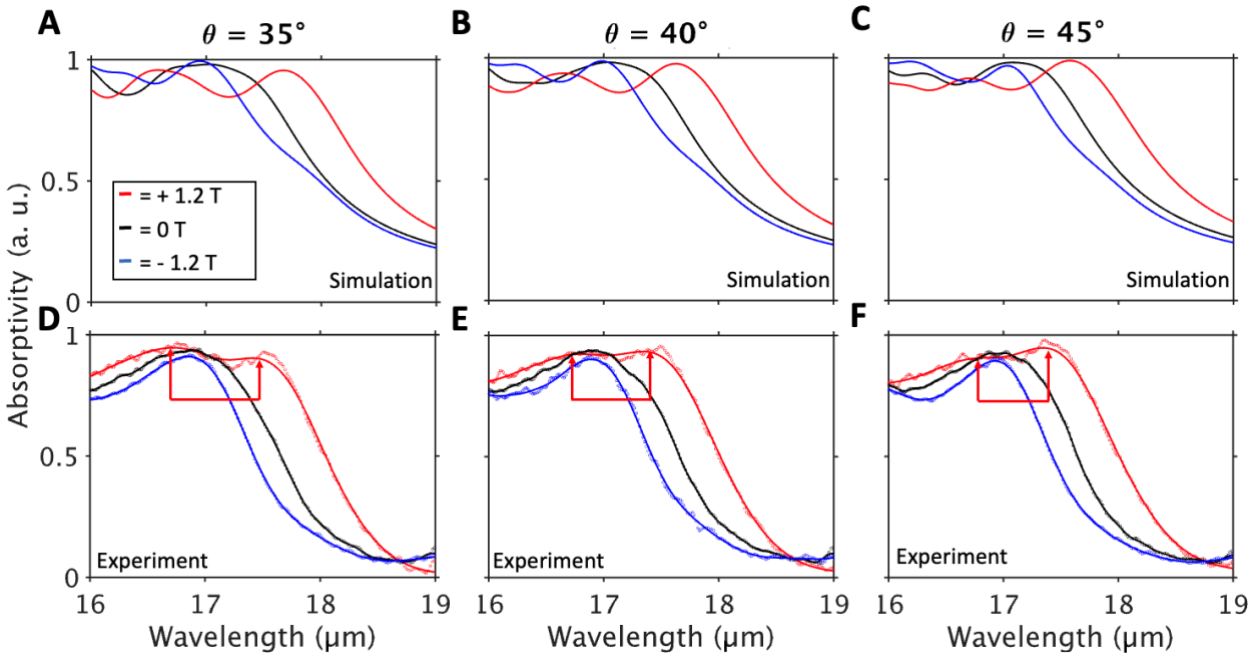

Figure 2.8 Simulated (a - c) and experimental (d - f) data on the narrow-angle transition from strong-to-weak nonreciprocal absorption. To better visualize the heatmap shown in Figure 2.8 c, we show linecuts of the simulated data with experimental data underneath. We mark with red arrows the shoulder peak that is not affected by a positive field at shorter wavelengths (left arrow in d - f) and the peak of the GMR that is strongly shifted by a positive magnetic field (right arrow in d - f).

To further highlight the effect of the GMR structure on nonreciprocal absorption, we look at the intensity effect on the absorption resonance at more oblique angles. Taking $\theta_i = 70°$, we can subtract the absorption of the bare InAs around the plasma shoulder from the GMR structure absorption and fit a Lorentzian to the difference (Figure 2.9). When the magnetic field is then turned on, the resonant intensity peak can be drastically tuned from absorption that greatly exceeds the plasma shoulder (positive field) to well below (negative field).

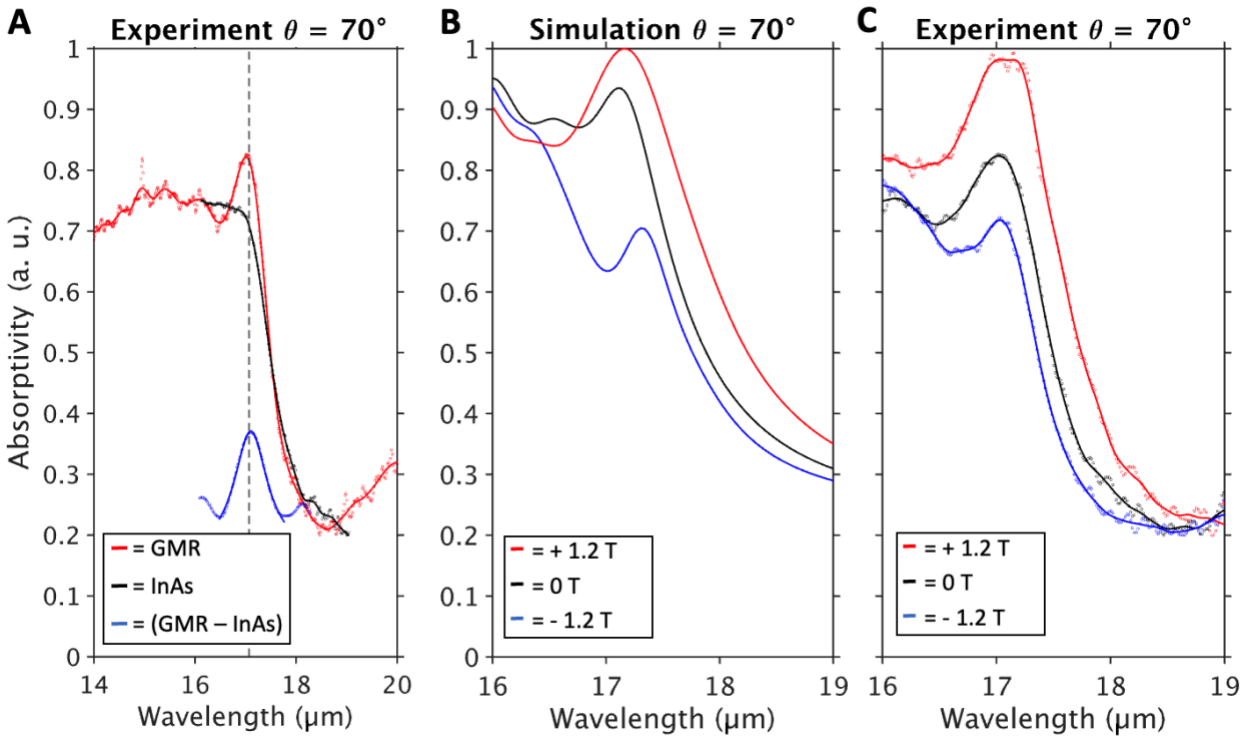

Figure 2.9 Intensity effect of GMR on nonreciprocal absorption at θ_i = 70°. (**a**) Experimental data at 70° incidence for the GMR structure and *n*-InAs with no patterned α-Si on top. The blue trace is the offset difference between the GMR and the *n*-InAs to highlight the resonant effect of the GMR. (**b** and **c**) Simulated and experimental data for positive and negative field showing the strong resonance intensity tuning at this angle.

To better understand and characterize the nonreciprocal response of the hybrid GMR structure, we compare the experimental and simulated absorptivity maxima for *p*-polarized light over a range of incidence angles for $B = 0$ T, 0.8 T, and 1.2 T. To map our dispersion across positive and negative angles, we confirm that Onsager-Casimir relations for reflectivity/absorptivity hold (Figure 2.10). A more thorough measurement and analysis of this is provided in the following chapter, specifically relating absorptivity and emissivity with a static, external magnetic field.

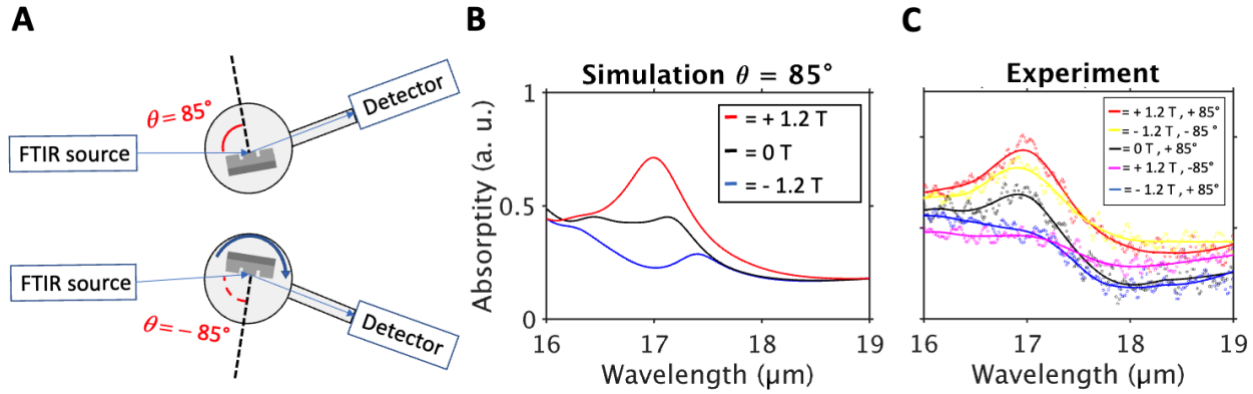

Figure 2.10 Schematic of reflection setup (a) and confirmation of the Onsager reciprocal relations (b and c). The sample and detector are mounted on a two-theta stage (with the FTIR source fixed). To test the Onsager-Casimir relations, which equate a negative magnetic field at positive incidence to a positive field at negative incidence, we look at the magnetic field effect at +/- 85° incidence (a). Unfortunately we cannot rotate the detector beyond -85° incidence. We then simulate 85° incidence for positive and negative fields (b) and compare the field effect at positive and negative incidence angles (c). What we observe is that the interchanging of field and incidence angle effects hold. A further discussion of the Onsager reciprocal relations pertaining to emissivity is provided in Chapter 3.

When $B = 0$ T, reciprocity is preserved, and we do not expect to see any reciprocity-breaking behavior. Consequently, the angular dispersion relation of the guided mode resonance at the plasma edge of the InAs remains symmetric. Figure 2.11 a shows the symmetric case measured in our experiment and the corresponding absorptivity maxima from simulations (Figure 2.11 d). We also observe a narrowing of the resonant linewidth for more oblique angles of incidence in both the simulated and experimental data when no magnetic field is applied, as shown by the vertical bars marking the full-width-at-5% maximum of each absorptivity spectrum. When the in-plane magnetic field is applied, reciprocity is broken, and the measured dispersion of the

absorptivity maxima becomes asymmetric (Figures 2.11 b, c). The degree of reciprocity breaking grows at smaller angles (approaching $\theta_i = 45°$), which is expected from the absorptivity maxima found from the simulations (Figure 2.11 e, f).

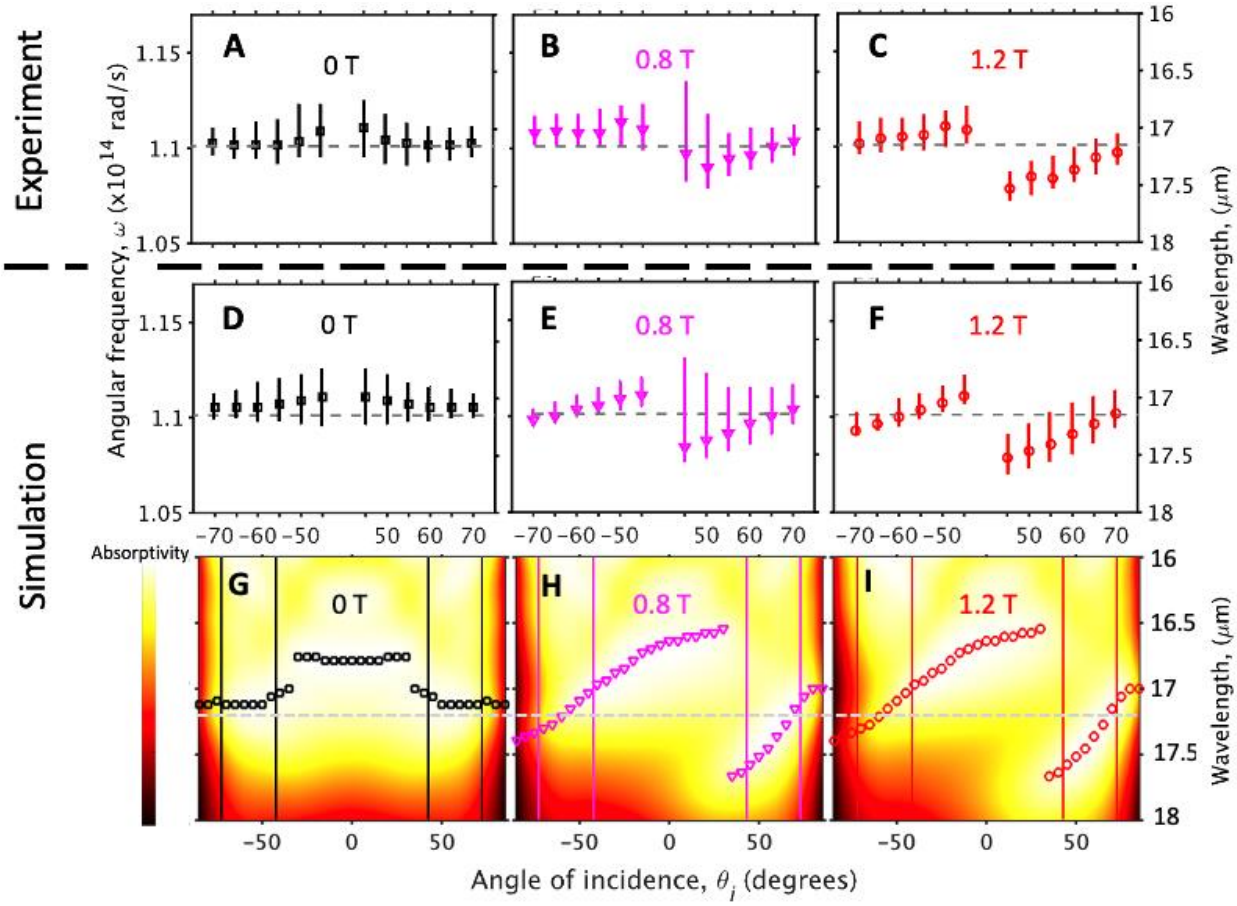

Figure 2.11 Magnetic field strength and angular dependence of reciprocity breaking. (**a** - **c**) Compiled experimental and simulated (**d** - **f**) absorptivity maxima for *p*-polarized light as a function of magnetic field and angle of incidence. When no magnetic field is applied (**a** & **d**) the structure behaves reciprocally. At 0.8 T (**b** & **e**) and 1.2 T (**c** & **f**) the *n*-InAs no longer satisfies Lorentz reciprocity and the reciprocal absorptivity relationship is broken. The error bars represent data points in the spectra to within 5% of the maximum value to give the reader an idea of the line shape. Plots of the individual spectra for other angles are included in Figure 2.10. (**g** - **i**) Heatmap of the simulated absorptivity over the entire angle of incidence range for varying magnetic fields. Horizontal lines mark the positive (and negative) incidence ranges shown in panels **a** - **f**.

We also observe a clear detuning of the absorptivity maxima with an increase in the magnetic field. For both the experimental (Figure 2.11 b) and simulated (Figure 2.11 e) absorptivity maxima at the intermediate 0.8 T magnetic field, the lineshape width for positive angles of incidence grows considerably. This makes the detuning of the absorptivity maxima at narrow incidence angles difficult to resolve. Increasing the magnetic field to 1.2 T separates the maxima at narrow angles such that the 5% bars do not overlap.

Unfortunately, our measurement system only allows for incidence angles down to 35°, limiting the ability to compare experiments and simulations for near-normal incidence. However, simulations indicate that the difference for positive and negative incidence (positive and negative field) decrease and approach zero as the scattering geometry approaches normal incidence since the first-order magneto-optic effects go to zero (Figure 2.11 g - i).

Interestingly, the measured maxima for negative incidence angles do not shift below the zero magnetic field maxima for oblique angles. This contrasts with the maxima extracted from simulations, which redshift for oblique (-65° and -70°) angles of incidence. A more quantitative analysis and categorization of the different GMR-plasma edge coupling is provided in Chapter 3, section 4.

2.5 Summary and outlook

In this chapter, we use a degenerately-doped magneto-optical semiconductor paired with a GMR coupled to free-space incident radiation to demonstrate nonreciprocal absorption in the infrared regime when a moderate magnetic field (B up to 1.2 T) bias is applied. The degree of reciprocity breaking is largest at narrower incidence angles θ_i (45° - 55°), making the design potentially useful for cascading multiple emitters/absorbers to achieve directional flow of energy [34]. The methods used to model, design, and fabricate the structure presented in chapter can be utilized for future implementations of nonreciprocal absorbers. As a future direction for engineering higher efficiency thermal radiators, direct measurement of the emissivity could be employed to demonstrate applications of systems that violate the Kirchhoff thermal radiation law, which is discussed in the following chapter. Higher quality factors of the structure could be obtained using a thinner magneto-optic layer with a back reflector or a lower doping concentration of InAs; however, this would result in a longer working wavelength. The easily identifiable

absorptivity peaks at the plasma edge are a consequence of using a periodic α-Si structure supporting a GMR, while the nonreciprocal behavior comes from the plasma-edge splitting of the magneto-optic *n*-type InAs. Beyond demonstrating nonreciprocal absorption in the infrared, hybrid magneto-optic and photonic crystal structures like those reported here are of potential interest for thermal radiation control and free-space information processing owing to the polarization-dependent response and low required magnetic fields for resonance tunability.

References

[1] A. Christofi, Y. Kawaguchi, A. Alu, A. B. Khanikaev, Giant enhancement of Faraday rotation due to electromagnetically induced transparency in all-dielectric magneto-optical metasurfaces. *Optics Express* **43**, 1838-1841 (2018).

[2] A. M. Mahmoud, A. R. Davoyan, N. Engheta, All-passive nonreciprocal metastructure. *Nature Comm.* **6**, 1-5 (2015).

[3] D. L. Sounas, A. Alù, Non-reciprocal photonics based on time modulation. *Nature Photonics* **11**, 774-783 (2017).

[4] Z. Yu, S. Fan, Complete optical isolation created by indirect interband photonic transitions. *Nature Photonics* **3**, 91-94 (2009).

[5] M. P. Hasselbeck, D. Stalnaker, L. A. Schlie, T. J. Rotter, A. Stintz, M. Sheik-Bahae, Emission of terahertz radiation from coupled plasmon-phonon modes in InAs. *Phys. Rev. B* **65**, 233203 (2002).

[6] J. Chochol, K. Postava, M. Cada, J. Pistora, Experimental demonstration of magneto-plasmon polariton at InSb(InAs)/dielectric interface for terahertz sensor application. *Scientific Reports* **7**, 1-7 (2017).

[7] I. A. Kolmychek, A. R. Pomozov, V. B. Novikov, A. P. Leontiev, K. S. Napolskii, T. V. Murzina, Anomalous birefringence and enhanced magneto-optical effects in epsilon-near-zero metamaterials based on nanorods' arrays. *Optics Express* **27**, 32069-32074 (2019).

[8] B. Fan, M. E. Nasir, L. H. Nicholls, A. V. Zayats, V. A. Podolskiy, Magneto-Optical Metamaterials: Nonreciprocal Transmission and Faraday Effect Enhancement. *Adv. Opt. Mat.* **7**, 1801420 (2019).

[9] Z. Tan, F. Fan, X. Dong, J. Cheng, S. Chang, Nonreciprocal terahertz beam steering based on magneto-optic metagratings. *Scientific Reports* **9**, 1-7 (2019).

[10] H. Wang, H. Wu, J.-Q. Zhou, Nonreciprocal optical properties based on magneto-optical materials: n-InAs, GaAs and HgCdTe. *Journ. Quant. Spectr. And Rad. Transfer* **206**, 254-259 (2018).

[11] Q. Mu, F. Fan, S. Chen, S. Xu, C. Xiong, X. Zhang, X. Wang, S. Chang, Tunable magneto-optical polarization device for terahertz waves based on InSb and its plasmonic structure. *Photonics Research* **7**, 325-331 (2019).

[12] S. V. Hum, *ECE 422 Lecture notes*, University of Toronto (2022).

[13] W. C. Chew, *ECE 604 Lecture notes*, Purdue University (2022).

[14] G. Kirchhoff, On the relationship between the emissivity and absorptivity of a body for heat and light. *Ann. Phys.* **109**, 275-301 (1860).

[15] M. Planck, *The Theory of Heat Radiation* (Forgotten Books, London, 2013).

[16] R. Siegel, J. Howell, *Thermal Radiation Heat Transfer*, 4th ed.; Taylor & Francis: London, 49 (2001).

[17] H.A. Lorentz, The theorem of Poynting concerning the energy in the electromagnetic field and two general propositions concerning the propagation of light. *Verl. K. Akad. W Amsterdam* **4**, 1-11 (1896).

[18] W.C. Snyder, Z. Wan, X. Li, Thermodynamic constraints on reflectance reciprocity and Kirchhoff's law. *Appl. Opt.* **37**, 3469 (1998).

[19] B. Zhao, Y. Shi, J. Wang, Z. Zhao, N. Zhao, S. Fan, Near-complete violation of Kirchhoff's law of thermal radiation with a 0.3 T magnetic field. *Optics Letters* **44**, 4204 (2019).

[20] C. Adambukulam, V. K. Sewani, S. Asaad, M. T. Madzik, H. G. Stemp, A. Morello, A. Laucht, An ultra-stable 1.5 Tesla permanent magnet assembly for qubit experiments at cryogenic temperatures. *Review of Scientific Instruments* **92**, 085106 (2021).

[21] S. Law, D.C. Adams, A. M. Taylor, D. Wasserman, Mid-infrared designer metals. *Opt. Express* **20**, 12155-12165 (2012).

[22] S. S. Wang, R. Magnusson, Theory and applications of guided-mode resonance filters. *Optics Letters* **32**, 2606-2613 (1993).

[23] J. Piper, S. Fan, Total Absorption in a Graphene Monolayer in the Optical Regime by Critical Coupling with a Photonic Crystal Guided Resonance. *ACS Photonics* **1**, 347-353 (2014).

[24] J. N. Liu, M. V. Schulmerich, R. Bhargava, B. T. Cunningham, Optimally designed narrowband guided-mode resonance reflectance filters for mid-infrared spectroscopy. *Optics Express* **19**, 24182-24197 (2011).

[25] Y. M. Qing, H. F. Ma, Y. Z. Ren, S. Yu, T. J. Cui, Near-infrared absorption-induced switching effect via guided mode resonances in a graphene-based metamaterial. *Optics Express* **27**, 5253-5263 (2019).

[26] L. Alcantara, *Electromagnetic Materials* (IntechOpen, 2018).

[27] S. Fan, J.D. Joannopoulos, Analysis of guided resonances in photonic crystal slabs. *Phys. Rev. B* **65**, 235112 (2002).

[28] L. Zhu, S. Fan, Near-complete violation of detailed balance in thermal radiation. *Phys. Rev. B* **90**, 1-3 (2014).

[29] A. Kamboj, L. Nordin, P. Petluru, A. J. Muhowski, D. N. Woolf, D. Wasserman, All-epitaxial guided-mode resonance mid-wave infrared detectors. *Appl. Phys. Lett.* **118**, 201102 (2021).

[30] C. Adambukulam, V. K. Sewani, S. Asaad, M. T. Madzik, H. G. Stemp, A. Morello, A. Laucht, An ultra-stable 1.5 Tesla permanent magnet assembly for qubit experiments at cryogenic temperatures. *Review of Scientific Instruments* **92**, 085106 (2021).

[31] V.S. Asadchy, M.S. Mirmoosa, A. Diaz-Rubio, S. Fan, S.A. Tetryakov, Tutorial on Electromagnetic Nonreciprocity and its Origins. *Proc. IEEE* **108**, 1694 (2020).

[32] H.B.G. Casimir, On Onsager's Principle of Microscopic Reversibility. *Rev. Mod. Phys.* **17**, 350 (1945).

[33] J. Meixner, Thermodynamic and kinetic treatment of thermoelectric effects in a magnetic field. *Ann. D. Physik* **40**, 165-180 (1941).
[34] Y. Park, B. Zhao, S. Fan, Reaching Ultimate Efficiency of Solar Energy Harvesting with a Nonreciprocal Multijunction Solar Cell.

Chapter 3

Direct Kirchhoff thermal radiation law violation

3.1 Motivation for direct emissivity measurements

While theoretical proposals for thermal emitter configurations that break Kirchhoff's law abound [1, 2, 3], experimental measurements that directly demonstrate an inequality in the absorptivity and emissivity have remained elusive. In this chapter, we directly measure the absorptivity and emissivity from a nonreciprocal photonic structure and directly observe a violation of Kirchhoff's law.

The top layer of this photonic structure consists of a GMR waveguide: a dielectric slab waveguide supporting a transverse magnetic (TM) mode that couples to free space through a grating formed on the top surface [4, 5] (Figure 3.1 a and b). Such resonant structures have been used to filter and enhance infrared absorption for thermal detectors [6] and light trapping for solar cells [7]. The bottom layer consists of degenerately-doped *n*-InAs which has a Drude-like optical response [8] with a significant magnetic field dependence near the epsilon-near-zero (ENZ) wavelength from free carrier contributions [9]. This is the same structure presented in Chapter 2; however we use a higher doping concentration of the *n*-InAs and thus re-design the GMR waveguide to match the ENZ wavelength of the InAs wafer.

Again, when a transverse magnetic field, B, is applied perpendicular to the plane of incidence (along the z-axis in Figs. 1 a), the permittivity tensor of the InAs develops finite off-diagonal contributions. The *n*-InAs free carrier density is $n = 3.0 \times 10^{18}$ cm^{-3}, the effective mass $m_e = 0.035\ m_0$, and the scattering rate $\Gamma = 5.1$ THz. The corresponding *n*-InAs ENZ wavelength is 12.9 μm.

This chapter is adapted from K. J. Shayegan, S. Biswas, B. Zhao, H. A. Atwater, Direct observation of the violation of Kirchhoff's law of thermal radiation. *Nature Photonics* **17**, 891-896 (2023).

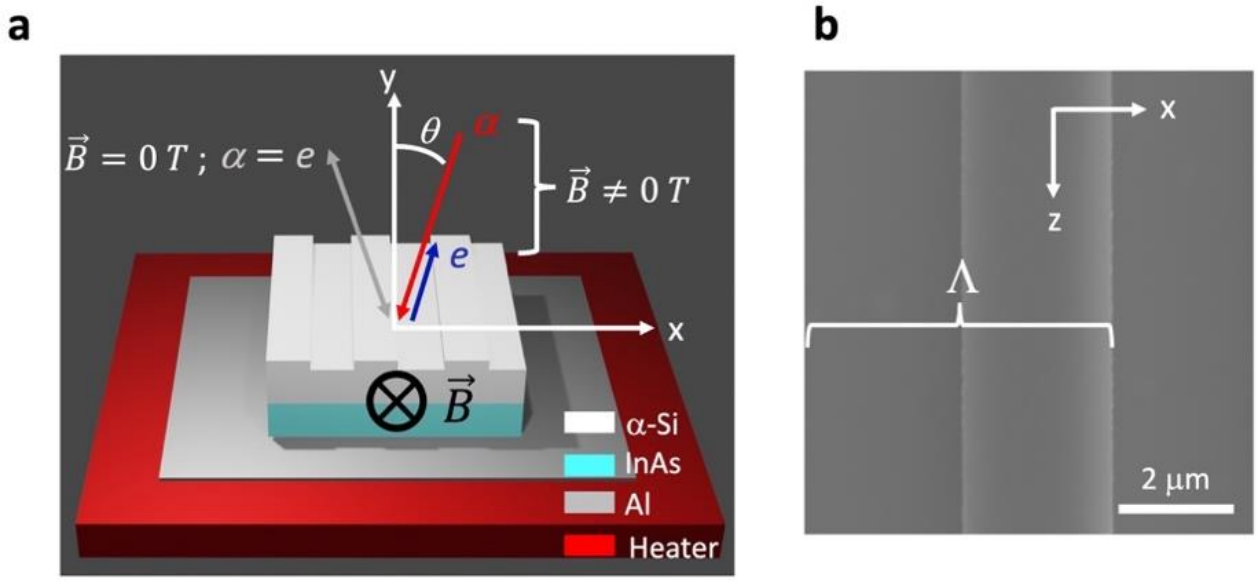

Figure 3.1: Schematic of magnetically-tunable emission and absorption of GMR structure coupled to *n*-InAs. (a and **b)** Schematic of the GMR structure on InAs. The GMR structure has a grating periodicity, Λ, of 5.5 μm, groove depth of 0.5 μm, and slab depth of 1.55 μm. In the case of no applied magnetic field, the absorptivity and emissivity channels are equal (left side, grey arrow). When a transverse magnetic field is applied along the z-direction, the absorptivity and emissivity (red and blue arrows, respectively) are tuned away from being equal in the same channel to being equal in opposite channels. The grating periodicity, Λ, is confirmed with SEM images.

3.2 Design considerations for direct emissivity measurements

We choose α-Si for the GMR structure due to its low loss in the infrared as compared to InAs as well as the well-developed and accessible deposition and etching techniques when compared to other low-loss dielectrics like SiC. As we heat the sample above room temperature, we observe a red shift in the $+1^{st}$ order guided mode (Figure 3.2 c). This temperature dependence seems at first glance counterintuitive, as one would naively expect a blue shift in the emission spectrum of a blackbody with increasing temperature [1] as well as an increase in the plasma frequency of *n*-InAs due to increasing carrier concentration. However, the spectral directional emissivity is determined by normalizing the collected emission of the sample by the emission from a blackbody reference, and the change in intrinsic carrier concentration in InAs over the range of temperatures (24 – 150° C) is two orders of magnitude lower than the doping concentration of our sample. For doped InAs and films of plasmonic materials with Drude-like optical responses [10], the increase in electron-phonon scattering with temperature results in a red shift of the on-diagonal permittivity zero-crossing wavelength.

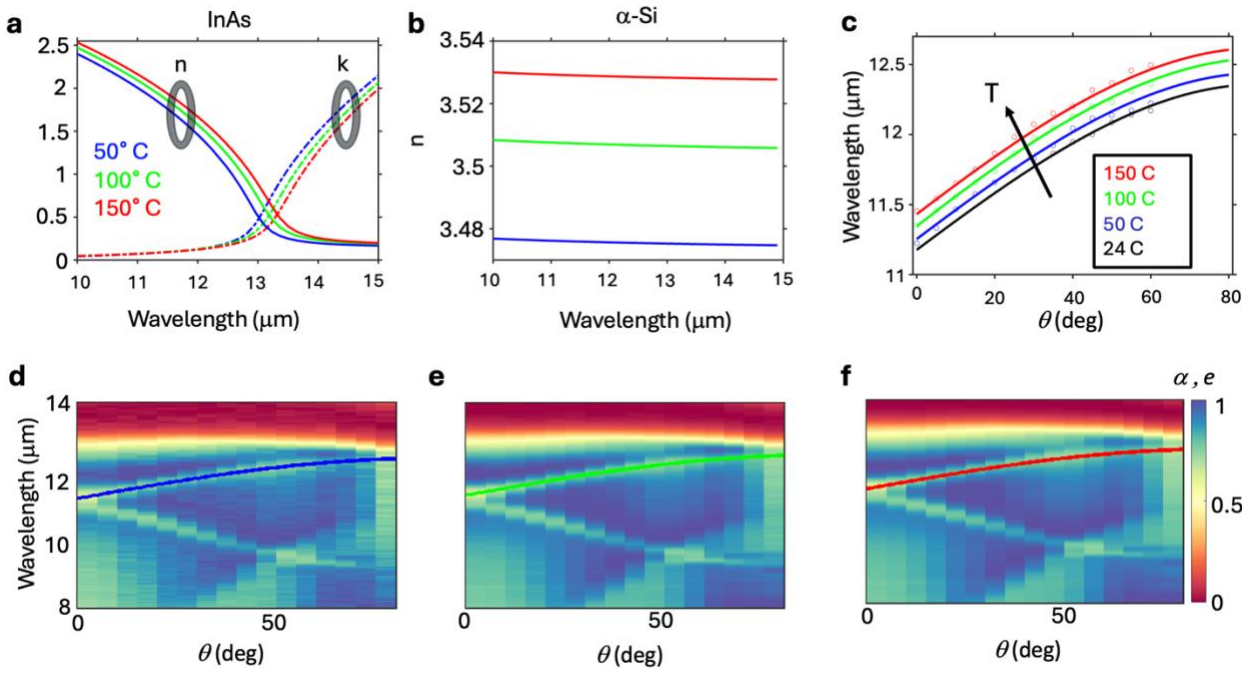

Figure 3.2: Temperature-dependent refractive indices of InAs and α-Si and heated emissivity measurements. (a) Refractive index values (n and k, solid and dot-dashed lines respectively) of the InAs wafer for various temperatures. We observe shifts in n and k that correspond to a redshifting of the ENZ-wavelength of the wafer. **(b)** Temperature-dependent refractive index values of the deposited α-Si. The refractive index grows as a function of temperature. The extinction coefficient is negligible in the wavelength range. (**c**) Experimental data (points) of the $+1^{st}$ order guided-mode branch through absorptivity (24° C, black) and emissivity (50° C, 100° C, and 150° C; blue, green, and red respectively) measurements; the curves represent theoretical calculations. The redshift in the GMR for a given θ is a consequence of shifts in the refractive indices of the α-Si and *n*-InAs as a function of temperature [11]. (**d** - **f**) Emissivity measurements taken at 50, 100, and 150° C, respectively. The blue, green, and red curves are obtained by solving Equation 3.1 using the average measured refractive index of α-Si at each temperature. Both (**a**) and (**b**) were measured and fitted using a J.A. Woollam IR-VASE and the WVASE software.

To carry out emissivity measurements in ambient conditions, we first need an understanding of the temperature-dependence of the optical properties of the constituent layers of our photonic structure. We do this via spectroscopic ellipsometry, where a parametrized fit of the amplitude and phase of the ratio of reflected *p*- and *s*-polarized light is used to model the refractive index of the sample.

We first measure the *p*- and *s*- polarized reflectance of the *n*-InAs wafer at 50° C, 100° C, and 150 °C and use a Drude model to extract the infrared refractive index (Figure 3.2 a). After building a model that captures the shift in the refractive index of the *n*-InAs at the given temperatures, we deposit a 2-μm-thick layer of α-Si on the wafer and measure the refractive index

again at the same set of temperatures. This is again done via spectroscopic ellipsometry, however we re-use the models for the bare InAs so that we are only fitting for the deposited α-Si layer at the given temperatures.

We observe an increase in the refractive index of the α-Si layer as a function of temperature (Figure 3.2 b). This shift can also be seen in our emissivity measurements, where the GMR redshifts with increasing temperature (Figure 3.2 c).

Solving a toy model of the +1st order guided mode branch which incorporates the refractive index of the α-Si for the upper and lower bounds of the resonance condition:

$$\gamma\, n_{\alpha-Si} - \Delta \leq n_{air} sin(\theta) - m\frac{\lambda}{\beta\Lambda} < \gamma\, n_{\alpha-Si} \qquad \text{(Eq. 3.1)}$$

where γ and β are scaling coefficients held constant over all temperature, $n_{\alpha-Si}$ is the refractive index of the α-Si layer, Δ is the average perturbation of the refractive index due to the presence of the grating, n_{air} is the refractive index of air, θ is the incident angle, m is the diffractive order, and Λ is the periodicity of the grating. Using the different refractive indices of $n_{\alpha-Si}$ at the three different temperatures, we track the GMR of our device for different temperatures (Figure 3.2 d-f).

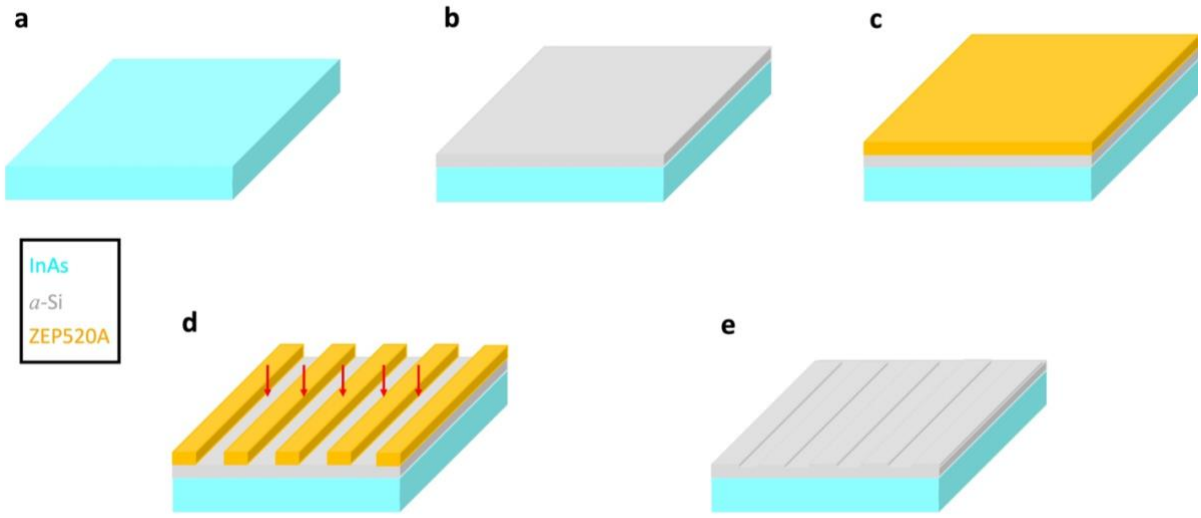

Figure 3.3: Fabrication process of sample. (a) We begin with a bare InAs wafer for which we have already determined the temperature-dependent optical properties. **(b)** a 2-μm-thick α-Si layer is deposited on top of the InAs wafer via PECVD. **(c)** A 750-nm-thick layer of resist, ZEP520A, is spun onto the wafer and the grating pattern is written into the resist via electron beam pattern generation (EBPG). (**d**) The pattern is then developed, and remaining resist is baked. The resist left on the sample surface acts as a mask for the ICP-RIE process. (**e**) The resist mask is removed overnight and the α-Si GMR structure is cleaned and imaged with an optical microscope and SEM.

The fabrication process of the GMR structure is outlined in Figure 3.3. We start by cleaning the *n*-InAs wafer in a sonicated acetone bath, followed by a sonicated isopropyl alcohol bath. Following the cleaning process, we deposit 2.05 μm of α-Si using plasma-enhanced chemical vapor deposition (PECVD) at 200 °C with a gas flow rate of 250 SCCM (5% SiH_4 / 95% Argon balance).

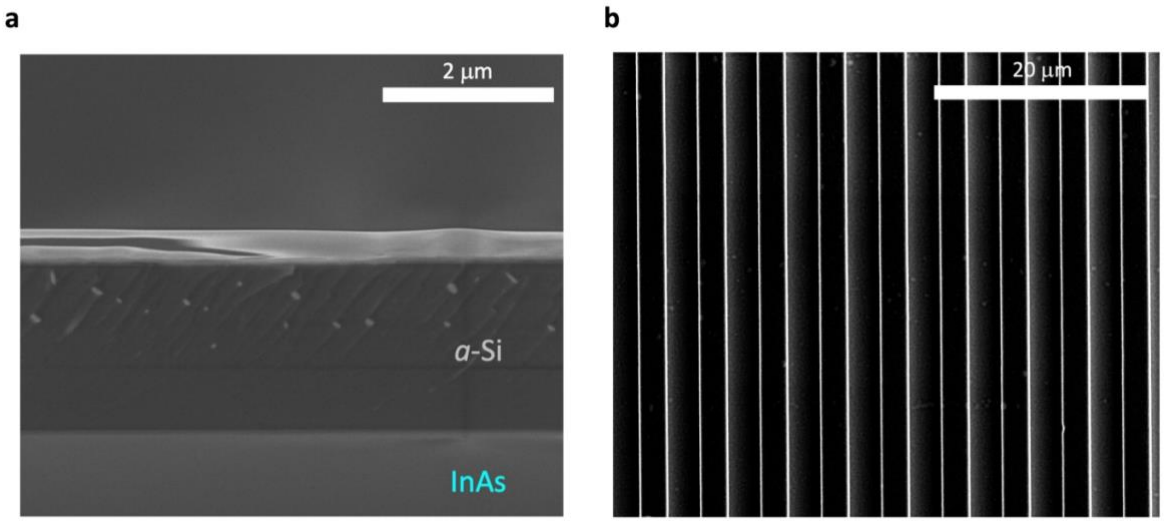

Figure 3.4: SEM images of α-Si layer and grating structure (a) Side-view SEM image of the 2-µm-thick α-Si layer on top of the InAs wafer. This sample was not used for the final grating structure, but rather for the optical characterization of the α-Si layer. **(b)** Top-view SEM of the fabricated grating structure.

Once the pattern is confirmed using an optical microscope, we leave the sample in Remover PG overnight and rinse the final sample in IPA and DI water. We take scanning electron microscope (SEM) images of the final grating (Figure 3.4 b) as well as the thickness of α-Si deposited on the InAs (Figure 3.4 a) to fine-tune the deposition and etching process.

3.3 Direct absorptivity and emissivity measurements at 0 magnetic field bias

We plot the polarization-resolved emissivity and absorptivity measurements above room temperature next to each other in Figure 3.5 a and b. The full angular dispersion from emissivity measurements are shown in Figure 3.2; constraints in the absorptivity measurement setup did not allow for small angles of incidence ($\theta <$ 35°). The spectral directional emissivity, $e_{sample}(\lambda, \theta, \chi, T)$, was found by subtracting out background signal and normalizing by a carbon blackbody reference emission at the same temperature, $I_{Carbon\ BB}(\lambda, \theta, \chi, T)$:

$$e_{sample}(\lambda, \theta, \chi, T) = \frac{I_{sample}(\lambda, \theta, \chi, T) - I_{Aluminum}(\lambda, \theta, \chi, 24° \text{ C})}{I_{Carbon\ BB}(\lambda, \theta, \chi, T) - I_{Aluminum}(\lambda, \theta, \chi, 24° \text{ C})} \qquad \text{(Eq. 3.2)}$$

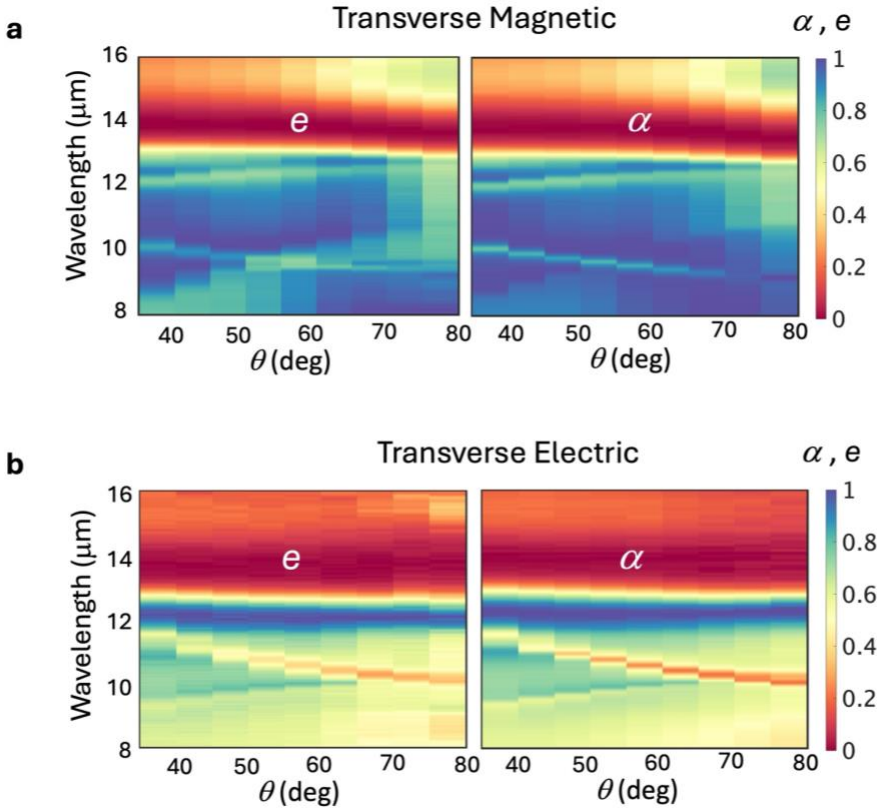

Figure 3.5: Comparison of collected spectral emissivity and absorptivity for the two measurement systems. (a and b) TM- and TE- polarized emissivity and absorptivity measurements taken at 100 °C (upper and lower respectively) showing the guided-mode dispersions.

The background emission intensity from the measurement apparatus was determined by measuring the emission intensity from an aluminum sample at ambient temperature, $I_{Aluminum}(24° \text{ C})$ (Figure 3.6) [12].

Since this is a measurement in the absence of magnetic field, the absorptivity and emissivity spectra are very similar to each other (Figure 3.5 a and b). The optical interference between a continuous InAs emission and spectrally-sharp resonance of the guided-mode structure result in a Fano-like emissivity and absorptivity spectrum. This is clear in Figure 3.5 a, where the $+1^{st}$ and -1^{st} order guided modes are visible as lower (lighter) emissivity and absorptivity lines starting at $\lambda = 12$ μm and $\lambda = 10$ μm for $\theta = 35°$, respectively. The resonances supported by the GMR structure have a finite bandwidth due to intrinsic loss in the system [13, 14].

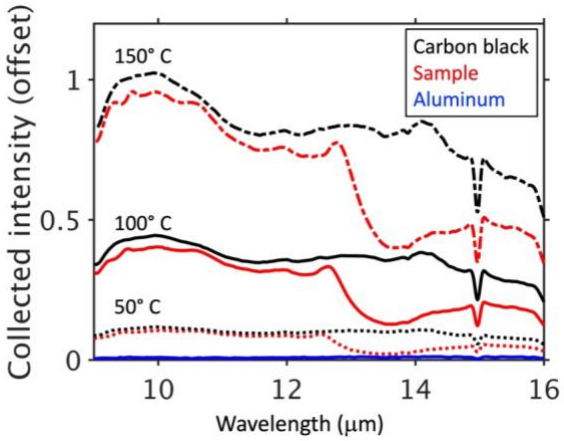

Figure 3.6: Normalization of the emissivity data for $\theta = 65°$. Raw traces of the collected emission from a Carbon black reference (black) and the sample (red) at three different temperatures. The blue trace is the emission of Aluminum at 24 °C and represents the background emission contributions from the system. Traces taken at different temperatures are offset for clarity.

The low emissivity and absorptivity band for $\lambda > 13$ μm for both TM- and TE-polarized light (Figure 3.5) is due to the low absorption/emission from the *n*-InAs at wavelengths longer than the plasma wavelength. We refer to this transition from high to low emissivity of the *n*-InAs across all angles as the InAs emissivity edge.

We use two different systems to measure the emissivity and absorptivity directly. The emissivity measurement system is a home-built, angle-resolved, thermal emission spectroscopy (ARTES) setup [15]. The sample is mounted at the rotation axis of a goniometer (Thorlabs BGM12CC) with an angular range of +/- 45°. The goniometer itself is on a 45° wedge so that we collect over an emission angular range of 0 - 90°. The rotation axis is positioned between the faces of the pole pieces of a low-field electromagnet (GMW 5403). The field strength across the gap between the pole pieces is measured using a Hall sensor (Lakeshore HGT-1010) and is found to be uniform across the sample. The field strength can be tuned by changing the current through the electromagnet coils or changing the pole gap. For our experiments, we keep the pole gap constant at 15 mm.

Both the areas of the carbon blackbody and the sample are the same (7 mm x 7 mm). We collect the emission from the sample with a ZnSe lens and pass the light into a Fourier-transform infrared (FTIR) spectrometer. We align both sample surfaces to the focus of the ZnSe lens (spot size ~100 μm) using the internal alignment laser of the FTIR. For polarization-resolved

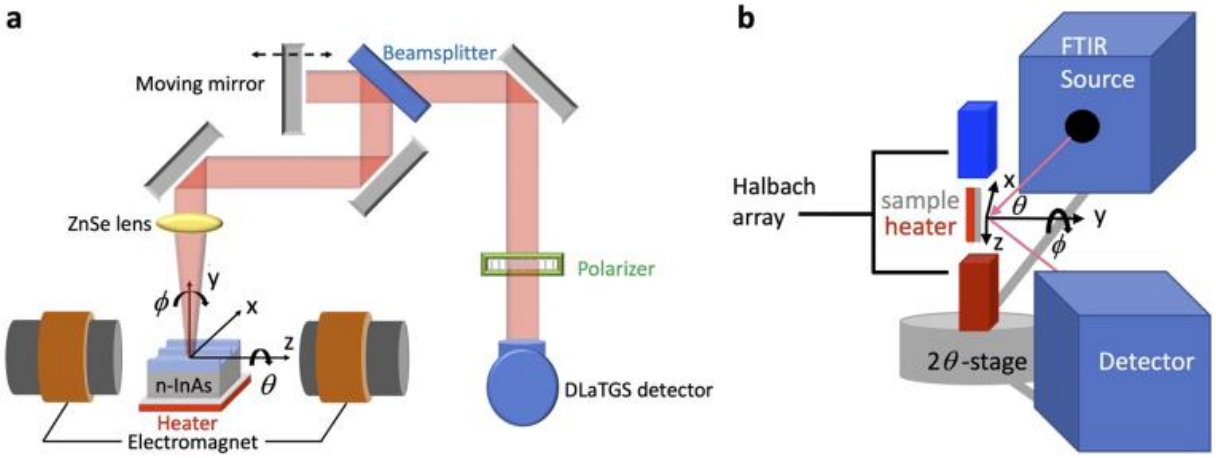

Figure 3.7: Schematics of the emissivity and absorptivity measurement setups. (a) For emissivity measurements, the sample is mounted on a heater at the rotation axis of a goniometer, centered between the pole pieces of an electromagnet. The goniometer allows us to rotate the sample around the z-axis and probe the outgoing radiation at an angle θ. The sample emission is collected through a ZnSe lens and sent through an external port into an FTIR. We place a polarizer in front of the detector to resolve the TM and TE emission. (**b**) The absorptivity measurement system uses an FTIR source and detector mounted on a 2-θ rotation stage. Instead of an electromagnet, we use a Halbach array of permanent magnets to apply the magnetic field. The sample is still heated to the same temperatures as in the emissivity measurements so that we have a direct comparison of the absorptivity and emissivity as defined by the Kirchhoff's Law.

measurements, we place a wire grid polarizer in front of a Deuterated Lanthanum TriGlycine Sulfate (DLaTGS) detector (Figure 3.7 a).

To enhance the signal-to-noise ratio, we heat the sample with a small-form resistive heater above room temperature (50° C, 100° C, and 150° C). A temperature-stable polyimide tape is used to fix the sample to the resistive heater. We subtract out the room-temperature signal by repeating the same measurements of Aluminum at room temperature. The intensity of the sample signal is then normalized by a carbon blackbody prepared by spraying a solution of carbon black onto carbon paper (Sigracet 38 BC) (Figure 3.6). Carbon black samples were also made by coating a silicon wafer with carbon black, however the non-uniformity of the carbon black distribution made it less desirable for normalization purposes.

The absorptivity measurements were done using a J.A. Woollam IR ellipsometer in reflection-transmission mode. The absorptivity measurements were all normalized against a gold reference sample with the same area as the device to account for the shape of the IR-spot changing as a function of angle. Because the source and detector are housed in large compartments, we were

limited to incidence angles above 35°. Instead of an electromagnet, we used a Halbach array [16] to apply the transverse magnetic field in the absorptivity setup. The field strengths could be tuned by changing the pole gap (Figure 3.7 b).

Of the two measurement systems, the spectral bandwidth of the emissivity measurement setup limits the full spectral range available. This is because the polarizer and ZnSe lens have non-uniform transmission outside of the 7-16 μm range. To keep the data analysis consistent across both measurements, we worked with normalized data from 8 to 16 μm for both the absorptivity and the emissivity measurements. This yields consistent matching of the spectra across the two measurement setups for the zero magnetic field case.

3.4 Kirchhoff thermal radiation violation and Onsager reciprocity relations for emissivity and absorptivity

By turning on a transverse, reciprocity-breaking magnetic field, we demonstrate a direct violation of Kirchhoff's law (Figure 3.8). In Figure 3.8 a and b we compare the change in emissivity and absorptivity for two opposite-valued magnetic fields, -1 T and +1 T. We observe that the change in absorptivity $\Delta\alpha = \alpha_{-1.0\,\mathrm{T}} - \alpha_{1.0\,\mathrm{T}}$ is opposite in sign to the observed change in emissivity $\Delta e = e_{-1.0\,\mathrm{T}} - e_{1.0\,\mathrm{T}}$. Note that $\Delta e \cong -\Delta\alpha$ over the full spectral and angular range. Figure 3.8 a and b also highlight the two spectral features at play: the InAs emissivity/absorptivity edge (red line starting at $\lambda \cong 13$ μm and $\theta = 35°$) and the +1st order GMR from the α-Si structure (faint red line starting at $\lambda \cong 12$ μm and $\theta = 35°$). The two features intersect near $\theta = 65°$, resulting in resonance tuning with magnetic field. Tuning of the peak emissivity spectral position, however, onsets at smaller, critical angle ($\theta_C = 50°$). This is a consequence of the InAs emission edge pulling the +1st order GMR emissivity peak even when both are not fully spectrally overlapped. This is discussed in depth later in the chapter in reference to Figure 3.9 c and Figure 3.12.

To achieve a more quantitative view of the magnetic-field tuning when Kirchhoff Law is broken, we display the emissivity and absorptivity at a specific angle $\theta = 70°$ (Figure 3.8 c and d). For both emissivity and absorptivity, we observe that the GMR coupled to the InAs is strongly affected by the transverse magnetic field. From a theoretical viewpoint, in the absence of other diffraction channels, this magnetic tuning having an opposite effect on the absorptivity and emissivity at a given angle derives from the Onsager-Casimir relations [17] for an absorber in an external magnetic field, B:

$$\alpha(\lambda,-\theta,B) = \alpha(\lambda,\theta,-B) \quad , \quad e(\lambda,-\theta,B) = e(\lambda,\theta,-B) \qquad \text{(Eq. 3.3)}$$

In words, swapping the positions of the source and detector ($\theta \rightarrow -\theta$) has the same effect as changing the sign of the reciprocity-breaking external field ($B \rightarrow -B$). To test this relationship, we rotate the sample stage to measure the sample emission for $-\theta$ and $+\theta$ and $-B$ and $+B$. (Our

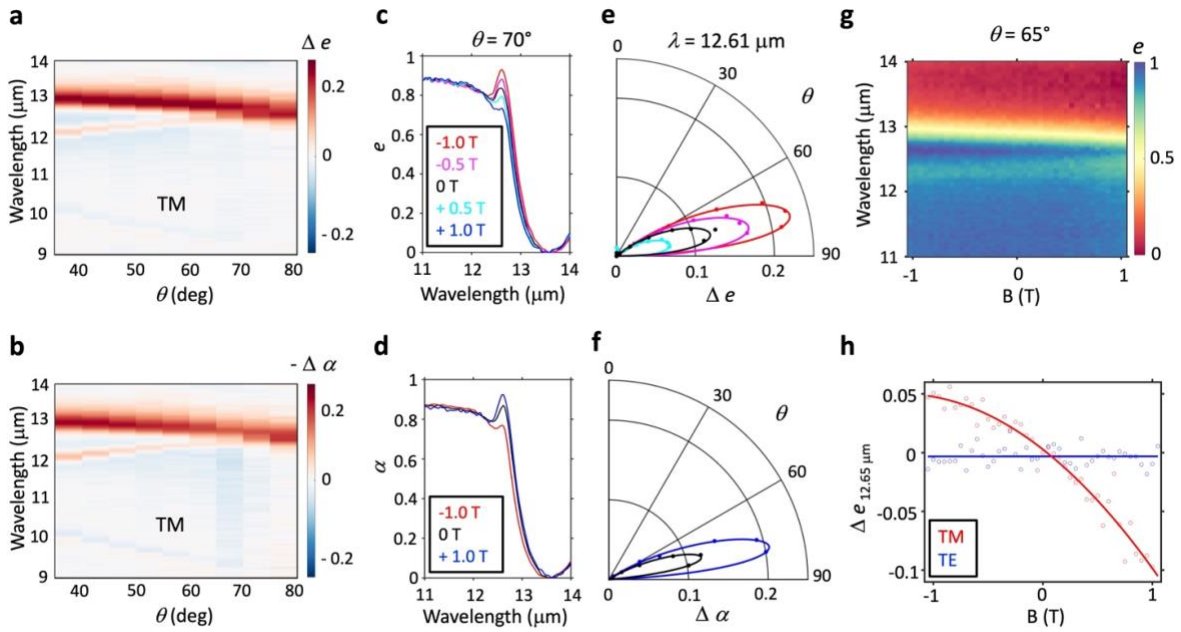

Figure 3.8: Violation of Kirchhoff's law in absorptivity and emissivity measurements. (**a** and **b**) Change in the absolute emissivity and absorptivity as the applied magnetic field is switched from +1.0 T to -1.0 T: $\Delta e = e_{-1.0\,\mathrm{T}} - e_{1.0\,\mathrm{T}}$ and $\Delta\alpha = \alpha_{-1.0\,\mathrm{T}} - \alpha_{1.0\,\mathrm{T}}$. The magnetic field has an opposite effect for the absorptivity and emissivity. Note that we plot Δe in **a** and $-\Delta\alpha$ in **b**. (**c** and **d**) Spectral emissivity and absorptivity at θ = 70° for varying magnetic fields. (**e** and **f**) Directivity plots demonstrating the effect of the magnetic field on the resonant directional emissivity and absorptivity coupling through the GMR structure. We subtract out the least resonant magnetic field case for both emissivity and absorptivity: $\Delta e = e - e_{1.0\,\mathrm{T}}$ and $\Delta\alpha = \alpha - \alpha_{-1.0\,\mathrm{T}}$. While the directionality is imposed by the GMR structure and is unchanged by the magnetic field, the outcoupling intensity is modulated by the InAs. Equal and opposite tuning is observed for emissivity and absorptivity. (**g**) Measured emissivity as a function of wavelength and magnetic field for θ = 65°. The emissivity resonance can be seen as a dark blue region near λ = 12.7 μm for large negative magnetic fields. The resonant emission is tuned to narrower linewidth and smaller amplitude with increasing magnetic field. This is a consequence of the InAs emission edge (yellow line starting at λ = 13 μm for -1 T) shifting to shorter wavelengths for increasing magnetic field. (**h**) Change in the emissivity near the resonance wavelength (λ = 12.65 μm) for θ = 65° as a function of magnetic field. TE-polarized emission shows no magnetic field dependence while the TM-emissivity change is fit quadratically. This captures the beginning of the saturation effect for large negative magnetic fields.

experimental setup does not allow measurements of absorptivity around normal incidence.) With zero magnetic field, the emission of the photonic structure is symmetric across $\theta = 0°$: $e(\lambda, \theta) = e(\lambda, -\theta)$ (Figure 3.9 a). For nonzero magnetic field, we display the change in emissivity, $\Delta e = e_{-1.0\,\mathrm{T}} - e_{1.0\,\mathrm{T}}$, and observe equal and opposite effects of the magnetic field across $\theta = 0°$ (Figure 3.9 b).

Equation 3.3 has been further developed in the context of a nonreciprocal absorber/emitter with a transverse magnetic field [16, 17]. Because our structure exhibits a compound symmetry that combines a mirror operator with an operator that flips the sign of the magnetic field, the spectral directional absorptivity and emissivity are related by [17]:

$$\alpha(\lambda, -\theta, B) = e(\lambda, \theta, B) \qquad \text{(Eq. 3.4)}$$

Taking the right-hand-sides of equations 3.3 and 3.4, we note that $\alpha(\lambda, \theta, -B) = e(\lambda, \theta, B)$. The opposite *B*-field dependence for emissivity and absorptivity is apparent from our measurements (Figures 3.8 a - f, 3.9 d and e). To illustrate this, in Figures 3.8 e and f, we show directivity profiles at the resonant wavelength by subtracting the largest positive magnetic field emissivity spectrum at each angle (largest negative magnetic field spectrum at each angle for absorptivity), from the spectra for the other applied magnetic fields. We observe that the directionality of emissivity and absorptivity at the resonant wavelength does not change by varying magnetic field. While the magnitude of the emissivity and absorptivity are modulated, the angular profile remains unchanged. This can be understood from the fact that the directionality of the thermal emission is imposed by the grating structure which does not have a dependence on the magnetic field.

We also vary the magnetic field at a single angle ($\theta = 65°$) in a fine sweep and measure the emissivity from the structure (Figure 3.8 g). At large negative magnetic field, the resonant emission is both large in amplitude and broad in linewidth (dark blue region from 12.5 – 12.8 μm). As the magnetic field is increased to positive values, the InAs emission edge (yellow line starting at 13 μm for -1 T) blueshifts and reduces both the amplitude and the linewidth of the resonant emission. A detailed discussion of the InAs emission edge shifting and the resonant emission amplitude decreasing with the increasing magnetic field can be found later in the chapter (Figure 3.10).

Figure 3.8 h shows the magnetic-field-dependent change in the emissivity at λ = 12.65 μm (near the resonant wavelength) relative to the zero-field case for both TM- and TE-polarized thermal emission. For the TE-polarized emission, as expected, we observe no modulation of emissivity. For TM-polarized light, the change in emissivity for positive magnetic field is approximately linear (~ 0.1 / T). This approximately linear magnetic field dependence of the

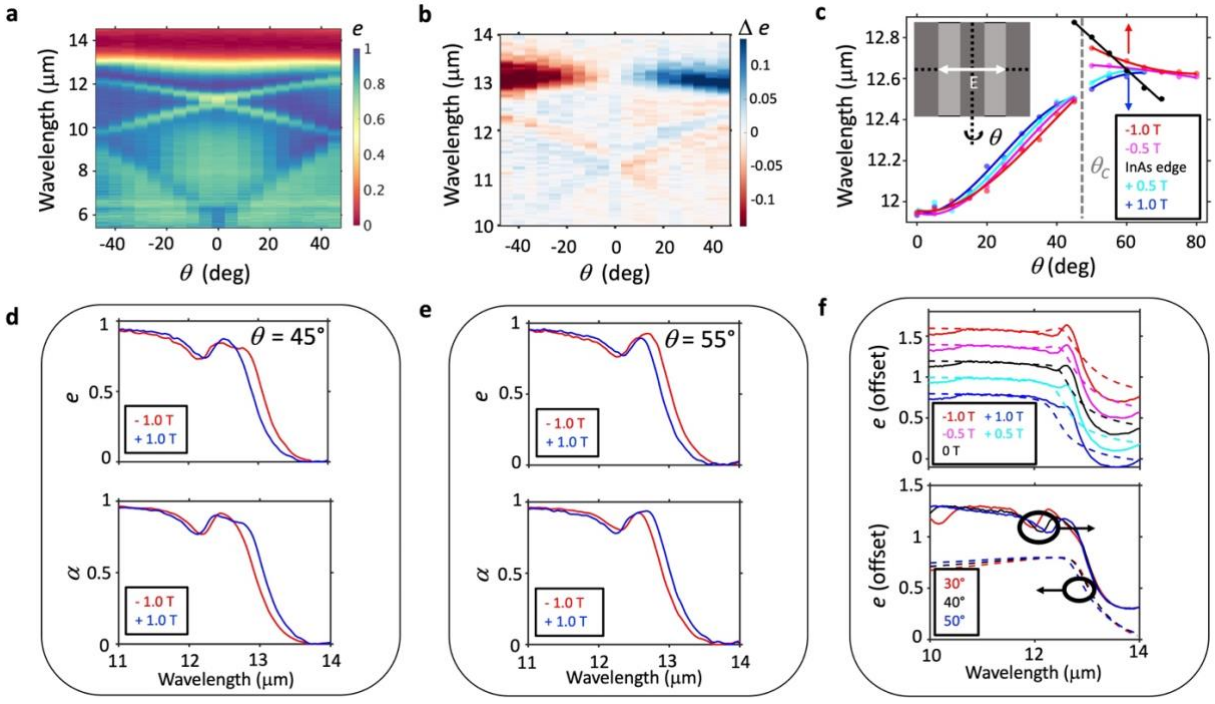

Figure 3.9 Onsager-Casimir relations for emissivity and absorptivity in a magnetic field. (**a**) TM emissivity measurements for zero applied magnetic field when the outgoing angle is near normal incidence. (**b**) Change in emissivity from -1.0 to +1.0 T across normal incidence. The antisymmetric (across $\theta = 0°$) shifts in intensity associated with the guided-mode peaks are visible as light blue and red features from 10 to 12 μm. (**c**) TM emissivity maxima for varying magnetic fields. (**d** and **e**) Emissivity and absorptivity spectra above and below $\theta_C = 50°$. For $\theta = 45°$, the spectral shift of the peak emissivity does not align with the InAs shift; however, for $\theta = 50°$, the peak shift aligns with the magnetic field shift of the InAs. Opposite magnetic field effects are observed for absorptivity and emissivity. (**f**) (Upper panel) Emissivity measurements of the photonic structure (solid) and simulations of the InAs emissivity (dashed) for $\theta = 70°$ for varying magnetic field. The blue shift in the InAs emission edge for positive field results in smaller emissivity. Conversely, a red shift in the InAs emission edge for negative fields results in larger emissivity. (Lower panel) Emissivity measurements of the photonic structure (solid) and simulations of the InAs emissivity (dashed) illustrating the opposite spectral shift of the GMR and InAs emission edge as a function of θ for zero applied magnetic field.

emissivity and absorptivity for positive fields is expected from the cyclotron resonance of the InAs [18].

However, over the full magnetic field range shown in Figure 3.8 h (-1 to +1 T) we fit the change in emissivity to a quadratic function. At large negative magnetic fields, the emissivity modulation decreases. This is because the emissivity upper and lower bounds of the photonic structure are dominated by the emissivity of the *n*-InAs. The saturation of the emissivity tuning for increased emissivity (negative magnetic field) is a consequence of the fact that the spectral radiance cannot exceed that of the emitted blackbody spectrum (i.e. cannot become super-Planckian) [19]. This is confirmed both in a further analysis of the experimental data (Figure 3.10) and in simulation (Figure 3.11).

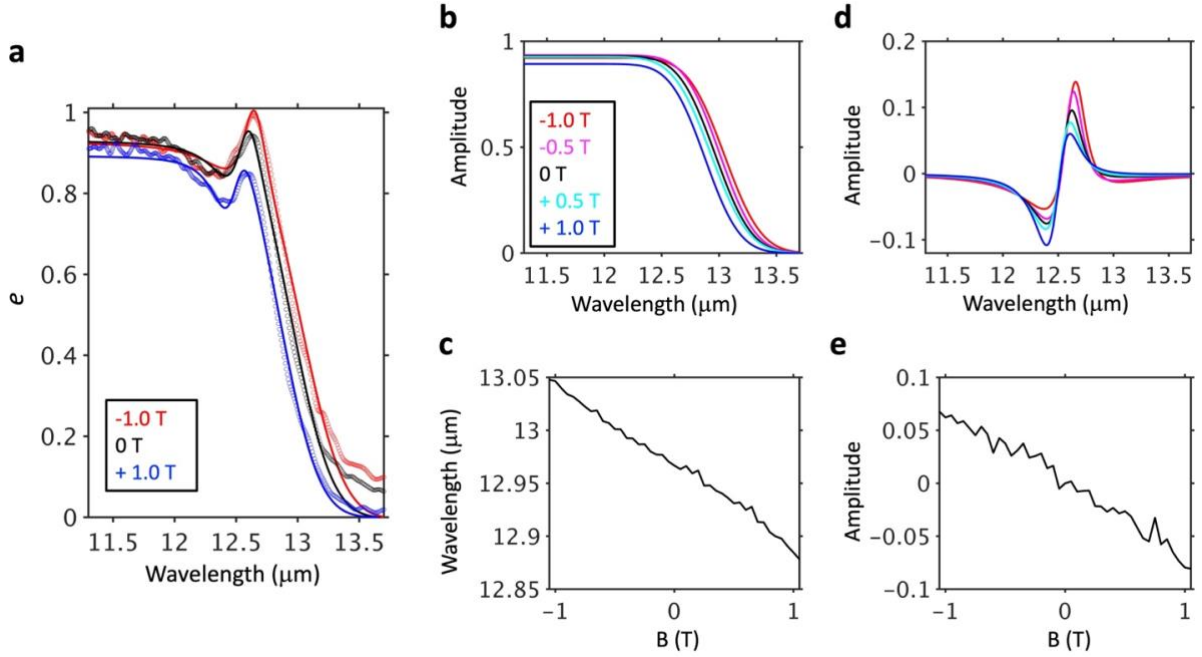

Figure 3.10: Fitting results from the fine magnetic field sweep at $\theta = 65°$. (**a**) Experimental data and fits for three different magnetic fields. (**b**) The extracted InAs contribution to the emissivity (amplitude) for varying magnetic field, modeled as a sigmoid. (**c**) Central wavelength of the InAs contribution (i.e. the sigmoid) for varying magnetic field. We observe a blueshift of the emission edge with increasing magnetic field. (**d**) The resonant emissivity contribution (amplitude) of the GMR structure is modified, but the spectral shift is dictated by the InAs magnetic field response (**b** and **c**). (**e**) Change in the resonant amplitude for all magnetic field values.

For a deeper analysis of the experimental measurements, we fit the fine magnetic field sweep data taken at $\theta = 65°$, shown in Figure 3.8 g. We break the contributions to the photonic structure emissivity into two components: a sigmoid, representing the InAs emission edge, and a Fano-like resonance that results from the GMR aligned to the InAs emission edge (Figure 3.10 a). When these two components are combined, the wavelength shift in the emission is due to a blueshift of the InAs emission edge for positive magnetic field and redshift for negative magnetic field (Figure 3.10 b). This spectral shift of the InAs emission edge is linear as a function of magnetic field (Figure 3.10 c). The Fano-like resonance produces a small change in the central wavelength for varying magnetic field (Figure 3.10 d), and its most significant magnetic-field response is the reduction in the resonant amplitude (Figure 3.10 e).

An interesting point to note is that the emissivity tuning of the photonic structure saturates for sufficiently large magnetic field at a given wavelength (Figure 3.8 h). This linear behavior in the sigmoid central wavelength shift is reflected when looking at the average change in the photonic structure emissivity over a wavelength range that spans the emission edge. However, for a single wavelength that corresponds to the maximum emissivity of the structure under negative magnetic field (λ = 12.65 μm, red trace in Figure 3.10 a), the emissivity tuning saturates because of the constraint of Planckian emission (i.e. the sample emissivity cannot exceed 1). This effect is only discernible when the emissivity approaches 1. We re-plot Figure 3.8 h from earlier in the chapter next to simulations for the same angle ($\theta = 65°$) and at the simulation resonant wavelength under negative magnetic field (λ = 12.65 μm) (Figure 3.11). At lower emissivity, the magnetic tuning of the emissivity will appear linear.

By mapping the emissivity maxima for the $+1^{st}$ order guided mode over the full angular range, we can visualize the wavelength and amplitude tuning of both the emissivity and absorptivity with magnetic field, as illustrated in Fig. 3.9 c. The magnetic-field-induced shifts in

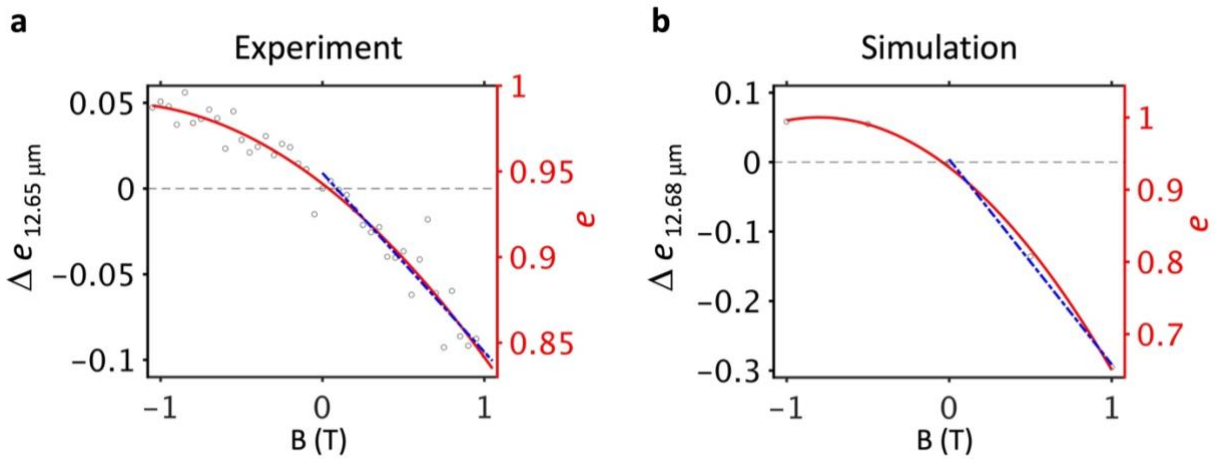

Figure 3.11: Experimental and simulated emissivity change for non-zero magnetic field exhibiting saturation effect as resonant sample emissivity approaches Blackbody limit. (**a**) Experimental data (black points) with quadratic fit (solid red) for the full magnetic field range and linear fit (dot-dash blue) for the positive magnetic field range. (**b**) The same plot as in (**a**) for our simulated photonic structure. The magnitude of the change in emissivity as a function of magnetic field is larger, however we observe the same saturation behavior. Note that our resonant peak emissivity at $\theta = 65°$ is at a slightly longer wavelength (λ = 12.68 μm).

the emissivity and absorptivity resonance amplitude and, to a lesser extent, the resonant wavelength shifts, are due to the shift in the InAs emissivity edge.

We observe a large modulation of the resonant emissivity *amplitude* for large angles (Figure 3.8 c, Figure 3.12 c). In this range, ($\theta > 65°$), the emissivity of the device is non-resonant for the positive field cases and no maxima larger than the InAs background are found (Figure 3.12 c), represented by the absence of blue markers for the emissivity maxima in Figure 3.9 c. For $e(\lambda, 70°, +1.0\ \mathrm{T})$, or $\alpha(\lambda, 70°, -1.0\ \mathrm{T})$, the emission wavelength of the InAs blue shifts (Figure 3.9 f, upper panel, dashed blue trace) and no longer strongly outcouples through the GMR structure (Figure 3.9 f, upper panel, solid blue trace). For $e(\lambda, 70°, -1.0\ \mathrm{T})$, the magnetic field shifts the emission wavelength of the InAs to longer values compared to the zero-field case, resulting in a stronger resonance and outcoupling through the GMR structure and into the far-field (Figure 3.9 f, upper panel, red trace).

Tuning of the emissivity and absorptivity resonance *wavelength* is strongest near a critical incidence angle ($\theta_C \cong 50°$ in Figure 3.9 c). As seen in the lower panel of Figure 3.9 f, for increasing θ the +1st order guided mode redshifts (solid traces) and the InAs emission wavelength blueshifts

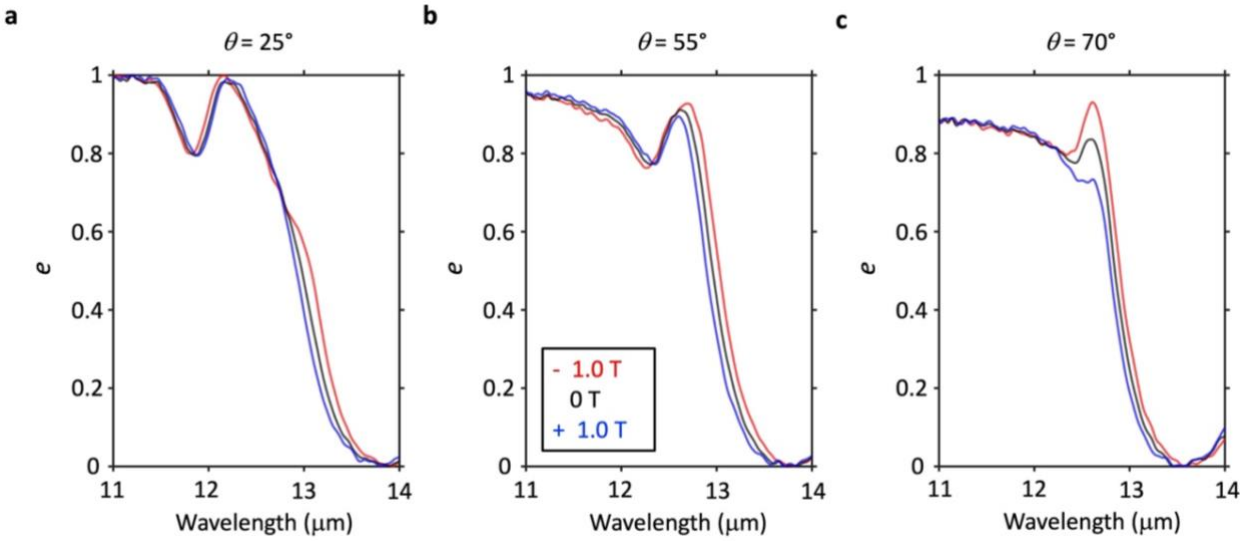

Figure 3.12: Experimental data comparing different regimes of the spectral and amplitude tuning of the peak emissivity for three angles. (**a**) Emissivity for $\theta = 25°$ for three magnetic field values. At small angles, the spectral overlap of the InAs emissivity edge (~13 μm) and the +1st order GMR (~12.1 μm) is minimal, resulting in no tuning of the spectral position or magnitude of the emissivity peak of the overall structure. (**b**) At $\theta = 55°$, the spectral position of the emissivity peak is tuned by the direction of the InAs emissivity edge shift (blueshift for +1.0 T and redshift for -1.0 T) relative to the +1st order GMR. We term this angular range where the InAs emissivity edge begins to change the spectral position of the emissivity peak as the "critical angle" θ_C. (c) For large angles, we get strong emissivity amplitude tuning with little shift in the spectral position of the resonant emissivity.

(dashed traces). Near $\theta_C = 50°$, the InAs emission wavelength and +1st order GMR begin to spectrally overlap. For sufficiently large negative fields, the InAs emissivity has its own peak known as the Brewster mode [20] (Figure 3.9 f, upper panel, red trace), which, when sufficiently spectrally overlapped with the GMR, pulls the overall peak emissivity to longer wavelengths as shown in Figure 3.9 e and Figure 3.12 b. Below θ_C, the spectral overlap between the InAs emission wavelength and +1st order GMR is mismatched enough that the wavelength of the emissivity peak is dominated by the GMR, seen in Figure 3.9 d and Figure 3.12 a. The same is true for absorptivity; however the role of the magnetic field is reversed as seen in Figures 3.9 d and e.

Beyond the fine sweep of the magnetic field at $\theta = 65°$, we can also understand the mechanisms of the emissivity and absorptivity tuning by looking at the emissivity spectra for three different characteristic angular ranges:

I. Completely uncoupled, where the magneto-optic shift in the InAs emission edge is spectrally mismatched from the $+1^{st}$ order GMR ($0° < \theta < 45°$). This is shown in Figure 3.12 a for $\theta = 25°$. The spectral position of the peak emissivity is not discernibly affected by the magneto-optic shift of the InAs.

II. "Mode pulling," where the InAs emission edge and $+1^{st}$ order GMR are slightly spectrally mismatched, resulting in the peak emissivity switching between the GMR and the Brewster mode depending on the magnetic field sign ($\theta = 50°, 55°$). This is shown in Figure 3.12 b for $\theta = 55°$. The spectral position of the peak emissivity is "pulled" blue (for positive) and red (for negative magnetic field) by the magneto-optic shift of the InAs.

III. Completely coupled, where the InAs emission edge is completely spectrally overlapped with the $+1^{st}$ order GMR ($\theta > 60°$). This is shown in Figure 3.12 c for $\theta = 70°$. The spectral position of the peak emissivity does not move, however the magneto-optic shift of the InAs tunes the emissivity to being above (negative field) and below (positive field) the emissivity background.

In summary, we measured the emissivity and absorptivity of a magneto-optic photonic structure, giving direct experimental evidence for violation of the Kirchhoff law of thermal radiation under a modest transverse magnetic field. We find that the dependence of the absorptivity and emissivity detuning for small applied magnetic fields is linearly dependent on the magnetic field, however it saturates when the peak emissivity approaches 1. Both the spectral and directional tuning of the emissivity and absorptivity are described by the Onsager-Casimir relations. These results open the path for future experimental work on Kirchhoff-violating thermal emitters. Thanks to the ubiquity of devices and applications for both nonreciprocal and thermal emission, numerous theoretical works have proposed combining these two concepts to address phenomena related to radiative cooling [21], solar energy harvesting [22], and spin-polarized light sources [16]. Our work demonstrates the decoupling of the absorptivity and emissivity for such devices and opens the door to more complex designs that realize distinct emissivity and absorptivity channels [23].

The nonreciprocal mechanism in this chapter, a strong gyrotropic effect around the ENZ wavelength of *n*-InAs, can be extended to implement the Kirchhoff violation over a broadband spectral range [24], which we demonstrate in the following chapter. Alternative materials [25] can also be used to reduce, or even remove [26] the requirement of an external magnetic field. Beyond materials with an inherent nonreciprocal optical response, methods of implementing nonreciprocal devices using spatiotemporal modulation [27] or external, unidirectional biasing [28] are avenues towards other Kirchhoff-violating emitters.

References

[1] L. Zhu, S. Fan, Near-complete violation of detailed balance in thermal radiation. *Phys. Rev. B* **90**, 1-3 (2014).

[2] B. Zhao, C. Guo, C. A. Garcia, P. Narang, S. Fan, Axion-Field-Enabled Nonreciprocal Thermal Radiation in Weyl Semimetals. *Nano Letters* **20**, 1923-1927 (2020).

[3] S. Pajovic, Y. Tsurimaki, X. Qian, G. Chen, Intrinsic nonreciprocal reflection and violation of Kirchhoff's law of thermal radiation in planar type-I magnetic Weyl semimetal surfaces. *Phys. Rev. B* 102, 165417 (2020).

[4] S. S. Wang, R. Magnusson, J. S. Bagby, M. G. Moharam, Guided-mode resonances in planar dielectric-layer diffraction gratings. *J. Opt. Soc. Am.* **7**, 1470-1474 (1990).

[5] D. Fattal, J. Li, Z. Peng, M. Fiorentino, R. G. Beausoleil, Flat dielectric grating reflectors with focusing abilites. *Nature Photonics* **4**, 466-470 (2010).

[6] A. Kamboj, L. Nordin, P. Petluru, A. J. Muhowski, D. N. Woolf, D. Wasserman, All-epitaxial guided-mode resonance mid-wave infrared detectors. *Appl. Phys. Lett.* **118**, 201102 (2021).

[7] T. Khaleque, R. Magnusson, Light management through guided-mode resonances in thin-film silicon solar cells. *Journal of Nanophotonics* **8**, 083995 (2014).

[8] P. P. Paskov, Refractive indices of InSb, InAs, GaSb, $InAs_xSb_{1-x}$, and $In_{1-x}Ga_xSb$: Effects of free carriers. *J. Appl. Phys.* **91**, 1890 (1997).

[9] J. N. Heyman et al., Terahertz emission from GaAs and InAs in a magnetic field. *Phys. Rev. B* **64**, 085202 (2001).

[10] H. Reddy, U. Guler, A. Kudyshev, A. V. Kildishev, V. M. Shalaev, A. Boltasseva, Temperature-Dependent Optical Properties of Plasmonic Titanium Nitride Thin Films. *ACS Photonics* **4**, 1413-1420 (2017).

[11] J. Bergmann, M. Heusinger, G. Andrä, F. Falk, Temperature dependent optical properties of amorphous silicon for diode laser crystallization. *Optics Express* **20**, A856-A863 (2012).

[12] R. W. Boyd, *Radiometry and the detection of optical radiation* (Wiley, New York, 1983).

[13] P. Lalanne, et al., Quasinormal mode solvers for resonators with dispersive materials. *Journal of the Optical Society of America A* **36**, 686-704 (2019).

[14] J. Li, Z. Li, S. Shen, Degenerate quasi-normal mode theory for near-field radiation between plasmonic structures. *Optics Express* **28**, 34123-34136 (2020).

[15] F. Zhong, K. Ding, Y. Zhang, S. Zhu, C. T. Chan, H. Liu, Angle-Resolved Thermal Emission Spectroscopy Characterization of Non-Hermitian Metacrystals. *Phys. Rev. Applied* **13**, 014071 (2020).

[16] C. Adambukulam, V. K. Sewani, S. Asaad, M. T. Madzik, H. G. Stemp, A. Morello, A. Laucht, An ultra-stable 1.5 tesla permanent magnet assembly for qubit experiments at cryogenic temperatures. *Rev. Sci. Instrum.* **92**, 085106 (2021).

[17] H.B.G. Casimir, On Onsager's Principle of Microscopic Reversibility. *Rev. Mod. Phys.* **17**, 350 (1945).

[18] B. Zhao, Y. Shi, J. Wang, Z. Zhao, N. Zhao, S. Fan, Near-complete violation of Kirchhoff's law of thermal radiation with a 0.3 T magnetic field. *Optics Letters* **44**, 4204 (2019).
[19] Y. Xiao, M. Sheldon, M. A. Khats, Super-Planckian emission cannot really be 'thermal'. *Nature Photonics* **16**, 397-401 (2022).
[20] T. Taliercio, V. N. Guilengui, L. Cerutti, E. Tournié, J.-J. Greffet, Brewster "mode" in highly doped semiconductor layers: an all-optical technique to monitor doping concentration. *Optics Express* **22**, 24294-24303 (2014).
[21] S. Fan, W. Li, Photonics and thermodynamics concepts in radiative cooling. *Nature Photonics* **12**, 182-190 (2022).
[22] Y. Park, B. Zhao, S. Fan, Reaching the Ultimate Efficiency of Solar Energy Harvesting with a Nonreciprocal Multijunction Solar Cell. *Nano Letters* **22**, 448-452 (2022).
[23] B. Zhao, J. Wang, Z. Zhao, C. Guo, Z. Yu, S. Fan, Nonreciprocal Thermal Emitters Using Metasurfaces with Multiple Diffraction Channels. *Phys. Rev. Applied* **16**, 064001 (2021).
[24] J. S. Hwang, J. Xu, A. Raman, arXiv:2212.13112v1 **[physics.optics]**.
[25] Z. Zhang, L. Zhu, Broadband Nonreciprocal Thermal Radiation. *Phys. Rev. Applied* **19**, 014013 (2023).
[26] E. Liu et al., Giant anomalous Hall effect in a ferromagnetic Kagome-lattice semimetal. *Nature Physics* **14**, 1125-1131 (2018).
[27] Y. Hadad, J. C. Soric, A. Alù, Breaking temporal symmetries for emission and absorption. *PNAS* **113**, 3471-3475 (2016).
[28] S. A. H. Gangaraj, F. Monticone, Drifting Electrons: Nonreciprocal Plasmonics and Thermal Photonics. *ACS Photonics* **9**, 806-819 (2022).

Chapter 4

Broadband Kirchhoff thermal radiation law violation

4.1 Motivation and introduction for broadband, directive nonreciprocity

Thus far, inequalities in the spectral directional emissivity and absorptivity presented in this thesis have been limited to narrow spectral resonances [1], or wavelengths well beyond the infrared regime [2]. Bridging the gap from basic demonstrations to practical applications requires control over a broadband spectral range of the unequal spectral directional absorptivity and emissivity.

The nonreciprocal effect presented in the previous chapters relied on tuning the coupling of a guided-mode resonance with a plasma resonance, limiting the bandwidth and angular range of the absorptivity and emissivity detuning. In this chapter, we demonstrate broadband nonreciprocal thermal emissivity and absorptivity by measuring the thermal emissivity and absorptivity of gradient ENZ InAs layers of subwavelength thicknesses (50 nm and 150 nm) with an external magnetic field. We carry out these direct measurements of both the absorptivity and the emissivity for two samples with different thicknesses and find that the nonreciprocal emission and absorption strongly depends on the sample's subwavelength thickness and the carrier concentration ordering.

4.2 Broadband directive thermal emitters

Broadband directive thermal emission was first demonstrated through coupling multiple sub-wavelength ENZ materials to a leaky, propagating mode, known as the Berreman mode [3]. The dispersion of the mode is dependent on the total thickness of the layered stack, D, while the spectral range is determined by the various ENZ resonances of the constituent layers, termed a

---

This chapter is adapted from K. J. Shayegan, J. S. Hwang, B. Zhao, A. P. Raman, H. A. Atwater, Broadband nonreciprocal thermal emissivity and absorptivity. *Light Sci. & Appl.* **13**, 176-181 (2024).

gradient ENZ. The term gradient in used in this context when the concentration varies linearly along the depth dimension. This concept is depicted in the upper panels of Figure 4.1, while the emissivity for varying stack thickness is plotted in the lower panels.

The experimental realization of broadband directional emission was first done using oxides with material resonances in the infrared. Thin films of these oxides were then stacked together on a reflective substrate, with the total thickness of the stack determining the angular range of the outcoupled Berreman mode [4].

Thin-films of gradient ENZ materials lend themselves readily to magneto-optically active III-V semiconductors (e.g. GaAs, InAs). Molecular beam epitaxy (MBE) of III-V semiconductor materials can precisely control both the carrier concentration of thin films to as well as the thickness to the atomic limit. Furthermore, because the ENZ wavelengths determine both the broadband spectral range of emission as well as the wavelength where nonreciprocal behavior is largest, such structures are ideal for broadband, directive nonreciprocal emission.

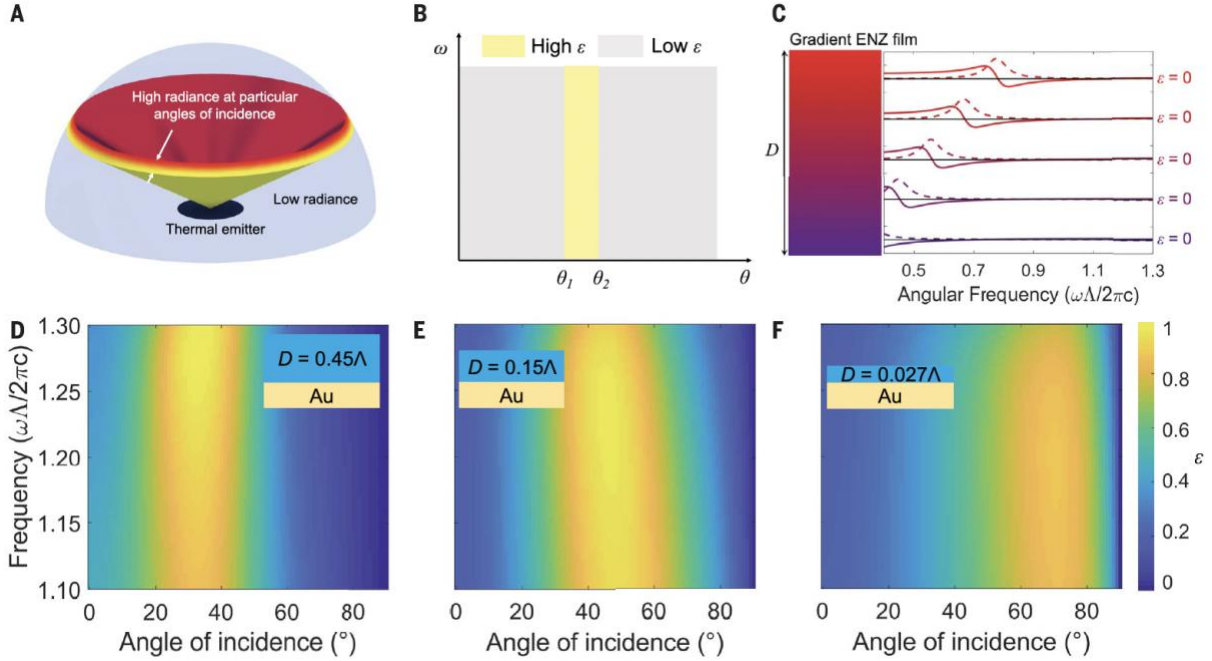

Figure 4.1 Concept of broadband, directive thermal emission, (a - b) where the emitted radiation is directed through a narrow angular range between θ_1 and θ_2. Outside of this angular range, the emission is suppressed. **(c)** Permittivity of each individual ENZ layer along the depth dimension, D. **(d - f)** Emission frequency vs angle of incidence for three varying structure thicknesses. The scaling factor, Λ, is the central wavelength of emission for the broadband spectral range. Figure reproduced from [4].

4.3 Fabrication of broadband, directive emitter for Kirchhoff violation

The ENZ resonance wavelengths are set by the electron free carrier concentration of each individual InAs layer. We focus on results obtained from a gradient-ENZ structure with six carrier concentrations (n_1 – n_6) increasing from 1.5 to 4.5 x 10^{18} cm^{-3} from the bottom to the top of the structure [5]. The individual resonances of the layers are spectrally closely spaced to create a broadband emissivity and absorptivity feature in the 12.5 μm – 17 μm region. The angle at which the emitted light couples out of the structure is determined by the thicknesses of the constituent ENZ layers. This is formally known as the Berreman mode, as outlined in the previous section.

The mechanisms that determine the emitter spectral and directional selectivity (i.e., the carrier concentration and thickness of the constituent layers, respectively) also determine the bandwidth, directionality, and magnitude of the nonreciprocal tuning of the emissivity and absorptivity. Consequently, the contrast between low emissivity angles at near-normal incidence and high emissivity at large angles in addition to low emissivity outside versus high emissivity inside the ENZ bandwidth is tunable with the magnetic field. The dielectric function of each layer follows the same Drude model outlined in Chapters 2 and 3. The free carrier density n_i, effective mass $m_{e,i}$ and scattering rate Γ_i used in the simulations of the broadband structure are included in Table 4.1.

Table 4.1. Material properties in simulations

Layer	*carrier concentration* (10^{18} cm^{-3})	m_e ($9.11x10^{-31}kg$)	Γ (THz)
n_1	4.5	0.053	5.653
n_2	3.9	0.050	5.652
n_3	3.3	0.046	5.651
n_4	2.7	0.042	5.650
n_5	2.1	0.038	5.649
n_6	1.5	0.032	5.649
$n_{reflector}$	60	0.158	10.06
n_{GaAs}	$2.1x10^{-12}$	0.063	3.2824

The thickness of each layer with distinct carrier concentration is 150 nm thick and is capped at the back with a 300 nm degenerately doped n^{++} InAs layer that acts as a back reflector (Figure

4.2 (a) in section 4.4). We also measure a structure with 50 nm thick individual layers, which is discussed later in this chapter.

MBE is used to grow the designed InAs-nanolayers with different n-type (Si) doping concentrations. The solid-source VEECO Gen-930 MBE is equipped with a valve-controlled arsenic cracker to provide the As_2 flux and a 400 cc SUMO cell for indium is operated with a higher tip temperature to reduce the defect density caused by indium spitting. The InAs-nanolayers are grown on epi-ready, single-side polished, semi-insulating GaAs (100) substrates. An oxide desorption process is carried out for the GaAs (100) substrates prior to the InAs-nanolayer growth under an As_2 flux of 5×10^{-6} Torr at a substrate temperature of 600 °C. A 50 nm GaAs buffer layer is grown at a GaAs growth rate of 0.33 mLs^{-1}, in which the substrate temperature decreases to 580 ºC. After the buffer layer growth, the GaAs substrate is maintained at 600 °C for 10 minutes under an As_2 flux to smoothen the surface. For the growth of InAs nano-layers, the substrate temperature is decreased to 410 ºC, the InAs growth rate is fixed at 0.5 mLs^{-1} and the As/In flux ratio is controlled to be 1.2 ~ 1.5. Following the growth of the gradient InAs film, the same As_2 flux on the surface is maintained until the substrate cools to 325 °C. Finally, the As_2 flux is stopped and the sample is taken out of the MBE growth chamber at ~ 275 ºC. Reflection high energy electron diffraction (RHEED) is utilized to calibrate the GaAs and InAs deposition rates, as well as to calibrate the As/In flux ratio.

4.4 Measurement of directive, broadband Kirchhoff violation

We obtain the spectral directional emissivity and absorptivity of the sample using the same measurement systems from the previous chapter (Figure 4.2 (b-d)). The absorptivity data is taken with a J.A. Woollam IR ellipsometer while the emissivity data is taken using a homebuilt angle-resolved thermal emission spectroscopy setup [6]. Comparing the absorptivity and emissivity spectra to simulations at the expected angle for maximum magnetic-field tuning ($\theta = 60°$), we resolve the resonances that collectively form the broadband absorptivity and emissivity spanning 12.5 μm – 17 μm (Figure 4.2 (b)). The background slope from high to low emissivity and absorptivity from short (10 μm) to long (19 μm) wavelengths is attributed to absorption of the GaAs handle on which the sample is grown.

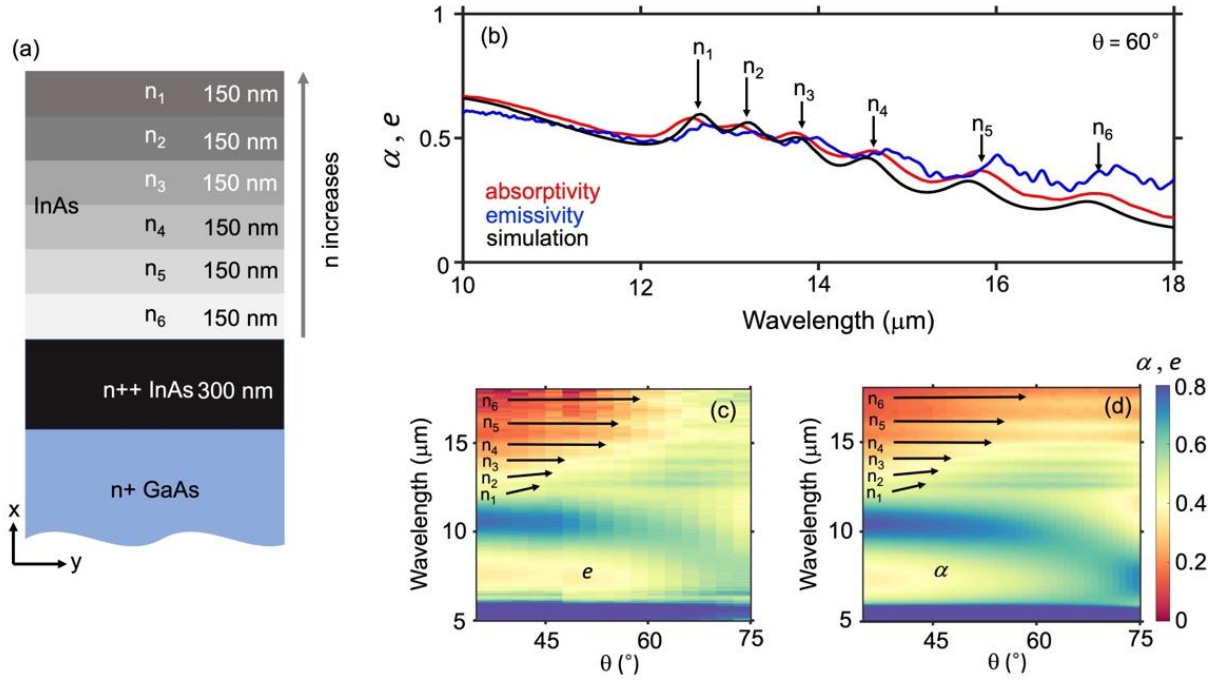

Figure 4.2 Magneto-optic gradient-ENZ structure. (a) Schematic of the gradient-ENZ structure. The carrier concentration increases for layers closer to the surface of the device (i.e., in the increasing x-direction). A very degenerately doped n^{++} InAs layer is used as a back reflector. The back reflector layer thickness is to scale. **(b)** Absorptivity (red), emissivity (blue), and simulated (black) spectra for the structure at $\theta = 60°$. The resonant absorption/emission associated with each layer are labeled. **(c)** Spectral directional emissivity data taken with the sample heated to 100 °C. **(d)** Spectral directional absorptivity data taken at ambient (25 °C).

The absorptivity measurements are taken at room temperature (25 °C) while the emissivity measurements are taken with the sample heated to 100 °C. Heating the sample to higher temperatures results in a larger signal-to-noise ratio for emissivity measurements, however results in a slight redshift of the resonances associated with the ENZ-crossings (Figure 4.2 b, blue trace). Comparing the full spectral and angular information acquired from emissivity and absorptivity measurements, we see that the qualitative agreement between the two measurements matches across a large angular range ($35° < \theta < 75°$) (Figure 4.2 (c-d)). There are benefits to the two measurement systems: the emissivity setup can access the near-normal angular range of the sample

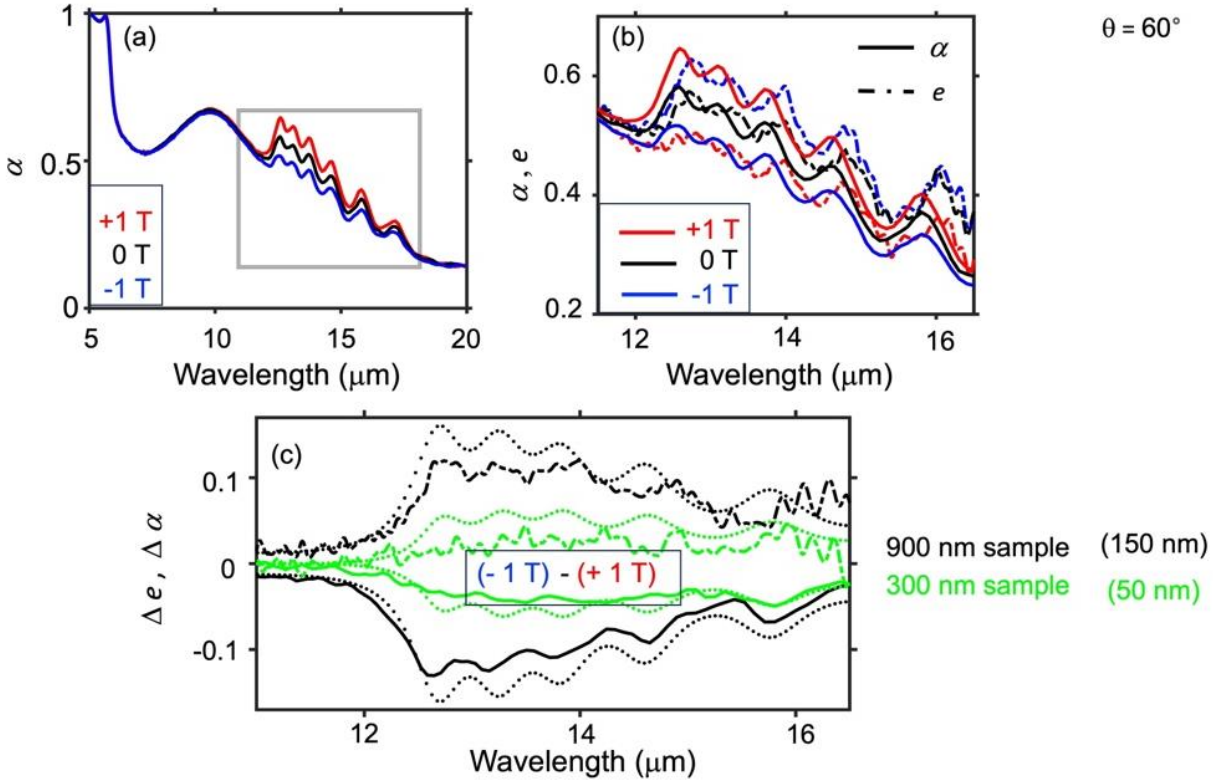

Figure 4.3 Broadband Kirchhoff violation. (a) Absorptivity data taken at $\theta = 60°$ for varying magnetic field values. The resonant peak near 6 μm is the n^{++} back reflector. The light gray box highlights the broadband spectral range where the tuning is observed. (**b**) Absorptivity and emissivity plots zoomed in to the spectral range of interest. The opposite magnetic field dependence is observed in the emissivity data. We note that the emissivity data is noisier at longer wavelengths where detector sensitivity is reduced. (**c**) Simulated (dotted) and measured Δe (dot-dashed) and Δa (solid) spectra for $\theta = 60°$ when subtracting the + 1 T measurement from the – 1 T measurement. The thick sample (black) shows a stronger and spectrally inhomogeneous tuning when compared to the thin sample (green).

emission while the absorptivity setup has greater accuracy and precision in the individual angle certainty owing to it not being a homebuilt setup or requiring a lens for collection. There is increased signal uncertainty at longer wavelengths (> 16 μm) in the emissivity measurement

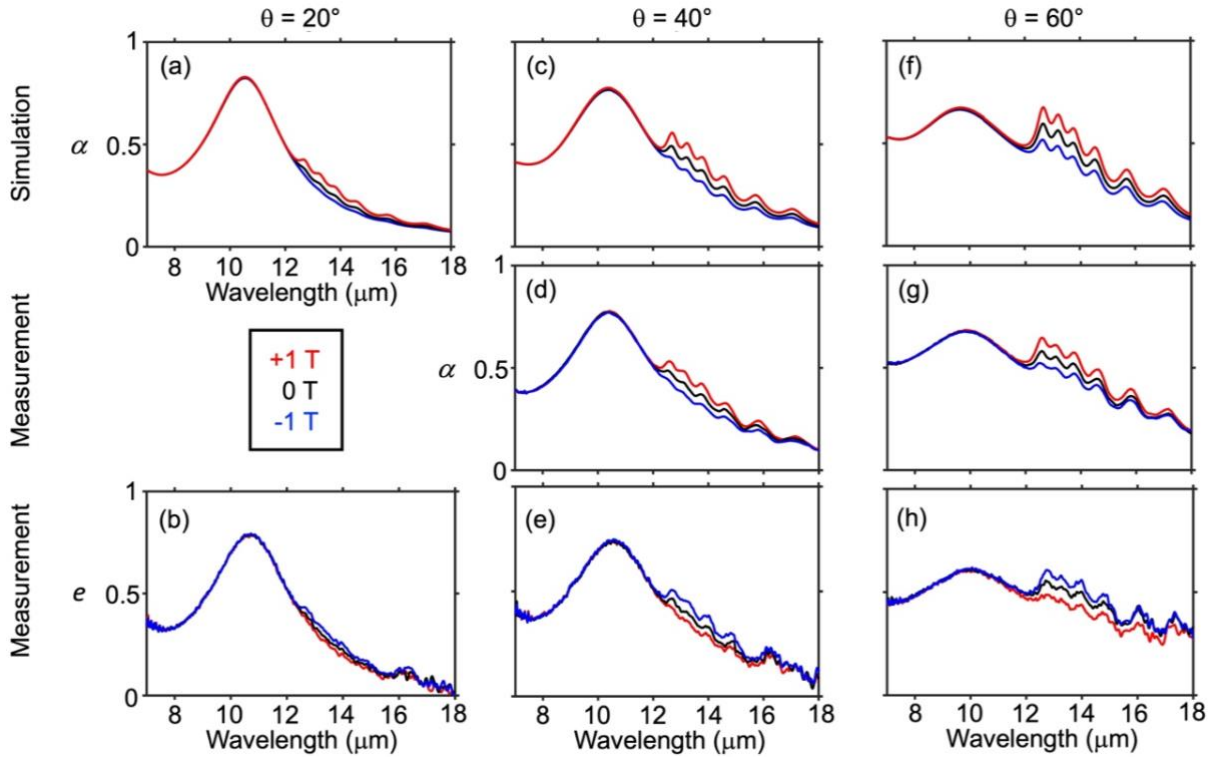

Figure 4.4 Simulated absorptivity, measured absorptivity, and measured emissivity spectra under an external magnetic field for $\theta = 20°$ (a and b), $\theta = 40°$ (c – e), and $\theta = 60°$ (f – h). The absorptivity data is taken at 25 °C and the emissivity data is taken at 100 °C. We note that for wavelengths above 16 μm, the emissivity data increases in noise due to decreased detector sensitivity and transmissivity of the ZnSe lens.

setup due to both the polarizer transmission function and the detector sensitivity at these wavelengths. A more in-depth description of the emissivity and absorptivity measurements is included in Chapter 3.

The intensity of the resonances corresponding to $n_1 – n_6$ have a strong angular dependence, however the spectral position of the resonance is constant as a function of angle, indicative of a distinctive broadband leaky Berreman mode supported by gradient-ENZ materials [7, 8]. This simplifies our analysis of the magnetic-field effect on the emissivity and absorptivity tuning in that

we can average over a fixed broadband spectral range and look at the angular dependence of the tuning without losing the spectral range where the effect is occurring.

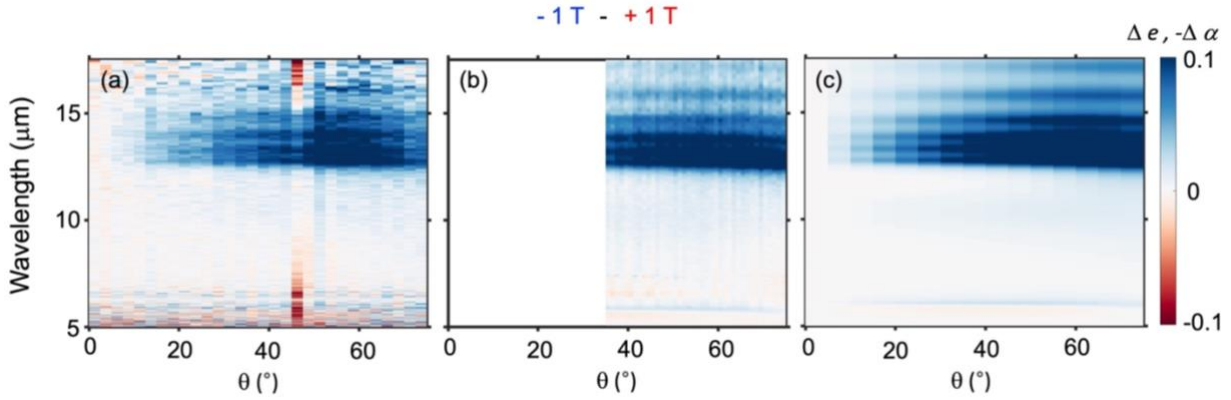

Figure 4.5 Spectral directional change in the emissivity (a) and absorptivity (b) between -1 T to + 1 T. We plot the negative change in the absorptivity to keep the colors of the plots consistent. In simulation (**c**) we also observe a faint strip near 6 μm that corresponds to the n^{++} InAs back reflector of the structure. This is also visible in (**b**), however the noise at short wavelengths in the emissivity measurement obscures this detail.

The measured absorptivity spectra at $\theta = 60°$ for an applied field of – 1 T, 0 T, and + 1 T are shown in Figure 4.3 (a). We observe tuning across the entire wavelength range (12.5 μm – 17 μm), with stronger tuning at shorter wavelengths. This nonuniformity in the spectral tuning is a consequence of the ordering of the layers. As discussed later in the chapter (Figures 4.9 and 4.11) the ordering and thicknesses of the layers constituting the gradient-ENZ sample can be judiciously chosen to achieve uniform spectral tuning.

We compare the magnetic field dependence of the absorptivity to the emissivity of the sample under the same applied magnetic field strengths (Figure 4.3 (b), Figure 4.4). The opposite magnetic field dependence of the emissivity of the sample demonstrates nonreciprocal broadband absorptivity and emissivity and implies a violation of the spectral-directional Kirchhoff thermal radiation law [3]. We note that the emissivity spectral features are slightly red-shifted from the heating of the sample, and that the strong match between the zero-field (Figure 4.3 (b), black traces) absorptivity and emissivity data degrades slightly at long wavelengths. This is a consequence of detector sensitivity at long wavelengths ($\lambda > 16$ μm) decreasing in the emissivity setup. Despite the low emission collected from the sample at these wavelengths, the detected

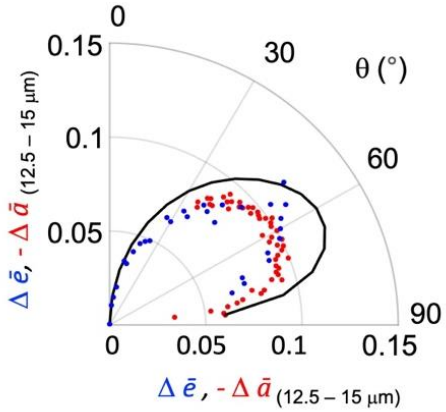

Figure 4.6 Polar plot of the average change in the emissivity and absorptivity between – 1 T to + 1 T for a spectral bandwidth of 12.5 μm – 15 μm. The experimentally measured absorptivity and emissivity are plotted as scatter points (red and blue, respectively) and the simulation results are plotted as a solid black line. The average tuning is largest around θ = 60° for the absorptivity measurements and simulated change in emissivity, in line with the direction of peak emissivity for zero applied magnetic field. While in theory the absolute change in emissivity and absorptivity for the same field should overlap, the emissivity setup has a larger angular uncertainty. Note that we plot the negative change in absorptivity to keep all plots on the same axis.

emission from the reference blackbody is also low, resulting in a normalization that is increasingly noise sensitive.

We also measure the difference in the emissivity and absorptivity ($\Delta\, e$, $\Delta\, a$) between - 1 T to + 1 T for a second sample with the same gradient carrier concentration profile but with individual layer thicknesses of 50 nm (Figure 4.3 (c)). The $\Delta\, e$ and $\Delta\, a$ for this second, thinner sample is notably smaller than what is observed for the thicker sample and is confirmed through simulations. This arises from the fact that applying a magnetic field changes both the real and imaginary parts of the permittivity tensor, in turn changing optical loss behavior directly in the InAs layer. This can also be understood as the effect of a larger total number of carriers (electrons) responding to the magnetic field and thereby imparting the gyrotropic effect to TM radiation. A more in-depth analysis of the thickness dependence and ordering of the carrier concentration is provided later in the chapter (Figures 4.11 and 4.12).

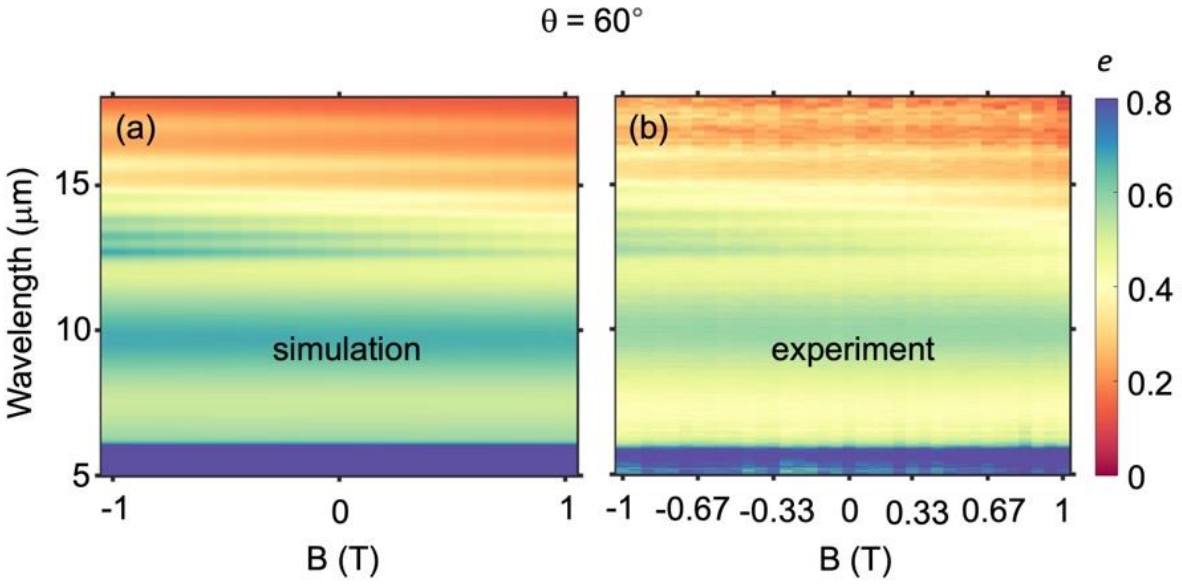

Figure 4.7 Simulation (a) and experimental data (b) showing the emissivity spectra as a function of the applied magnetic field for θ = 60°. We observe stronger tuning of the shorter wavelength modes, corresponding to the layers located nearer the surface of the structure.

The constant spectral position of the broadband Berreman mode across all angles allows us to compare the average change in the absorptivity and emissivity across all measured angles for a fixed spectral range without losing information to angular dispersion of resonances (Figure 4.5). Figure 4.6 plots the average change in the emissivity and absorptivity over a constant spectral

bandwidth of 12.5 μm – 15 μm when the magnetic field is changed between – 1 T and + 1 T ($\Delta \bar{e}_{(12.5-15\ \mu m)}$ and $\Delta \bar{a}_{(12.5-15\ \mu m)}$). The scatter points are the experimentally measured change in the emissivity (blue) and absorptivity (red) with the simulated change plotted in solid black. Note that we plot the negative value of $\Delta \bar{a}_{(12.5-15\ \mu m)}$ to keep the sign of the axes the same for all traces.

Based on simulations, the maximum tuning of the emissivity and absorptivity occurs around $\theta = 60° - 65°$. This aligns with the angle at which the sample most strongly emits based on the individual layer thickness. Both $\Delta \bar{e}_{(12.5-15\ \mu m)}$ and $\Delta \bar{a}_{(12.5-15\ \mu m)}$ have approximately the same angular dependence as predicted by simulations. The slight angular divergence of $\Delta \bar{e}_{(12.5-15\ \mu m)}$ is attributed to larger angular uncertainty and noise between emissivity measurements when compared to the absorptivity data. In theory, the two should overlap exactly, as the increased emissivity and decreased absorptivity should be directly correlated.

Going to the angle where the largest Δe and Δa are observed as a function of field ($\theta = 60°$), we performed a fine variation of the magnetic field in both simulation and in our measurements of the emissivity (Figure 4.7). Starting at - 1 T, the individual emissivity peaks from 12.5 μm – 15 μm are visible as green ripples. The broadband Berreman modes of the deeper, lower carrier concentration layers appear as light yellow against the red background of the longer wavelength (λ > 15 μm) emissivity. As we go to zero and positive magnetic field values, the peak

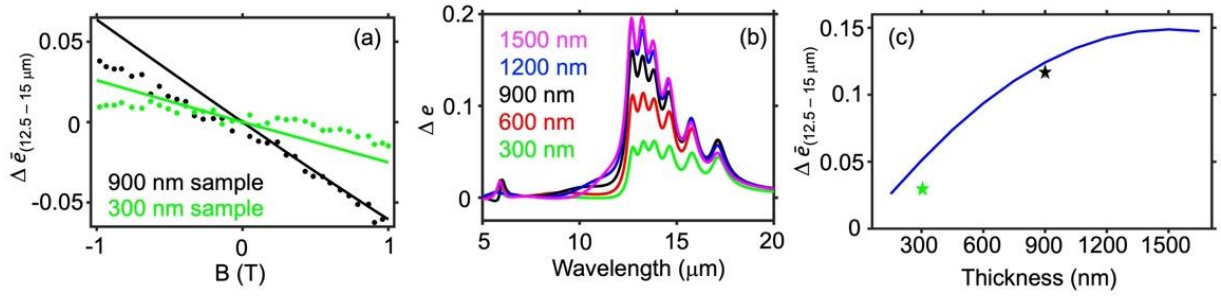

Figure 4.8 Thickness dependence of nonreciprocal effect. (**a**) Fine magnetic field dependence of the emissivity from 12.5 μm to 15 μm for a thick (black) and thin (green) sample. The thick sample shows a stronger magnetic field dependence than the thin one. (**b**) Simulated Δe spectra for varying sample thickness. We observe stronger tuning overall for thicker samples; however the tuning is increasingly skewed blue. Small tuning of the back reflector at 6 μm is also seen in the experimental measurements of the absorptivity (Fig. S3). (**c**) The average change in the emissivity from 12.5 μm to 15 μm for changing sample thickness. The green and black stars are the experimentally measured values. The angle in this is held at $\theta = 60°$, and it should be noted that changing the thicknesses of the constituent ENZ layers will also influence the directionality.

emissivity in the 12.5 μm – 15 μm range is strongly tuned from ~0.6 (green) to 0.45 (yellow). This spectral region is tuned stronger than longer wavelengths in large part due to the ordering of the layers (Figure 4.10). While it appears that there is no tuning of the emissivity at wavelengths below 12.5 μm, we can resolve a slight tuning of the n^{++} InAs back reflector near 6 μm in the absorptivity measurements and in simulation (Figure 4.5). This spectral shift is not resolvable in the direct emissivity measurements due to noise added by atmospheric absorption in this wavelength range.

Staying at $\theta = 60°$, we compare the change in the emissivity under external magnetic field for both the thick (150 nm individual layer thickness, 900 nm total thickness) sample and a second, thin (50 nm individual layer thickness, 300 nm total thickness) sample. The tuning of the magnetic field is smaller both in our measurement (scatter) and simulations (solid lines) for the thin sample (green) (Figure 4.8 (a)). While the angular distribution of the emissivity/absorptivity tends to larger angles for thinner samples, the overall decrease in the magnetic tuning of the absorptivity and emissivity for thinner samples holds true across other angles (Figure 4.9).

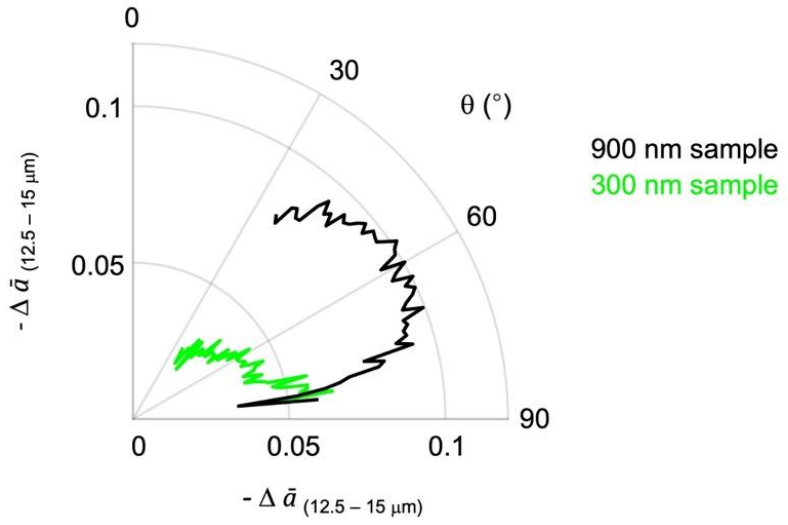

Figure 4.9 Polar plot for 300 nm and 900 nm change in absorptivity. Average change in the absorptivity between – 1 T to + 1 T for a thin (green) and thick (black) sample where the carrier concentration gradient is the same. The spectral range of the average is from 12.5 μm to 15 μm. The thin sample's peak absorptivity and emissivity are at larger angles due to the thickness dependence of the angular dispersion of the Berreman modes. We observe stronger tuning over a wide angular range for the thicker sample.

4.5 Thickness and ordering dependence of nonreciprocal contrast

To explore this thickness dependence in greater detail, we simulate the spectral change in the emissivity (absorptivity) from – 1 T to + 1 T at $\theta = 60°$ for samples with linearly varying thickness (Figure 4.8 (b)). The thickness of the individual layers is the same, and we use the total thickness when referring to each sample. Two things are discernible when we plot Δe between the two magnetic fields. Firstly, increasing thickness results in larger overall tuning of the emissivity (and absorptivity). Secondly, the spectral distribution of the tuning becomes skewed towards shorter wavelengths within the broadband window. This stronger tuning at shorter wavelengths is a direct result of the ordering of the layers. If one were to place the lowest carrier concentration layer (n_6) at the top of the structure and reverse the ordering so that the highest carrier concentration layer (n_1) is situated on the reflector, the tuning at longer wavelengths would exceed the tuning at shorter wavelengths (Figure 4.10 and Figure 4.12). One limitation of samples comprised of constituent layers with successively increasing thickness is that the directional selectivity of the Berreman mode decreases and the absorptivity and emissivity become more isotropic.

Figure 4.8 (c) plots the change in the average emissivity at θ = 60° between – 1 T and + 1 T for the spectral range from 12.5 μm to 15 μm for varying total thickness (and layer thickness) of the samples. We include the experimentally measured values as symbols on the plot. While the average tuning increases with increasing sample (and layer) thickness, the effect saturates above 1500 nm total thickness (250 nm individual layer thickness). For these thicker samples, the angle of optimal coupling for the Berreman mode shifts closer to normal incidence. This results in weaker Berreman mode coupling to free-space and could account for the saturation of the effect in the limit of large thicknesses.

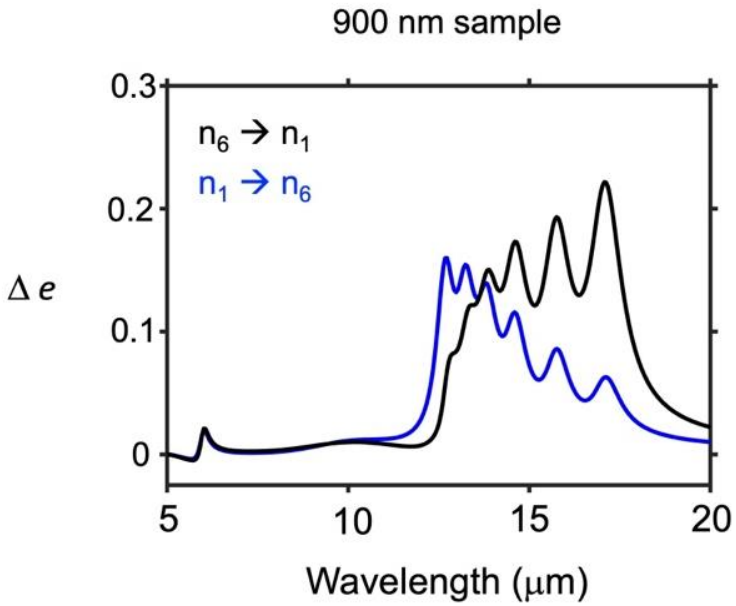

Figure 4.10 Simulated change in the spectral emissivity between – 1 T to + 1 T for the 900 nm sample at θ = 60° for two carrier concentration gradient orderings. The black trace is for increasing carrier concentration for deeper layers; the blue trace is for decreasing carrier concentration for deeper layers (the sample discussed and experimentally measured in the chapter). Reversing the carrier concentration order of the gradient layers results in a reversal in the spectral dependence of the tuning and an overall increase in the effect of the magnetic field on the emissivity and absorptivity.

For a configuration where the ENZ gradient goes to higher carrier concentrations (shorter ENZ wavelength) for deeper layers, we note a stronger overall tuning (Figure 4.10). This can be understood intuitively: as the free carrier concentration of a layer increases, it can be thought of as more metallic [9, 10]. In the case of our sample, having the high free carrier concentration layer on the top means that the emission from deeper layers is absorbed (or absorption of deeper layers is screened by the top layers, as $n_1 \rightarrow n_6$). If one were to reverse the ordering of the carrier

concentration gradient ($n_6 \rightarrow n_1$), one would see the opposite spectral dependence (Figure 4.10). Not only would the tuning at longer wavelengths be larger, but the overall tuning magnitude would be larger. Intuitively this can be interpreted as the lower carrier concentration layers behaving less "metallic" than the higher carrier concentration layers and thus do not screen the deeper layers as effectively.

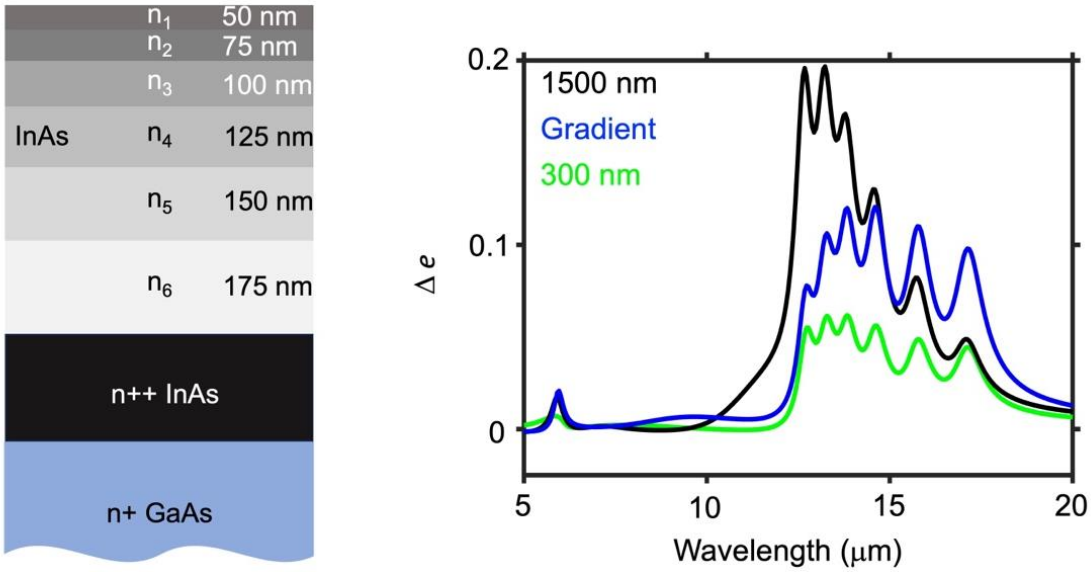

Figure 4.11 Structure with both a gradient in the carrier concentration as well as the thickness (left). The thinner layers on top result in weaker tuning of the wavelengths associated with those layers. However, this also means that the tuning of longer wavelength (deeper) layers is not screened as strongly. The simulated change in the spectral emissivity between – 1 T to + 1 T for $\theta = 60°$ show this tradeoff.

A way to balance the larger magnitude tuning afforded by thicker layers with the spectral uniformity of the tuning for thinner samples is to introduce a gradient in the thickness of the individual layers. We suggest that the thickness of the individual ENZ layers be increased as the layers go deeper into the sample (Figure 4.11, left panel). The thicker layers will have stronger tuning at their respective wavelengths due to the larger electronic contribution/thickness, while the thinner layers located near the top are not as heavily "screened" as thin layers deep in the heterostructure. The resultant tuning is both large in magnitude relative to the thin sample while spectrally more uniform than the thick sample (Figure 4.11, blue trace). It should be noted that the intensity of the tuning for the gradient thickness sample could be increased further by swapping the order of the carrier concentration gradient (i.e., going to higher carrier concentrations along the

depth dimension). While we plot the spectral tuning for $\theta = 60°$, a deeper analysis of the effect of having a gradient in the thickness layer needs to be done.

To confirm that the screening effect is in part due to the metallic nature of the upper layers, we run simulations for the difference in emissivity from +1 T to -1 T for varying carrier concentration of only the top layer (Figure 4.12). We observe that as the carrier concentration of the top layer increases (i.e. becomes more metallic), the tuning effect of the magnetic field is reduced for the deeper, lower carrier concentration layers.

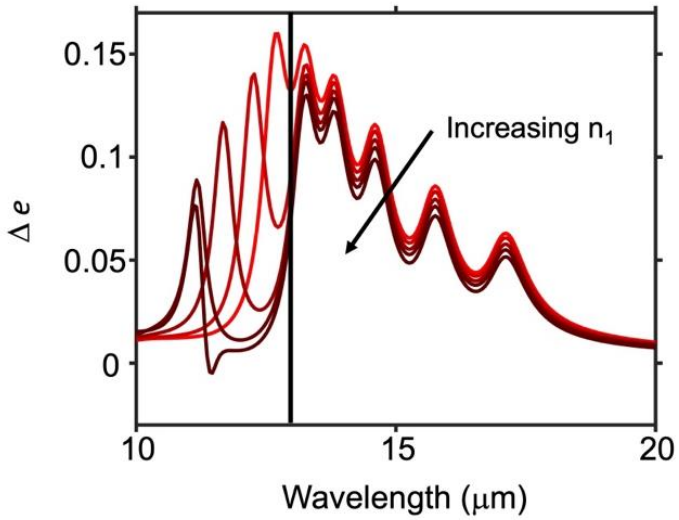

Figure 4.12 Average change in the emissivity from + 1 T to - 1 T for increasing top layer carrier concentration. As the concentration of the top layer increases (light red to dark red), the tuning of the lower layers is also reduced. The carrier concentrations for the top layer used in the above figure are tabulated in the figure below.

4.6 Summary and outlook

The spectral dependence of the tuning is related to the depth of the layer associated with the wavelength being tuned. In the devices we measured, this meant that shorter wavelengths were tuned more strongly than longer wavelengths due to layers with higher carrier concentrations being located nearer to the top of the sample. Furthermore, the magnitude of the tuning is dependent on sample thickness, with thicker layers resulting in a larger magnitude of tuning. This larger overall magnitude in tuning comes at the cost of uniformity in the spectral distribution of the tuning. To balance this, we put forward a gradient-ENZ structure where the individual layer thicknesses are also varied along the depth dimension as a potential solution.

The general design principles regarding thickness and ordering are applicable to other materials that should exhibit the nonreciprocal absorptivity and emissivity both with (e.g., InSb [11], graphene [12]) and without a magnetic field (Weyl semimetals [13, 14, 15]). A limitation in using 2D materials lies in the thickness requirement of a Berreman mode. Other designs that rely on drift effects [16, 17, 18], and spatiotemporal modulation [4, 19]) need to be developed further for broadband nonreciprocal absorptivity and emissivity demonstrations at practical wavelengths. The spectral bandwidth of the nonreciprocal emissivity and absorptivity for this configuration can be tuned by the free carrier concentration, albeit with a reduction in tuning magnitude at shorter wavelengths due to larger scattering rates for higher carrier concentrations. In a fundamental optical mode point of view, methods that allow the heavily doped InAs reflector to effectively push the fields into the gradient ENZ layer and minimize the optical power lost towards the bottom of the emitter would allow more photons to interact with the free carriers, hence enhancing the average contrast. This can be done by increasing the thickness of the heavily doped InAs layer or increasing the doping concentration of the heavily doped InAs layer and thereby having this layer feature a larger, negative real part of the permittivity. From a materials point of view, using a higher moblity, lower electron effective mass material like InSb should enhance the magnetic field response of the structure. Another avenue to increasing the contrast between the nonreciprocal emissivity and absorptivity is to introduce a lossless dielectric spacer layer between the gradient-ENZ layers and the back reflector [20]. By adding such a layer, the phase difference for the

absorptivity and emissivity when a magnetic field is applied can result in near-complete destructive or constructive interference.

References

[1] K. J. Shayegan, et al. Direct observation of the violation of Kirchhoff's law of thermal radiation. *Nature Photonics* **17**, 891-896 (2023).

[2] Y. Hadad, J. C. Soric, A. Alu, Breaking temporal symmetries for emission and absorption. *Proceedings of the National Academy of Sciences of the United States of America* **113**, 3471-3475 (2016).

[3] S. Vassant, J.-P. Hugonin, F. Marquier, J.-J. Greffet, Berreman mode and epsilon near zero mode. *Optics Express* **20**, 23971-23977 (2012).

[4] Xu, J., Mandal, J., & Raman, A. P. Broadband directional control of thermal emission. *Science* **372**, 393-397 (2021).

[5] J. S. Hwang, J. Xu, A. P. Raman, Simultaneous control of spectral and directional emissivity with gradient epsilon-near-zero InAs photonic structures. *Advanced Materials* **35**, 2302956 (2023).

[6] F. Zhong, et al. Angle-resolved thermal emission spectroscopy characterization of non-Hermitian metacrystals. *Physical Review Applied* **13**, 014071 (2020).

[7] A. Bichri, et al. Characterization of Berreman modes in metal/dielectric Ag/SiO2 and Ag/MgF2 multilayers. *Journal of Physics*: *Condensed Matter* **9**, 6523-6532 (1996).

[8] T. Taliercio, et al. Brewster "mode" in highly doped semiconductor layers: an all-optical technique to monitor doping concentration. *Optics Express* **22**, 24294-24303 (2014).

[9] Z. Zhang & L. X. Zhu, Broadband nonreciprocal thermal emission. *Physical Review Applied* **19**, 014013 (2023).

[10] S. J. Ghalekohneh, C. K. Du, B. Zhao, Controlling the contrast between absorptivity and emissivity in nonreciprocal thermal emitters. *Applied Physics Letters* **124**, 101104 (2024).

[11] A. Caratenuto, et al. Magnetic field-induced emissivity tuning of InSb-based metamaterials in the terahertz frequency regime. *Optical Materials Express* **11**, 3141-3153 (2021).

[12] I. Crassee, et al. Intrinsic terahertz plasmons and magnetoplasmons in large scale monolayer graphene. *Nano Letters* **12**, 2470-2474 (2012).

[13] S. Pajovic, et al. Intrinsic nonreciprocal reflection and violation of Kirchhoff's law of radiation in planar type-I magnetic Weyl semimetal surfaces. *Physical Review B* **102**, 165417 (2020).

[14] B. Zhao, et al. Axion-field-enabled nonreciprocal thermal radiation in Weyl semimetals. *Nano Letters* **20**, 1923-1927 (2020).

[15] Y. Park, et al. Violating Kirchhoff's law of thermal radiation in semitransparent structures. *ACS Photonics* **8**, 2417-2424 (2021).

[16] Y. Dong, et al. Fizeau drag in graphene plasmonics. *Nature* **594**, 513-516 (2021).

[17] L. J. Xu, et al. Diffusive Fizeau drag in spatiotemporal thermal metamaterials. *Physical Review Letters* **128**, 145901 (2022).

[18] S. A. H Gangaraj, F. Monticone, Drifting electrons: nonreciprocal plasmonics and thermal photonics. *ACS Photonics* **9**, 806-819 (2022).

[19] A. Ghanekar, et al. Nonreciprocal thermal emission using spatiotemporal modulation of graphene. *ACS Photonics* **10**, 170-178 (2023).
[20] L. Wang, et al. Maximal violation of Kirchhoff's law in planar heterostructures. *Physical Review Research* **5**, L022051 (2023).

Chapter 5

Thermal lensing

"The lamps are different, but the Light is the same."

- Rumi

5.1 Introduction to self-focused thermal emission

In the previous three chapters, we described and demonstrated nanophotonic thermal emitters that broke Kirchhoff's law of thermal radiation. The method through which this was achieved was by limiting the number of optical modes of the structures (i.e. guided modes and Berreman modes) to the frequencies where nonreciprocal behavior was anticipated.

In these designs, there is a strict relationship between the momentum (wave-vector) and the energy (wavelength) at which the radiation outcouples [1] (see Figure 5.1). Realizing structures

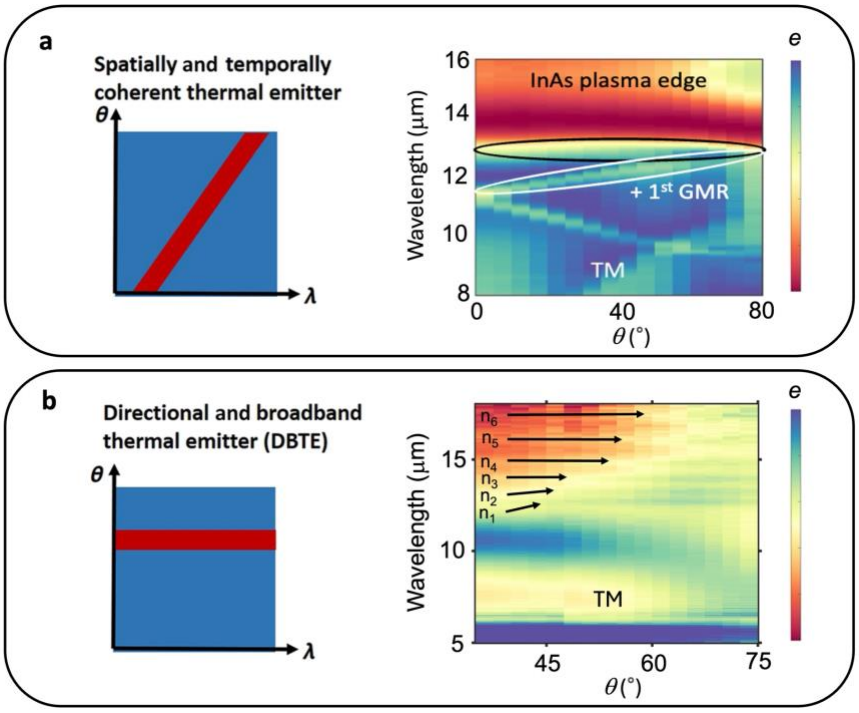

Figure 5.1 Spatial-temporal coherence relations of nanophotonic thermal emitters. (a) Spatially and temporally coherent thermal emitter where the angle at which the thermal emission efficiently outcouples has a strict wavelength dependence (left), implemented with a GMR structure in Chapter 2 (right). **(b)** Directional broadband emission (left), realized through a set of ENZ-resonances coupled to a Berreman mode (right). Figures on left of **(a)** and **(b)** are adapted from reference 1. Right panel of (**a**) and right panel of (**b**) taken from Chapters 3 and 4 respectively.

that both support extended modes and complex phase profiles presents an inherent tradeoff. The more the long-range order of a resonant photonic structure is perturbed, the lower the in-plane coherence length will be.

There has been a theoretical study that uses surface phonon polaritons [2] to impart in-plane coherence while varying the spacing and dimensions of scatterers to realize a complex spatial phase profile for thermal lensing. Another method of realizing self-focused thermal emission has been through optimizing neighboring scatterers surrounding a central, thermal emitter. In this design, the emission is not truly "thermal" across the sample surface, as only one mode is being thermally populated and the neighboring scatterers are completely passive (Figure 5.2).

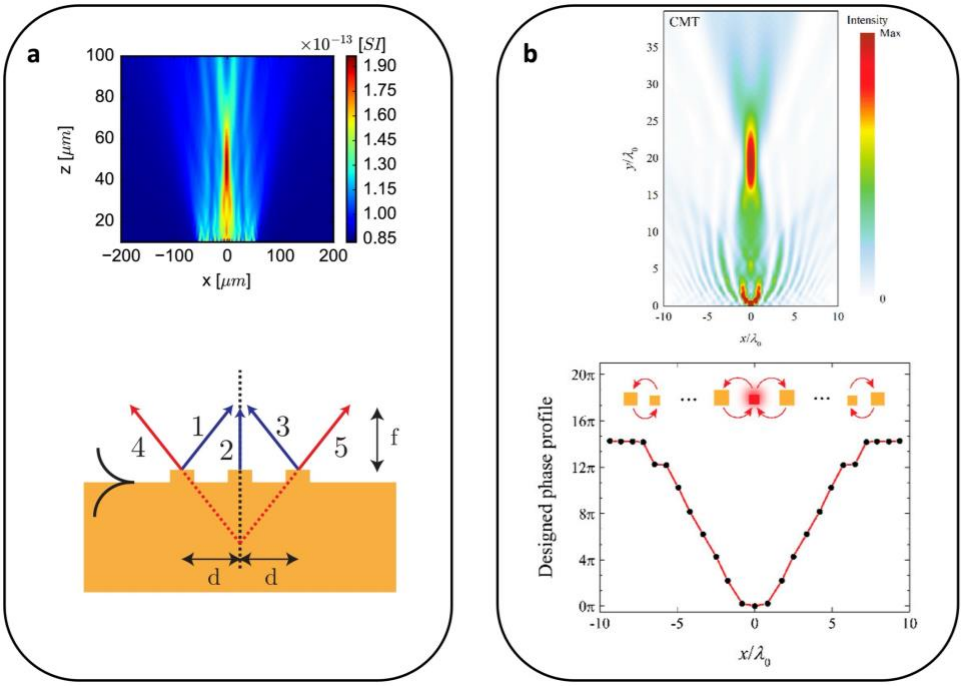

Figure 5.2 Theoretical predictions of self-focused thermal emission. (a) Upper panel: the TM-polarization electric-field intensity for a design (lower panel) where SPhPs are scattered out with varying efficiency (mediated by scatterer width) and phase (determined by resonator spacing, d). **(b)** Self-focused thermal emission from a single, emissive particle at the center of a finite array. The designed phase profile for the operation wavelength is found through an optimization using coupled mode theory. Figure (**a**) is taken from reference 2. Figure (**b**) is taken from reference 10.

In this chapter, we propose and fabricate a structure with self-focused (i.e. lensing) thermal emission with a collective resonance known as the Rayleigh anomaly to impart long-range, in-plane spatial coherence combined with varying local resonances to realize a spatial phase profile across the finite array. We then find the optimal scatterer profile using particle-swarm optimization to produce focal points at varying distances and operational wavelengths. We envision that this thermal lens will yield fundamental insights into the limits of nanophotonic engineering of thermally emitted light's coherence as well as applications in infrared sources and sensors.

5.2 Nonlocal and collective resonances for thermal lensing

In this section, we discuss the mechanism through which we engineer the spatial coherence over the surface of a thermal lens. Recent works have leveraged the extended spatial coherence provided by guided modes [3] and leaky-wave modes [4] to realize asymmetric thermal emission and lensing in conventional metasurfaces, respectively. Such nanophotonic designs rely on engineering a mode that is defined by a long-range order parameter (e.g. perturbation period, waveguide thickness, etc.). Our design relies on what is called a "collective" mode, however the approximate description can be captured in the confines of a nonlocal mode. The distinction between nonlocal and collective modes is that the collective mode's properties come from the coupling dynamics between individual, local resonances. The coupling modifies the long-range in-plane coherence (e.g. quasi-bound state in the continuum (q-BiC) [5] and surface lattice resonance (SLR) [6]).

The design in this chapter relies on a Rayleigh anomaly, whose first two modes, $\boldsymbol{\lambda}_{RA,\ 1}$ and $\boldsymbol{\lambda}_{RA,\ 2}$ can be approximated analytically by the spacing of the individual resonators of the array, Λ, as:

$$\boldsymbol{\lambda}_{RA,\ 1} = n\,\Lambda\,(1 \pm \sin(\theta)) \qquad \text{(Eq. 5.1)}$$

$$\boldsymbol{\lambda}_{RA,\ 2} = {}^{1}/_{2}\, n\,\Lambda\,({}^{1}/_{2} \pm \sin(\theta)) \qquad \text{(Eq. 5.2)}$$

where n is the refractive index and θ is the incidence angle.

One notes that the above dispersions have no dependence on the local resonances that compose the array (i.e. we can consider the above treatment as a nonlocal mode). We will cover how the dispersion of the modes is affected by the coupling of the individual resonances in the following section. With the in-plane coherence provided by the Rayleigh anomaly, we can engineer

a phase response across the surface of the array by varying the spectral position of local resonances relative to the collective resonance. We show the concept schematically in Figure 5.3 a. Suppose one wants a thermal lens with focal length of 187 μm and operation wavelength of $\lambda = 3.6$ μm. If the array has a constant spacing, $\Lambda = 5$ μm, the structure will have dispersive Rayleigh anomaly modes shown in the absorptivity versus wavelength vs angle of incidence plots shown in Figure 5.3 b. For the desired operational wavelength of 3.6 μm (dashed black line), we find that the Rayleigh anomaly outcouples at $\theta \sim 24°$ (dashed red line). Correspondingly, we would want a particle with local resonance, $\lambda_{res} = 3.6$ μm, placed 80 μm from the center of the lens (position 16 when $\Lambda = 5$ μm). The in-depth design and optimization process is laid out in section 5.3.

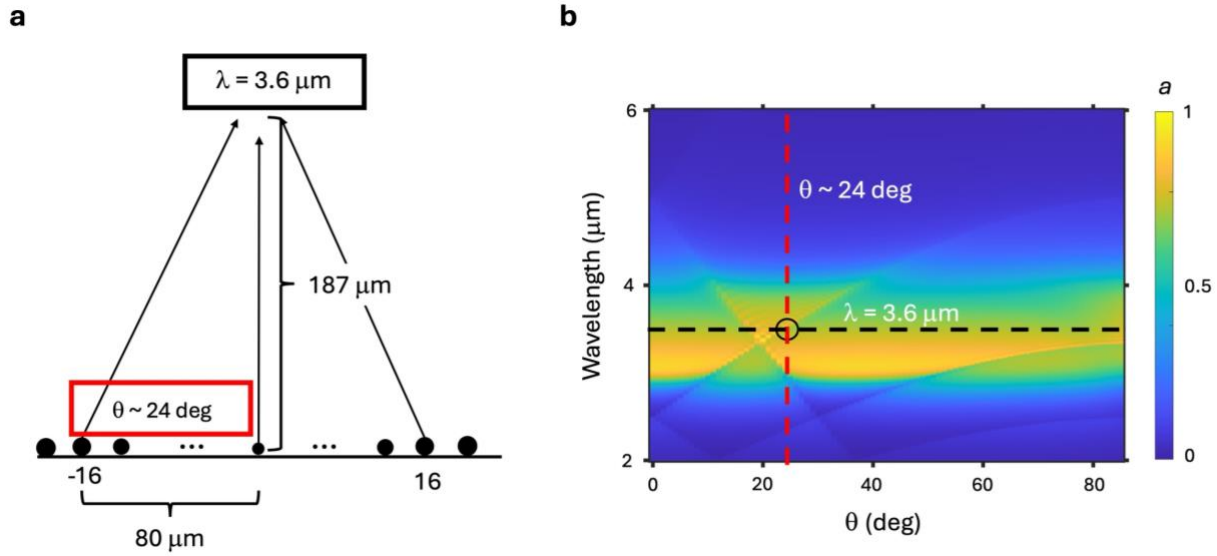

Figure 5.3 Schematic conceptualization of thermal lensing with finite arrays of resonant particles. (**a**) Assuming a focal length of 187 μm and operation wavelength of $\lambda = 3.6$ μm (black box), one would want the 16th particle (80 μm from the center of the lens) to resonantly outcouple at $\theta \sim 24°$. (**b**) Spectral-angular absorptivity of a finite array (41 particles) with spacing $\Lambda = 5$ μm and local resonances 3 μm $< \lambda_{res} <$ 4 μm. At 3.6 μm (dashed black line) the Rayleigh anomaly outcouples at $\theta \sim 24°$ (dashed red line). This corresponds to having $\lambda_{res} = 3.6$ μm for particle 16 in the array depicted in (**a**).

We realize the structure described above with germanium nanorods of height 600 nm on a gold back-reflector (Figure 5.4). The fabrication process is described in-depth in section 5.4 of this chapter. The parameters that we can tune are the pitch (spacing), Λ, between the individual resonators, and the local resonances of the individual nanorods, w. We use thin-film germanium because of its relatively flat optical constants across the infrared (n ~ 4.13 and k ~ 0.003). The non-zero k allows for absorption/emission from the rods. The gold acts as a perfect reflector, suppressing all absorption/emission from the substrate underneath the sample.

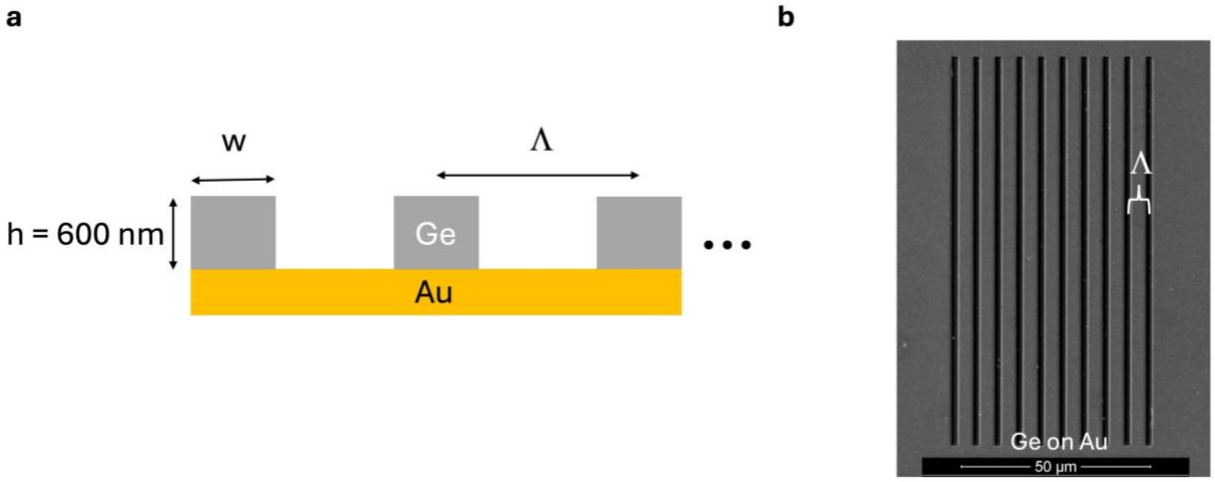

Figure 5.4 Germanium-on-gold resonators. (**a**) Germanium resonators with constant pitch (Λ) set the condition for the nonlocal resonance of the array. The heights of the germanium rods are fixed across all samples at 600 nm. By varying the width of individual resonators, w, we can tune the local resonance, λ_{res}. (**b**) SEM micrograph of finite array with Λ = 5 μm.

5.3 Coupled dipole approximation and optimization process*

The coupled dipole approximation (CDA) has been used in various contexts to predict and model the optical responses of periodic lattices [7, 8]. For the thermal lens designs presented in this chapter, we use the CDA for finite arrays. The CDA has previously been used to predict phase gradients in finite nanoparticle chains in homogeneous media [9], which almost exactly mirror our system, barring the back-reflector beneath the germanium nanorods. In the CDA for finite arrays,

* The derivation of the coupled dipole approximation for finite arrays follows that presented in reference 9.

we capture the dipole moment at particle in position $\boldsymbol{r}_i$ that has been illuminated by a plane-wave incident on the entire array as

$$p(\boldsymbol{r}_i) = \boldsymbol{\alpha}_{s,i} E_{loc,i} \quad \text{(Eq. 5.3)}$$

where $\boldsymbol{\alpha}_{s,i}$ is the polarizability of the particle and $E_{loc,i}$ is the "local" electric field at $\boldsymbol{r}_i$ from both the impinging field, $E_{app,i}$, and the delayed scattered fields from the neighboring particles, $E_{sca,i}$:

$$E_{sca,i} = \sum_{j \neq i} G_{ij} p_j \quad \text{(Eq. 5.4)}$$

where G_{ij} is the dipolar Green function that describes the coupling between dipoles at positions i and j. We can express the indices i and j alternately as the position separation, $q = |i - j|$, with the particles being a distance $r_q = q\Lambda$ apart. The electric dipole Green function then takes the form:

$$G_q = g_q e^{ikr_q} \quad \text{(Eq. 5.5)}$$

where

$$g_q = \left[\frac{(1 - ikr_q)(3cos^2\theta_q - 1)}{{r_q}^3} + \frac{k^2 sin^2\theta_q}{r_q} \right] \quad \text{(Eq. 5.6)}$$

for wavenumber $k = 2\pi n/\lambda$ and angle between the incident-field polarization and the in-plane displacement vector, θ_q. We then have N linear equations describing the applied electric field at each particle,

$$\hat{A}p = E_{app} \quad \text{(Eq. 5.7)}$$

where p is the $N \times 1$ dipole moment vector and $\hat{A}$ is the $N \times N$ interaction matrix:

$$A_{ij} = \begin{cases} {\alpha_s}^{-1}, i = j \\ -G_q, i \neq j \end{cases} \quad \text{(Eq. 5.8)}$$

The dipole moments of the individual particles can then be found through inverting $\hat{A}$.

To assess the viability of modeling the germanium nanorods with the CDA, we fabricate and measure the absorptivity of individual rods with constant height (600 nm) and varying widths (400 – 850 nm). We confirm the individual particle widths after fabrication through SEM (Figure 5.5 a). In this chapter, due to reciprocity, Kirchhoff's law applies and the measured absorptivity of individual rods is equal to the emissivity. The spectra obtained from FTIR reflectivity measurements are shown in Figure 5.5 b and c, with Lorentzian fits of the individual particle scattering:

$$\alpha_s = \frac{A}{{\omega_0}^2 - \omega^2 - i\gamma\omega} \qquad \text{(Eq. 5.9)}$$

where ω_0 is the frequency of the principle resonance, A is the amplitude, and γ the spectral width of the resonance. With the individual particle polarizability, we can calculate the scattering amplitude and phase at a specific wavelength (e.g. λ = 5 μm) for varying local resonance (λ_{res}) values.

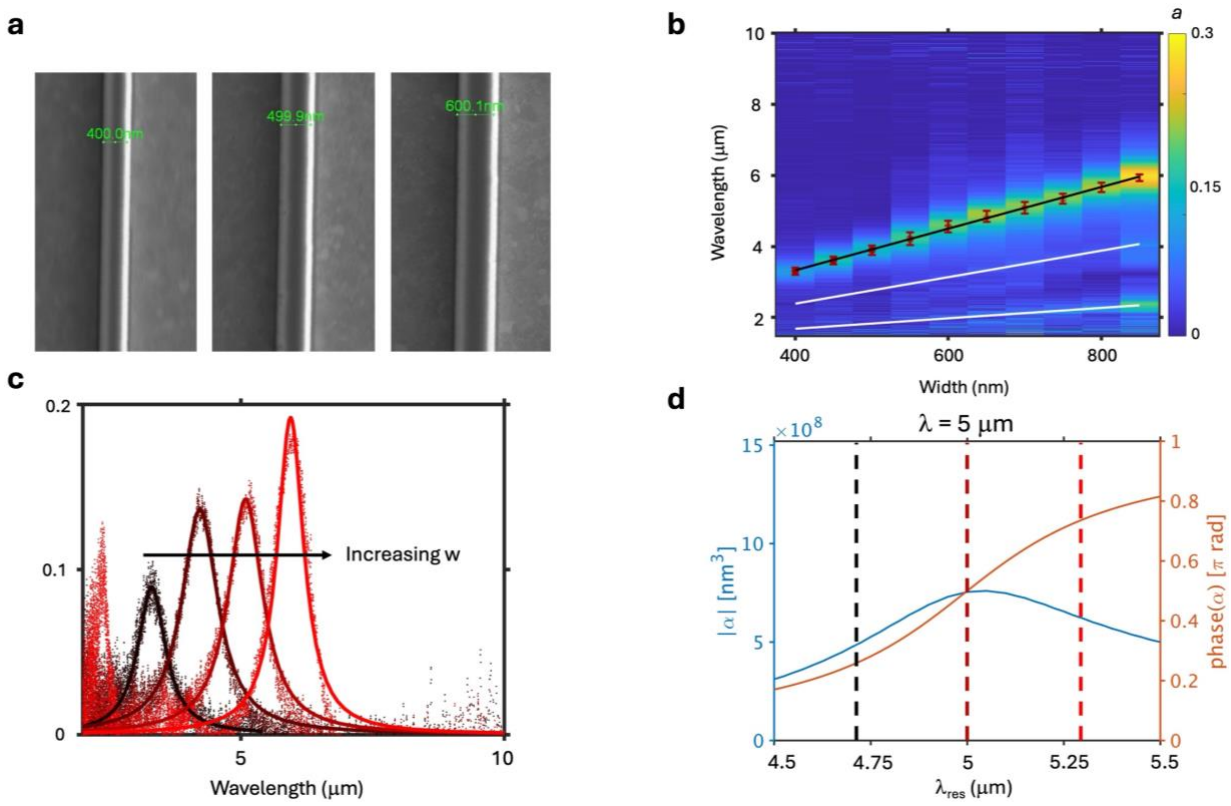

Figure 5.5 Spectra of individual germanium rods with varying widths. (**a**) SEM measurements of individual germanium nanorod widths. (**b**) Absorptivity data for all rods fabricated, where the extracted ω_0 are overlaid with error bars. The ω_0 values are fit linearly as a function of rod width afterwards. White lines trace out the higher-order resonances. (**c**) The scatter-points are experimental data from FTIR reflectivity measurements. The solid lines are Lorentzian fits of the data. The widths of the rods increase linearly from 400 nm to 850 nm, resulting in a redshift in the fundamental resonance. Higher-order resonances are also visible (red trace, ~ 3 μm) and are considered in the optimized lens designs. (**d**) Amplitude and phase response of particles at 5 μm when the resonance wavelength (λ_{res}), or alternatively ω_0, varies. The dashed lines approximately mark the three longer-wavelength resonances from (**c**).

After obtaining a model for the individual particle polarizability, we look to the CDA to model the collective effects of the germanium nanorods. To test this, we fabricate a set of arrays with constant particle width (600 nm) and vary the particle spacing, Λ. We then perform angle-

resolved emissivity and absorptivity measurements on the samples (Figure 5.6). Because of the higher signal-to-noise ratio, we focus on the data obtained through absorptivity measurements.

We observe that the theoretical and CDA-predicted 1st order Rayleigh anomalies align exactly with each other and with the measured values. This is expected, as the 1st order Rayleigh anomaly lies well outside the spectral range of the local resonance wavelength of the 650 nm nanorods, and consequently we would not anticipate any collective dynamics to affect the nonlocal mode. However, the theoretical 2nd order Rayleigh anomaly condition (Figure 5.6 b, red dashed

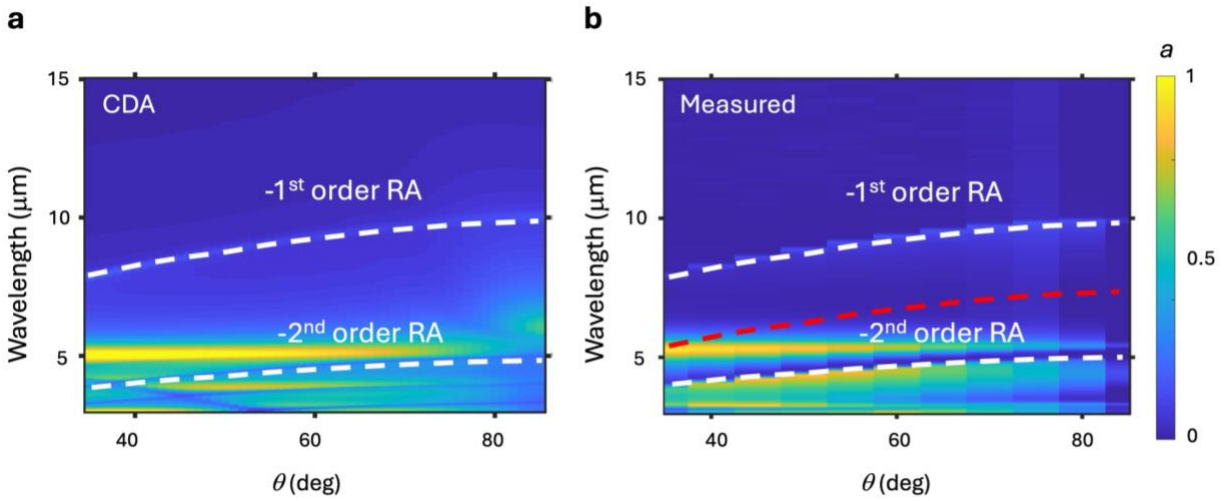

Figure 5.6 Spectra of germanium rod arrays with Λ = 5 μm (**a**) CDA-predicted absorptivity spectra as a function of angle, with the -1st and -2nd order Rayleigh anomalies (RA) marked out with dashed white line (**b**) Measured absorptivity data for sample with the same fabricated parameters as in (**a**). The red dashed line is the -2nd order Rayleigh anomaly without any inter-particle coupling accounted for.

line) compared with the CDA (Figure 5.6 b, white dashed line) shows that there is a significant correction when the local resonances and inter-particle coupling are accounted for.

Now that we can accurately capture the individual particle polarizability (Figure 5.5) and the collective dynamics (Figure 5.6) of the system, we can optimize a structure to produce "focused" emission at a given focal length, for a given wavelength. One main advantage of the CDA is the rapid speed-up of simulation time compared to full-wave simulations (days-long simulations take a few seconds). As a result, we can run multiple consecutive simulations while iteratively changing the input parameters.

Using particle-swarm optimization (PSO), we define an objective function that the parameter adjustments iteratively try to minimize. We define the objective function as a negative

2nd derivative of the electric field intensity as a function of displacement from the center of the lens, i.e. a concave-down intensity around the desired focal points (120 μm, 160 μm, and 187 μm) (Figure 5.7 a). The parameter we optimize to reach our focal point objective is the individual rod resonance wavelength (λ_{res}). We can, in principle, open the optimization up to the spacing, Λ, as well. We limit the optimization to individual rod resonances with fixed Λ to observe the local resonance profile requirement for different focal lengths. The particle resonances as a function of position are randomly populated before the optimization is run.

The optimized λ_{res} are shown as a function of particle position in Figure 5.7 b for a thermal lens operating at 3.6 μm. As the focal length grows, the positions of the λ_{res} that approach the design wavelength move towards the edge of the thermal lens. This is intuitive according to Figure 5.3 a, as Λ is fixed across the designs, meaning that the resonant diffractive condition is being pushed towards the side of the lens while the angle is held constant. As a result, the two diffractive beams meet farther away from the sample surface.

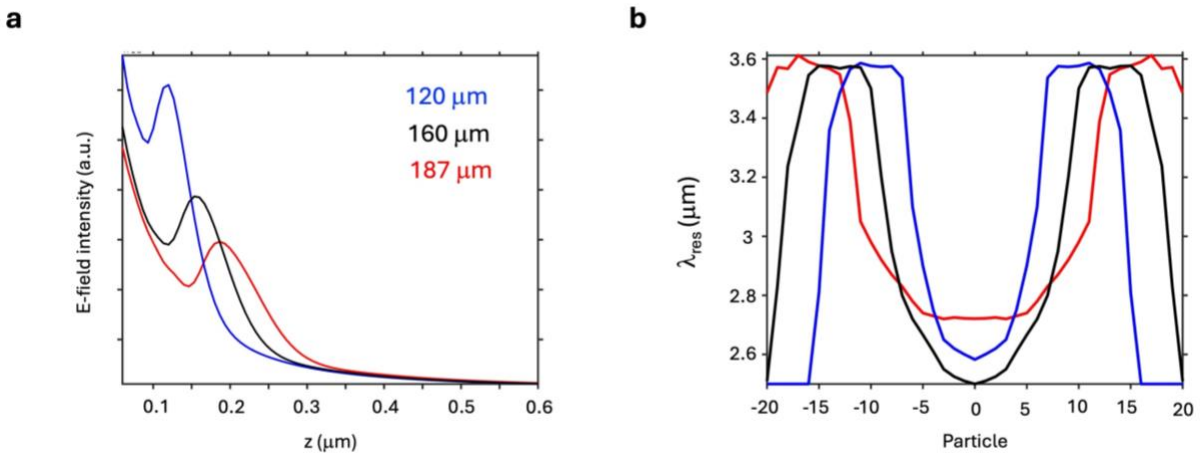

Figure 5.7 Optimized thermal lenses for 3.6 μm with varying focal lengths. (**a**) Electric field intensity as a function of distance (z) from the surface of the thermal lens for three different focal lengths. (**b**) Resonant wavelength as a function of particle position for the three focal distances in (**a**). The longer the focal distance, the closer to the side of the thermal lens the "on-resonance" resonators are positioned.

We plot the far-field electric field intensity in Figure 5.8 for the three varying focal length designs. The most striking observation is that the thermal lenses have two side-lobes that beam the radiation strongly away from focus. This is because the Rayleigh anomaly which strongly couples to the edge resonators with λ_{res} = 3.6 μm has a symmetric dispersion, coupling to both the + and –

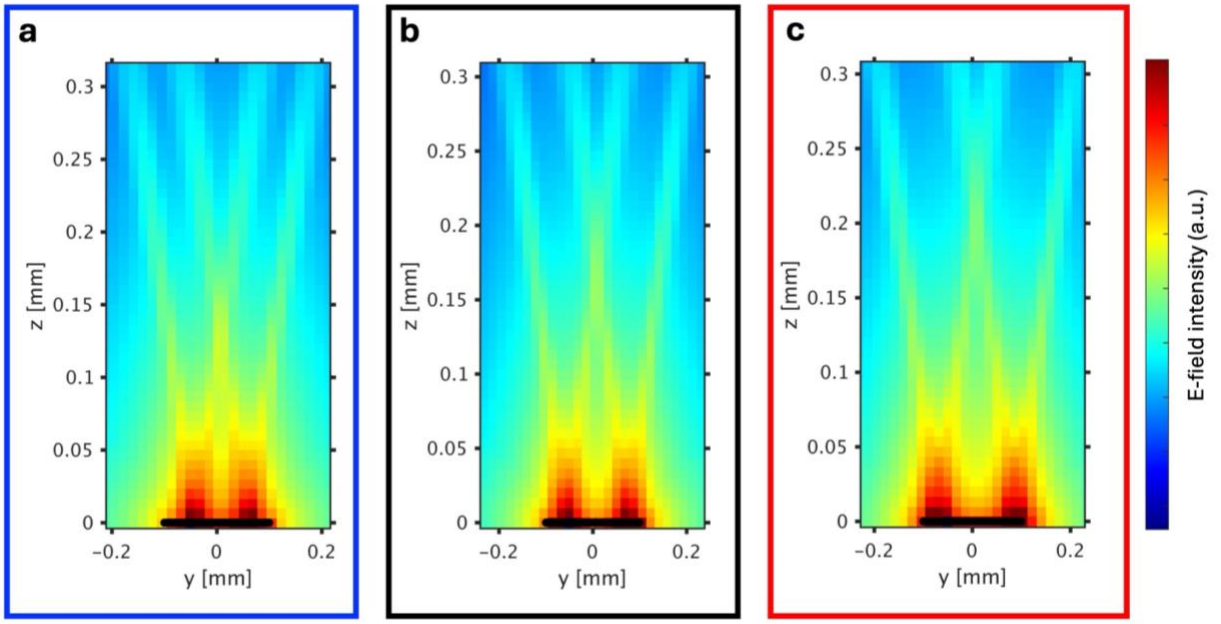

Figure 5.8 Electric field intensity plots of the optimized thermal lenses at 3.6 μm. (**a**) 120 μm focal length (**b**) 160 μm focal length (**c**) 187 μm focal length. The black bar at the bottom is the nanorod array, the size of which is constant (205 μm for N = 41 particles) across all three devices.

θ angles. While having a slight wavelength gradient around these "flat" resonance wavelength regions at the side of the thermal lens allows some asymmetry of the outcoupled emission towards the center of the lens, this represents a challenge faced in other thermal lens designs (see Figure 5.2) [10, 2].

5.4 Fabrication and measurements of thermal lenses

From our fits shown in Figure 5.5 b, we can make a direct correlation between the desired λ_{res} profiles in our CDA optimization and the widths of the corresponding germanium nanorods. For sample fabrication, we begin by depositing a 10 nm titanium adhesion layer and 80 nm gold back reflector on a silicon wafer via electron beam evaporation. After depositing the back-reflector, we run a cleaning process through a sonicated bath of isopropyl alcohol (IPA) and acetone. Once the sample surface is cleaned, we spin on a bilayer resist of polymethyl methacrylate (PMMA) 495 A8 at 1000 RPM for 1 minute and PMMA 950 A4 at 1500 RPM for 1 minute, yielding a total resist thickness of 1.33 μm. We anneal both layers at 180 ° C for 5 minutes.

After depositing the bilayer resist, we expose the sample in a Raith electron beam pattern generator at 10 nA with a 300 μm aperture and use a 1200 uC/cm^2 dose. We develop the exposed pattern in a methyl isobutyl ketone (MIBK) : IPA solution (1:3 ratio) for 1 minute and 45 seconds. With the patterns now in our resist, we again use electron beam evaporation to deposit 600 nm of germanium. This is a large amount of material to deposit using electron beam evaporation, and the radiative heat transfer and material flux onto the sample surface can change the surface morphology of the deposited germanium. We find that increasing the deposition rate from standard 1 Å/s to 2 Å/s results in a smoother germanium film. We believe that this is due to the reduced time the sample spends in the chamber, allowing less time for the sample to be heated by the source.

The final step of the fabrication process is to lift-off the PMMA bilayer resist stack and germanium not in contact with the gold surface. We do this using Remover PG, which we heat with the samples in the solution up to 55 °C for one minute and then leave to soak for another 12 hours. Because the sample areas are quite large (300 μm x 300 μm), there are residual pieces of germanium on the sample surface that we gently wash away with a direct stream of Remover PG. Once all residual germanium has been cleared, we dry the sample with nitrogen.

We use two methods to determine the spacing and widths of the germanium rods, namely SEM and atomic force microscopy (AFM). To determine the thickness of the deposited germanium, we rely on ellipsometry and AFM. In Figure 5.9, we show the obtained height profile and spacing of the rods through AFM. The 600 nm thickness was obtained after multiple iterations of electron beam evaporation, ellipsometry, AFM, and updates to the electron beam evaporator's tooling factor.

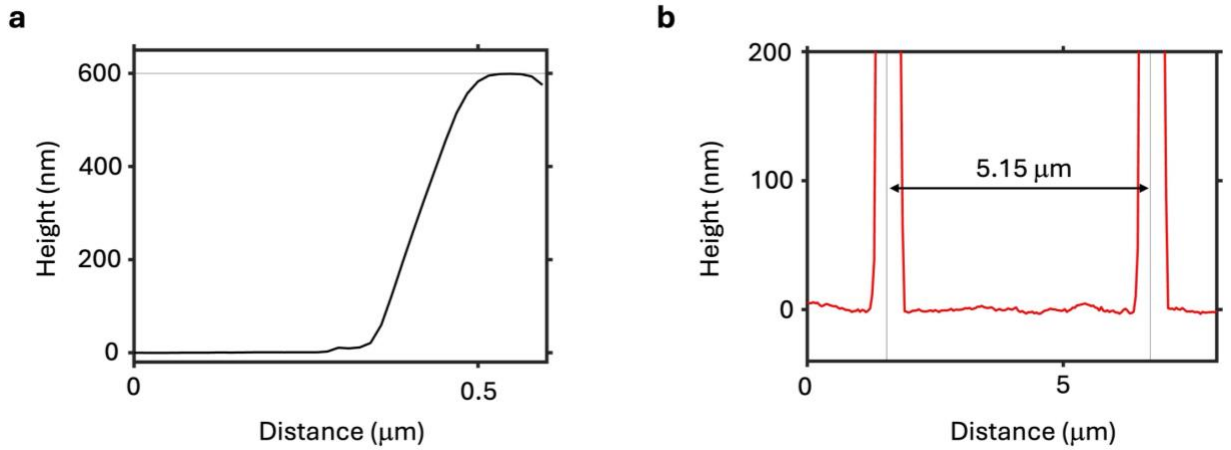

Figure 5.9 AFM measurements of the germanium rod heights and spacing. (**a**) Measurement of the germanium rod height (light line is at height = 600 nm) (**b**) Measurement of the inter-particle spacing. We aimed for 5 μm spacing and find the inter-particle spacing is approximately 5.15 μm.

Once the fabrication process yields consistent nanorod heights, widths, and spacings, we fabricate the desired thermal lens with the optimized λ_{res}. We show the 187 μm-focal-length lens spectra for the constituent rods in Figure 5.10 a. The overlaid black line is the desired resonant wavelength profile. We show an SEM of portion of the lens from particles 12 – 15 in Figure 5.10 b, showing the width gradient that corresponds to the wavelength gradient in Figure 5.10 a.

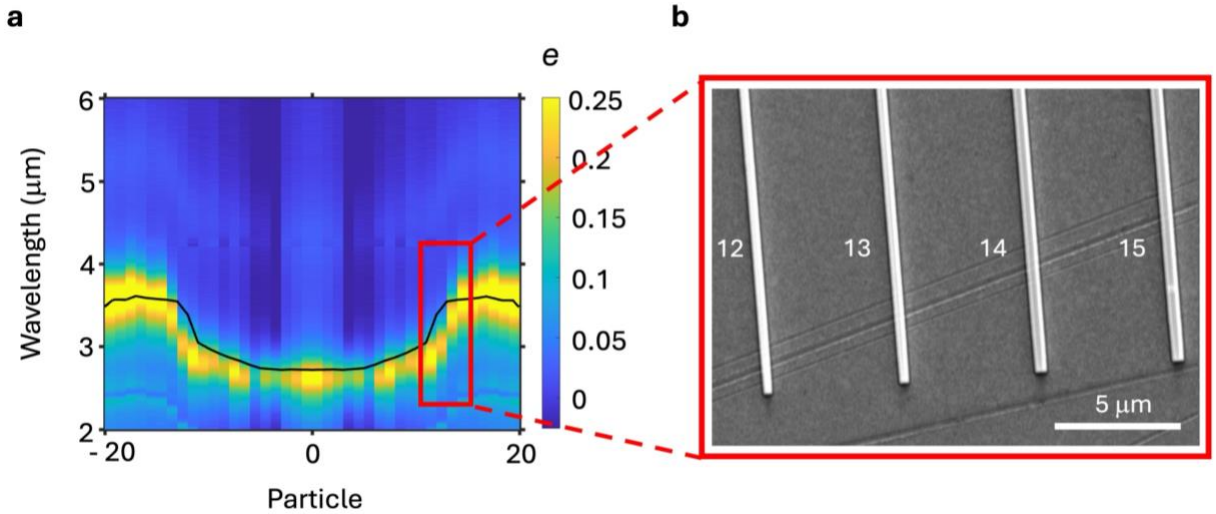

Figure 5.10 Fabricated rod spectra for thermal lens design. (**a**) The absorptivity/emissivity spectra of individual particles for the 187 μm focal length thermal lens. The overlaid black line is the optimized λ_{res} versus position according to the CDA-PSO. (**b**) SEM images of the thermal lens with pitch Λ = 5 μm from particle positions 12 – 15.

5.5 Summary and outlook

We envision that the design process laid out in this chapter will expedite the realization of thermal metasurfaces, in particular thermal lenses. We laid out an efficient way to model the collective dynamics of resonant, thermally emitting finite arrays of nanoparticles using the coupled dipole approximation. After successfully modeling the collective dynamics, we leveraged the speed of the coupled dipole approximation in comparison to full-wave simulations to run an optimization of finite arrays with constant spacing, while varying the local resonance wavelengths of the individual particles. In this chapter, we choose three varying focal lengths for a finite array of particles (N = 41 particles) with constant spacing (Λ = 5 μm) to demonstrate thermal lensing at 3.6 μm. We emphasize that the wavelength of operation spans a 0.5 μm around 3.6 μm, and that the design wavelength and focal lengths can be arbitrarily set. The spacing should also be included as an optimization parameter in future iterations to improve the focusing efficiency.

After finding optimal resonant wavelength profiles according to the CDA-PSO, we designed a process to efficiently fabricate the lens out of germanium nanorods. We show that we can accurately engineer the germanium nanorods' resonant wavelengths by varying their widths and performing FTIR reflectivity measurements on individual and coupled arrays of rods.

We propose that a direct measurement of the thermal emissivity be done using a lens-coupled FTIR spectrometer, as in Chapters 4 and 5. The benefit of using a ZnSe lens over the high numerical aperture (NA = 0.58) Cassegrain objective is that we limit the focal point and thermal lens aperture convolution that occurs as we move the thermal lens surface out of the focus of the objective. Future measurements should, however, continue using a wavelength-resolved spectrometer to measure the wavelength bandwidth of the thermal focusing effect. For this reason, we opt for an FTIR as opposed to a mid-wavelength infrared camera with a series of spectrally selective filters.

Future work could incorporate symmetry-breaking designs and external fields to realize stronger preferential coupling towards the center of the thermal lens, thereby improving efficiency. The structures presented in this chapter are one-dimensional, however one could extend the concept to two dimensions and encode different functionalities along different directions. Finally, the resonators need not be limited to germanium. Substituting a phase-change material (e.g. VO_2) or electro-optic material (e.g. ITO) for germanium could enable a reconfigurable or switchable thermal lens [11, 12].

References

[1] Y. Qu, M. Pan, M. Qiu, Directional and spectral control of thermal emission and its application in radiative cooling and infrared light sources. *Phys Rev. Applied* **13**, 064052 (2020).

[2] H. Chalabi, A. Alu, M. L. Brongersma, Focused thermal emission from a nanostructured SiC surface. *Phys. Rev. B* **94**, 094307 (2016).

[3] J. Yu, R. Qin, Y. Ying, M. Qiu, Q. Li, Asymmetric directional control of thermal emission. *Advanced Materials* **35**, 2302478 (2023).

[4] H. Huang, A. C. Overvig, Y. Xu, S. C. Malek, C.-C. Tsai, A. Alu, N. Yu, Leaky-wave metasurfaces for integrated photonics. *Nature Nanotechnology* **18**, 580-588 (2023).

[5] J. R. Nolen, A. C. Overvig, M. Cotrufo, A. Alu, Local control of polarization and geometric phase in thermal metasurfaces. *Nature Nanotechnology* **19**, 1627-1634 (2024).

[6] V. G. Kravets, A. V. Kabashin, W. L. Barnes, A. N. Grigorenko, Plasmonic surface lattice resonances: a review of properties and applications. *Chem Rev.* **12**, 5912-5951 (2018).

[7] B. T. Draine, P. J. Flatau, Discrete-dipole approximation for scattering calculations. *JOSA A* **11**, 1491-1499 (1994).

[8] M. A. Yurkin, A. G. Hoekstra, The discrete dipole approximation: an overview and recent developments. *Journal of Quantitative Spectroscopy and Radiative Transfer* **106**, 558-589 (2007).

[9] L. Michaeli, O. Doron, Y. Hadad, H. Suchowski, Rayleigh anomaly induced phase gradients in finite nanoparticle chains. *Nanoscale* **15**, 13653-13665 (2023).

[10] M. Zhou, E. Khoram, D. Liu, B. Liu, S. Fan, M. L. Povinelli, Z. Yu, Self-focused thermal emission and holography realized by mesoscopic thermal emitters. *ACS Photonics* **8**, 497-504 (2021).

[11] R. Audkhasi, Y. Qu, M. Zhou, Z. Yu, M. L. Povinelli, Dynamically switchable self-focused thermal emission. *Optics Express* **8**, 13357-13365 (2023).

[12] R. Sokhoyan, P. Thureja, J. Sisler, M. Grajower, K. J. Shayegan, E. Feigenbaum, S. Elhadj, H. A. Atwater, Electrically tunable conducting oxide metasurfaces for high power applications. *Nanophotonics* **12**, 293-253 (2023).

Chapter 6

Summary and outlook

"All things must pass
None of life's strings can last
So I must be on my way
And face another day…"

- George Harrison

6.1 Summary

At the outset of this thesis, we stated that the scope was to leverage nanophotonic and plasmonic fundamentals to demonstrate new effects in the context of thermal emission. We begin this chapter by reviewing the advancements in this regard:

1. In Chapter 2, we began by deriving Lorentz reciprocity relations and highlighting the dependence of Lorentz reciprocity on symmetric permittivity, ε, and permeability, μ, tensors. We then connect Lorentz reciprocity to Kirchhoff's thermal radiation law. We show that if the reflectivity of structure is nonreciprocal, it should violate Kirchhoff's thermal radiation law.

   We then lay out the theory that degenerately-doped InAs has a strong magneto-optic (and nonreciprocal) response at the plasma wavelength when a transverse magnetic field is applied. This nonreciprocal response is due to the permittivity scalar becoming an anti-symmetric tensor.

   To enhance light-matter interaction at the plasma wavelength, we turn to a α-Si GMR structure with a symmetric dispersion with no applied magnetic field that resonantly couples to the InAs underneath. Despite the GMR structure not having a magneto-optic response itself, the coupling between the structure and the InAs is strongly modified in the presence of an external magnetic field.

   Using a Halbach array to apply the magnetic field across the device, we perform a set of reflectivity measurements to show asymmetric and nonreciprocal absorptivity in the infrared. We show that the changes in the angular dispersion and resonance linewidth from the magnetic field are captured in frequency domain COMSOL simulations.

2. In Chapter 3, we demonstrate a direct violation of the Kirchhoff thermal radiation law in experiment. Building on the same design concepts from the preceding chapter, we make temperature-dependent refractive indices measurements and re-design the structure from Chapter 2 to have a resonance at shorter wavelengths (~12.5 μm – 13 μm). The reasoning behind this is that to perform direct spectral, directional emissivity measurements, we need to heat the sample above room temperature so that the emission from the sample exceeds the emitted radiation from the background. The Stefan-Boltzmann law, relating the emitted intensity to the body's temperature as

$$I_T \propto T^4$$

shows that heating the sample moderately above room temperature (50 – 100° C) provides a sufficient boost to the radiated intensity.

After modeling and fabricating the sample, we build a custom angle and polarization-resolved thermal emissivity setup where a tunable external magnetic field can be applied. Before performing any magneto-optic measurements, we ensure that our emissivity and absorptivity measurements produce the same spectral, directional data (i.e. confirm that the systems are the same when obeying Lorentz reciprocity).

We then perform measurements of both the absorptivity and emissivity under an external magnetic field, the first of their kind, and demonstrate a violation of the Kirchhoff thermal radiation law.

In the emissivity setup, we probe and quantify the behavior of the sample through fine-tuning of the magnetic field. This is possible due to our use of an electromagnet as opposed to a Halbach array in the emissivity setup. We are able to identify the different coupling regimes, and identify a saturation of the enhanced emissivity under large negative magnetic field as the sample's emissivity approaching the blackbody limit.

After analyzing the inequality in the spectral, directional emissivity and absorptivity, we confirm revised relations between the emissivity and absorptivity when Lorentz reciprocity is broken. These relations, the Onsager reciprocal relations,

$$\alpha(\lambda, -\theta, B) = e(\lambda, \theta, B)$$

are important in reinforcing that the second law of thermodynamics holds under the external magnetic field. If one were to integrate the spectral, directional emissivity and

absorptivity over the entire hemisphere of the sample surface, the total absorbed and emitted radiation are the same.

3. In Chapter 4, we use the same nonreciprocal effect of Chapters 2 and 3, however we enable a broadband tuning of the emissivity and absorptivity away from one another using a different photonic concept: the gradient-ENZ Berreman mode. In these MBE-grown samples, multiple ENZ-resonances of thin-film InAs are cascaded in the depth dimension as a "gradient". The total thickness of the stack determines the angle at which the radiation outcouples, with thinner samples coupling to larger angles and thicker samples radiating closer to normal incidence. Because the broadband emission is determined by the plasma wavelengths of the constituent layers of the gradient structure, we also expect strong nonreciprocal tuning of the emissivity and absorptivity at the same wavelengths.

   The Kirchhoff-violating behavior is measured over a spectral range 12.5 μm – 17 μm using the same measurement systems developed in Chapter 3. Beyond demonstrating the effect over a broadband spectral range, we measure two samples with varying thicknesses to assess the dependence of the nonreciprocal effect on the sample thickness. We show that the strongest tuning correlates to the optimal outcoupling angle of the Berreman mode, i.e. that the tuning for the thin sample is strongest at large angles and the thicker sample's strongest tuning is at $\theta = 60°$.

   However, even at the optimal angle for the thin sample ($\theta = 80°$) the tuning is lower in magnitude than the thick sample. We investigate this phenomenon further through simulation and find that the tuning is strongly thickness-dependent independent of angle outcoupling. Concisely, thicker samples exhibit stronger nonreciprocal behavior, up to a limit.

   Finally, the ordering of the gradient-ENZ has an impact on the tuning strength of the emissivity and absorptivity via magnetic field. We find that ordering the layers with increasing carrier concentrations deeper in the sample results in an overall stronger tuning over the entire spectral bandwidth. When higher carrier concentrations are closer to the sample surface, they act as a screening layer to layers deeper in the sample. A way to balance spectral uniformity with increased overall tuning is to implement a

structure with both a carrier concentration and thickness gradient of the individual layers along the depth dimension.

4. In Chapter 5, we move away from using nanophotonic structures (i.e. GMR, and Berreman modes) to realize and enhance Kirchhoff violation, and move towards reciprocal thermal emitters that realize complex functions, i.e. thermal lensing. The concept requires moving outside of the conventional metalens design toolbox to realize spatial coherence of the emitted radiation through a collective mode known as the Rayleigh anomaly. The Rayleigh anomaly relies on the period of a lattice of individual resonances, which we realize experimentally with germanium nanorods, to build coherence in the plane of the thermal lens.

   To understand and model the collective dynamics of the finite array, we use the coupled dipole approximation with modified individual particle polarizabilities to account for the effects of local resonances on the Rayleigh anomaly. We confirm the accuracy of the model by comparing coupled dipole approximation calculations of the 1^{st} and 2^{nd} order Rayleigh anomalies to the theoretical dispersions.

   We then vary the local resonances of the germanium nanorods constituting the array by changing the rod width. This tuning of the local resonances is varied over the sample surface to realize a complex scattering profile to realize a focal point above the sample. To realize a thermal lens experimentally, we map the germanium rod width to the local resonance wavelength. Once we have a width-resonance wavelength library, we define an objective function for the focal point and run a particle swarm optimization for the local resonances. For this operation, we iteratively run the coupled dipole approximation with varying local resonance profiles and constant particle spacing and array size.

   We find theoretical designs for three different focal lengths from the optimization process and fabricate the lenses as finite germanium arrays with varying individual particle widths. While we can measure the individual, uncoupled rod spectra and demonstrate a match between the desired wavelength design and the realized wavelength profile, direct emission measurements demonstrating thermal lensing are ongoing as of the writing of this thesis.

6.2 Outlook for Kirchhoff-violating structures

The demonstrations of Kirchhoff-violating thermal emitters discussed in this thesis have spurred a larger conversation in the radiative cooling and energy conversion community regarding the efficiency gains enabled by such structures [1, 2, 3]. Future experiments should assess whether there is measurable performance improvement for structures that exhibit strong nonreciprocal thermal emissivity and absorptivity. Recent works have demonstrated sub-ambient radiative cooling of vertical structures through asymmetric emissivity and absorptivity [4]. This is significant when considering constraints that an urban landscape would impose to cool the sides of buildings. The structures in Chapters 2 – 4 all exhibit asymmetric emissivity (and absorptivity) spatial profiles, however, have not be fully optimized to achieve full contrast across the + and - θ of the hemisphere. One avenue towards realizing such structures would be to implement a design process like that shown in Chapter 5 of this thesis. For a fixed magnetic field value, an objective function where the + and - θ contrast over a broadband wavelength and angular range is optimized for a set of structure parameters (e.g. layer-thickness, surface structure) using a fast computational method (e.g. transfer-matrix method). The optimized structure would need to be tested using a standard radiative cooling benchmarking system [5].

Another future direction for Kirchhoff-violating structures is implementing nonreciprocity that does not rely on magneto-optical effects. As evidenced by the work in Chapters 2–4, implementing devices with magneto-optic responses and applying the necessary magnetic field strengths to observe nonreciprocal emissivity and absorptivity is neither trivial nor easily scalable. In the near-field, nonreciprocal plasmon propagation has been demonstrated through applications of large currents along and against the direction of propagation of the plasmon [6]. While the application of a DC-bias is an attractive alternative to applying external magnetic fields, the currents required to modify the plasmon wavevector even a couple percent are prohibitive. A way to reduce the required modulation fields and enhance asymmetric absorptivity and emissivity would be to combine the momentum-shifting concept with a photonic transition. By designing a structure with two photonic modes, a spatio-temporal modulation at GHz modulation frequencies enables an indirect photonic transition that is allowed for positive but not negative wavevectors (and vice-versa) [7, 8]. Measurements demonstrating GHz modulation of electro-optic free-space

metasurfaces have been demonstrated [9], but not in the infrared nor in the context of thermal emission.

6.3 Outlook for thermal lensing

Direct measurements of thermal lensing are still ongoing as of the writing of this thesis. Beyond direct measurements and quantization of the coherence of complex thermal sources, we anticipate multiple extensions of the concept of the thermal lens that will rely on collective resonances. For example, local emitters in an array can be made individually addressable (e.g. through resistive or optical heating), and distinct lattice resonance modes can be excited based on which local resonance is thermally populated and coupled to the array. Depending on the lattice mode that is excited, the surface can be optimized to have a specific spatial scattering profile for that specific wavelength. A thermal metasurface with different functionalities can then be realized at different wavelengths [10].

A current limitation with the design presented in this thesis and the designs from [10, 11] is that the scattering structures are symmetric. If the edge of the lens strongly diffracts towards the center of the sample surface at angle θ relative to normal, it will also efficiently scatter towards angle $-\theta$ away from the intended focal point. To improve this inefficiency, breaking the symmetry of the structure either through nonreciprocity or surface structuring is an important avenue to explore.

While our structure is unique in its ability to focus linear, p-polarized thermal emission, larger phase gradients (i.e. greater than π) require different mechanisms of imparting a phase profile than those presented in Chapter 5. For circularly polarized thermal emission, geometric phase of 2π can be realized for a thermal metasurface [12].

Beyond enlightening the fundamental limits of coherence that are available to a thermal lens, the application of a cheap, directionally sensitive thermal emitter could be used in detection and ranging systems. Combined with data processing and training, passive infrared imagers and detectors have been proposed in heat-assisted detection and ranging (HADAR) systems [13]. This detection and ranging scheme leverages the ubiquity of thermally emitted radiation by removing the need for high-powered lasers to detect objects more than a few hundred meters away.

Overall, there are multiple near and long-term research questions that are actively being pursued in the field of thermal nanophotonics. The most immediately applicable nanophotonic

advancements are the spectral and directional engineering of thermal emitters for radiative cooling. Kirchhoff-violating thermal emission has been shown feasible in this thesis, however cooling and energy harvesting systems that experimentally realize an advantage over reciprocal systems are yet to be demonstrated. As our control of thermal radiation approaches the same level of sophistication as conventional metasurfaces, the possibility of realizing higher level systems like fully integrated thermal sources, detectors, and imagers is revolutionary for the infrared optics industry.

References

[1] S. Yang, C. Jianfeng, G. Xu, J. Li, X. Kong, C.-W. Qiu, One-way heat transfer in deep-subwavelength thermophotonics. *arXiv physics.optics* **2410**, 1-15 (2024).

[2] R. Hu, Z. Chen, S.-K. Kim, Can thermal nonreciprocity help radiative cooling? *Research* **7**, 1-3 (2024)

[3] S. Yang, M. Liu, C. Zhao, S. Fan, C.-W. Qiu, Nonreciprocal thermal photonics. *Nature Photonics* **18**, 412-424 (2024).

[4] F. Xie, et al., Subambient daytime radiative cooling of vertical surfaces. *Science* **386**, 788-794 (2024).

[5] A. P. Raman, M. A. Anoma, L. Zhu, E. Rephaeli, S. Fan, Passive radiative cooling below ambient air temperature under direct sunlight. *Nature* **515**, 540-544 (2014).

[6] Y. Dong, et al., Fizeau drag in graphene plasmonics. *Nature* **594**, 513-516 (2021).

[7] Z. Yu & S. Fan, Complete optical isolation created by indirect interband photonic transitions. *Nature Photonics* **3**, 91-94 (2009).

[8] A. Ghanekar, J. Wang, C. Guo, S. Fan, M. L. Povinelli, Nonreciprocal thermal emission using spatiotemporal modulation of graphene. *ACS Photonics* **10**, 170-178 (2023).

[9] I.-C. Benea-Chelmus, et al., Gigahertz free-space electro-optic modulators based on Mie resonances. *Nature Comm.* **13**, 3170 (2022).

[10] M. Zhou, E. Khoram, D. Liu, B. Liu, S. Fan, M. L. Povinelli, Z. Yu, Self-focused thermal emission and holography realized by mesoscopic thermal emitters. *ACS Photonics* **8**, 497-504 (2021).

[11] H. Chalabi, A. Alu, M. L. Brongersma, Focused thermal emission from a nanostructured SiC surface. *Phys. Rev. B* **94**, 094307 (2016).

[12] J. R. Nolen, A. C. Overvig, M. Cotrufo, A. Alu, Local control of polarization and geometric phase in thermal metasurfaces. *Nature Nanotechnology* **19**, 1627-1634 (2024).

[13] F. Bao, X. Wang, S. H. Sureshbabu, G. Sreekumar, L. Yang, V. Aggarwal, V. N. Boddeti, Z. Jacob, Heat-assisted detection and ranging. *Nature* **619**, 743-748 (2023).

Appendix

Experimental setups

A.1 Angle-resolved thermal emission with magnetic field

To carry out the direct emissivity measurements with an external magnetic field, we fasten a Newport motorized goniometer (BGS80) to the center platform of a GMW 5403 electromagnet (Figure A.1 a). The motorized stage is controlled remotely using an ESP 301 motion controller box and software from Newport.

The distance from the surface of the goniometer stage to the axis of rotation is 57.5 mm, meaning the sample surface that is being measured must be 57.5 mm from the goniometer surface for eucentric rotation relative to the FTIR. Furthermore, the sample must be fully between the pole pieces of the electromagnet to apply a uniform magnetic field across the sample's surface. This requires having an extension from the stage surface to the center of the pole pieces that is sufficiently long and narrow, to not limit the pole piece spacing. Aligning the sample surface relative to the FTIR port requires reflecting an internal alignment laser from the FTIR off the sample surface, back into the FTIR.

To heat the sample for direct emissivity measurements, we use high-performance thermoelectric modules from TE-technologies and read out the surface temperature using a thermistor (MP-3193) that is attached to the heater using temperature-stable polyimide double-sided tape from Polyonics (XT-679). We control the heater with a TE-technologies PID controller (TC-48-20), which regulates the power (current) being supplied from a 12 V DC power supply (PS-48-10).

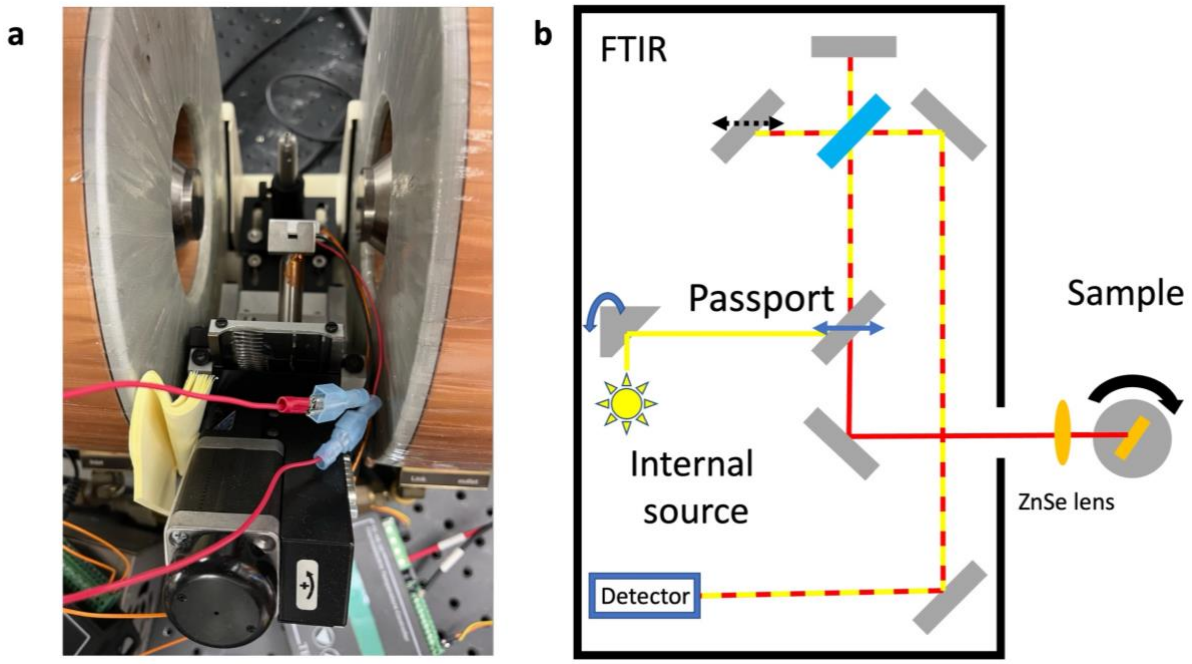

Figure A.1 Magneto-optical thermal emissivity setup. (a) Photo of the goniometer and heater placed between the electromagnet pole pieces. The sample surface must be at the rotation axis of the goniometer, and the rotation axis should be at the faces of the two pole pieces of the electromagnet. The red wires carry the input current to the thermoelectric heater. The orange wires carry the signal for the thermistor. (**b**) Beampaths for the sample emission (red) and internal source (yellow). The passport mirror's position determines whether emission from the sample or internal source is passed through to the detector.

To use the emission from our sample as the thermal source for our FTIR, we purchased and installed a custom mirror track from ThermoFisher (is50 gold dual passport mirror) which allowed us to switch between the internal source of the FTIR and a collimated, external source (our sample) using the software (omnic) provided by ThermoFisher. The emission from the sample surface is collimated by a low numerical aperture zinc selenide lens. The area of the sample (16 mm^2) far exceeds the collection area of the lens (0.05 mm^2), so we see little intensity variation up to ~ 60 degrees angle of incidence. We normalize the emitted intensity of the sample by a reference blackbody to retrieve the emissivity of the sample.

A.2 Thermal lensing setup

To measure the emission from the optimized thermal lens, we use a setup that can collimate the emission from the thermal lens into the FTIR or magnify the thermal lens emission from the focal plane to the image plane on the microbolometer array (infrared camera). The infrared camera (Xenics Gobi) setup is automated apart from inserting spectral filters and polarizers in front of the camera for spectral and polarization resolution. We control the acquisition parameters of the camera (pixels to acquire, calibration data, etc.) using the Xeneth 2.7 software.

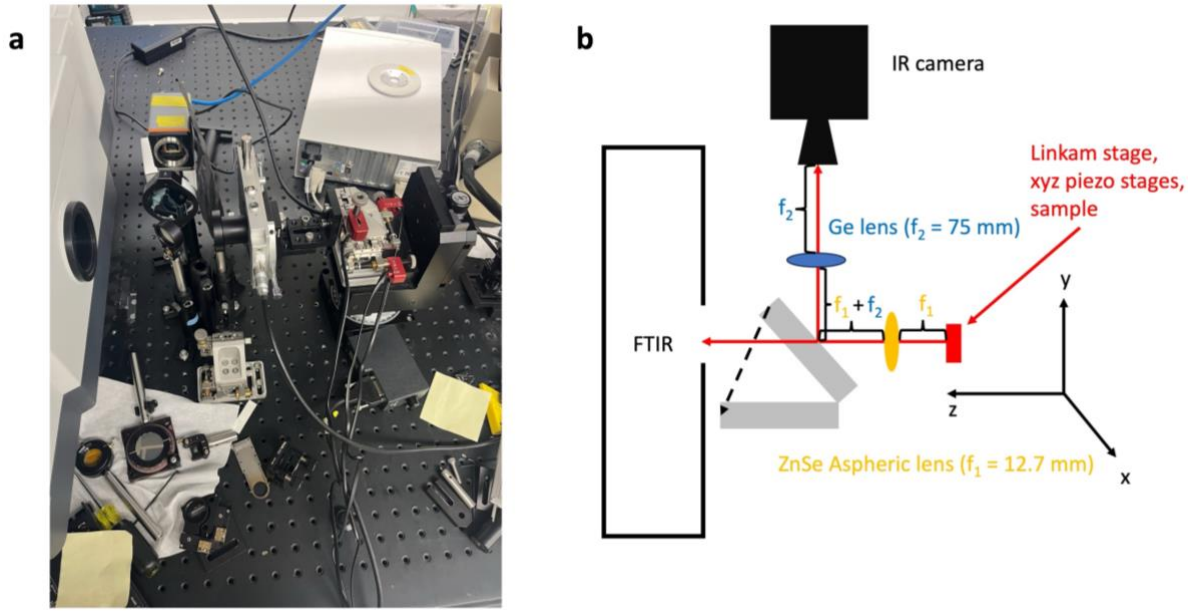

Figure A.2 Thermal lensing setup. (a) Photo of the setup. (**b**) Beampath for the thermal lensing setup. We use a two-lens setup to magnify (f_2 / f_1) the sample onto an infrared camera (8 – 14 μm spectral bandwidth). We use a flip mirror to transition from collecting the signal from the thermal lens onto the microbolometer array to the FTIR. To enable spectral resolution in the camera configuration, we use 500 nm bandwidth filters with 8 μm, 8.5 μm, and 9 μm center wavelengths.

For thermal lensing measurements, we require higher temperatures for the sample as compared to the magneto-optic emissivity measurements. This is a consequence of two factors, namely, 1) the increased sample attenuation when passing the sample signal through both the high numerical aperture zinc selenide and low numerical aperture germanium lenses and 2) the smaller relative sample area that is emitting (the lenses are 200 μm by 200 μm). To reach the required higher sample temperatures, we use a Linkam THMS 350 V heater with a stage controller. The maximum temperature of the stage reaches 350 C with the sample in ambient conditions.

For spatial intensity mapping measurements, which yield the intensity fall-off of the sample as a function of distance, we mount the Linkam stage to a set of XYZ-piezo positioners (Newport 9062). The average step size of the positioner in the z-direction is approximately 10 nm, however this value varies widely depending on the load on the positioner. Both the step size and the hysteresis are characterized through displacing the sample stage a known (1 mm) distance and dividing by the total number of steps required forwards and backwards. We mount the Linkam stage to the piezo positioner with a long (20 cm) standoff to thermally isolate the piezo positioners from the stage.

Because there is a relationship between the intensity falloff of the directive emission and the wavelength of the emitted radiation, we use a set of bandpass infrared filters for the directive emission measurements. The center wavelengths of the bandpass filters we use are at 8 μm, 8.5 μm, and 9 μm, with a 500 nm full-width at half-maximum. These filters allow us to create spatial maps of the intensity with wavelength resolution (Figure A.4).

With the polarizer and wavelength filter included in the beampath of the setup, there is significant signal attenuation. In addition to the attenuation, there is a thermal drift in the response of the microbolometer array that composes the camera (at the image plane of the setup). To compensate for any drift that occurs during spatial measurements of the thermal lens's intensity,

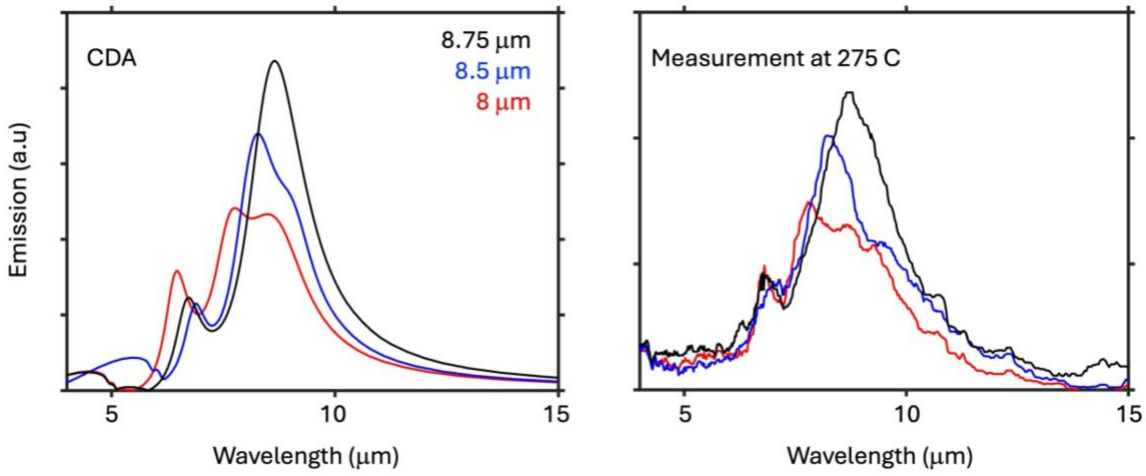

Figure A.3 Spectra of the thermal lenses using the FTIR beampath. Collected emission spectra from lenses with varying optimized wavelengths. The left panel are the expected spectra of the optimized lenses and the right side are the measured spectra when heating the samples to 275 C.

we calibrate the camera before each measurement using the manual calibration in the Xeneth 2.7 control software of the Gobi camera.

Spatial maps of the thermally emitted radiation with varying wavelength filters are shown in Figure A.4. We include the coupled dipole approximation simulations of the far-field intensity in the inset of each spatial map. The maps are made by scanning the sample away from the focus of the imaging setup (while in the camera configuration).

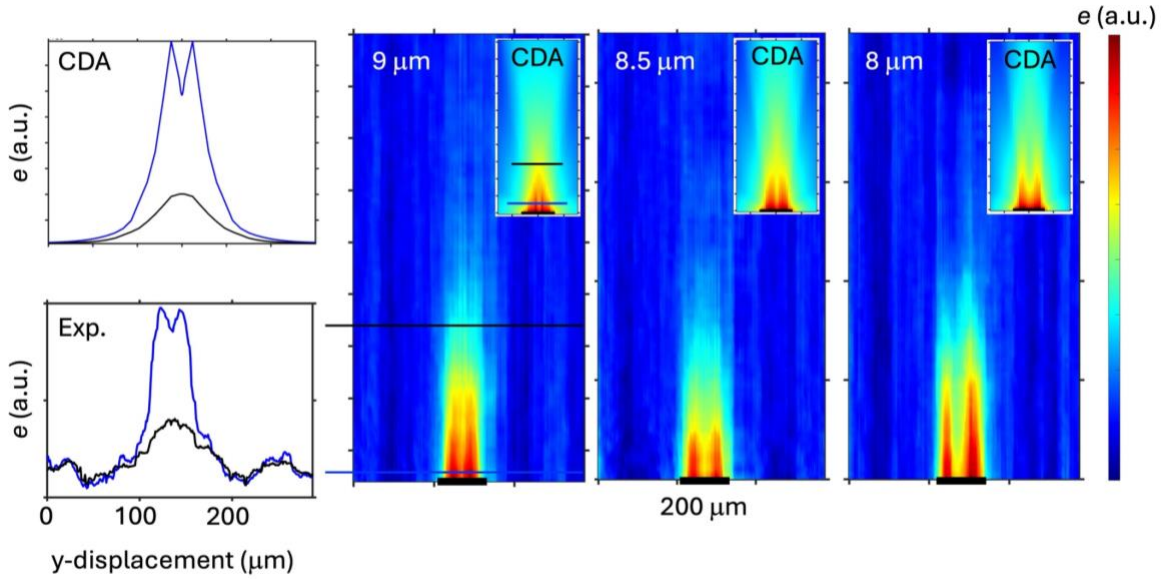

Figure A.4 Spatial maps at of the emitted radiation from an optimized structure at 8 μm, 8.5 μm, and 9 μm. Linecuts for both the CDA and the experimental measurements at the surface and focal point of the lens are shown on the left panels.